ABSTRACT

Title of dissertation: MICROTURBULENT TRANSPORT OF NON-MAXWELLIAN ALPHA PARTICLES

George John Wilkie, Doctor of Philosophy, 2015

Dissertation directed by: Professor William Dorland
Department of Physics

A burning Deuterium-Tritium plasma is one which depends upon fusion-produced alpha particles for self-heating. Whether a plasma can reach a burning state requires knowledge of the transport of alpha particles, and turbulence is one such source of transport. The alpha particle distribution in collisional equilibrium forms a non-Maxwellian tail which spans orders of magnitude in energy, and it is this tail that is responsible for heating the plasma. Newly-born high-energy alpha particles are not expected to respond to turbulence as strongly as alpha particles that have slowed down to the bulk plasma temperature. This dissertation presents a low-collisionality derivation of gyrokinetics relevant for alpha particles and describes the upgrades made to the GS2 flux-tube code to handle general non-Maxwellian energy distributions. With the ability to run self-consistent simulations with a population of alpha particles, we can examine certain assumptions commonly made about alpha particles in the context of microturbulence. It is found that microturbulence can compete with collisional slowing-down, altering the distribution further. One assumption that holds well in electrostatic turbulence is the trace approximation,

which is built upon to develop a model for efficiently calculating the coupled radial-energy turbulent transport of a non-Maxwellian species. A new code was written for this purpose and corrections to the global alpha particle heating profile due to microturbulence in an ITER-like scenario are presented along with sensitivity studies.

MICROTURBULENT TRANSPORT OF NON-MAXWELLIAN ALPHA PARTICLES

by

George John Wilkie

Dissertation submitted to the Faculty of the Graduate School of the
University of Maryland, College Park in partial fulfillment
of the requirements for the degree of
Doctor of Philosophy
2015

Advisory Committee:
Professor William Dorland, Chair/Advisor
Professor Thomas Antonsen
Professor Adil Hassam
Professor James Drake
Professor Ramani Duraiswami

Dedication

To my loving wife, Amber.

Acknowledgments

There are many people to whom I owe thanks for giving me the opportunity to study physics, and people without whom I could not have finished the degree. At the risk of unintentionally leaving out some of these important people, I would like to take this opportunity to recognize the contributions particular individuals have made in my personal life and career.

First of all, I would like to thank my family. My parents, Barbara and George, have raised me in a comfortable home where I was encouraged to pursue my interests. From telescopes to Europe trips, they have shaped me in many ways. I am grateful for all they have done for me over the years. My extended family also played an important role, accepting me for all my quirks and always being there for me. My grandparents, George, Anne, John, and Elizabeth have all built a legacy of integrity and hard work that myself and further generations will continue to benefit from.

From the day I was admitted to the graduate program at Maryland, my wife Amber has been nothing but supportive. Through all the emotional ups and downs (and a precipitous drop in pay after getting married!), I have not caught a hint of resentment or regret. Thanks to her hard work building a successful business, we have been able to live comfortably while I chased a dream. I hope to someday return the favor.

I remember Amber asking once, prompted by a book she was reading, "If you could travel anywhere and study under any person you wanted, who would it be?". I realized then that I was hard-pressed to find a better mentor than my doctoral

advisor, Bill Dorland. I am fortunate to have had Bill as a supportive and generous advisor who gave me the confidence and motivation to continue working when it got difficult. He is truly an inspirational figure. Even if I had an additional five years to study under him, I would continue to benefit from his expertise and wisdom.

The research community I have been introduced to has also played a large role in whatever success I have had in graduate school. I was particularly fortunate to engage in productive collaborations with Ian Abel, Edmund Highcock, and Matt Landreman, each of whom contributed significant work that made this dissertation possible. This community has been remarkable in the openness with which people are questioned and encouraged. From the very beginning, I have had the feeling that among these scientists, ideas stand on their own merits, whether they come from a student or a seasoned expert. Among those I have had the pleasure of interacting with, who helped make me more comfortable and contributed to the positive feelings I have about the academic community include: Alex Schekochihin, Greg Hammett, Steve Cowley, Nuno Louriero, Jason TenBarge, Matt Kunz, Michael Barnes, Felix Parra, Istvan Pusztai, Anne White, Nathan Howard, and Jonathan Citrin. I have also learned a lot from my fellow graduate students at Maryland and elsewhere, and I am glad I have had the opportunity to engage with them early in what will surely be their successful careers. These include Anjor Kanekar, Wrick Sengupta, Joel Dahlin, Ferdinand van Wyk, Michael Fox, Joseph Parker, Justin Ball, Jimmy Juno, and Noah Mandell.

I am also grateful to my committee: Professors Jim Drake, Adil Hassam, Tom Antonsen, and Ramaini Duraiswami. These professors are all very busy and still

donated their time to review this dissertation and provide valuable feedback. They took this responsibility seriously, and this work is stronger as a result. I would also like to thank Bill Dorland, Amber Wilkie, David Emerson, and Matt Landreman for spending the time to help proofread this dissertation.

I am thankful for Professor Tünde Fülöp for offering the opportunity to come work at Chalmers and thus providing significant motivation to finish and defend the dissertation!

Graduate school would not have been a possibility for me if it weren't for my time at NSWC, which prepared me for a career in science. In particular, John Vamos, Mike Gillum, John Hill, John Allwine, Frank Regan, and Chris Tomko were wonderful superiors and mentors. I have benefited from how seriously they took their responsibilities to their employees, and I am indebted to them for taking a chance on me out of college. I hope they got as much out of my time there as I did.

This work was supported by the U.S. Department of Energy by the grants numbered DE-FG02-93ER54197 and DE-FC02-08ER54964. Simulations were performed on the supercomputers Hopper and Edison at NERSC, Helios at IFERC, and Stampede at XSEDE.

Table of Contents

List of Figures

List of Abbreviations

CFL	Courant-Friedrichs-Lewy
DT	Deuterium-Tritium
EAE	Ellipticity-induced Alfvén eigenmode
EPM	Energetic particle mode
ITER	International Thermonuclear Experimental Reactor
IREAP	Institute for Research in Electronics and Applied Physics
ITG	Ion temperature gradient
JET	Joint European Torus
keV	Kilo-electron volt
KTAE	Kinetic TAE
MHD	Magnetohydrodynamics
LCFS	Last closed flux surface
MeV	Mega-electron volt
PDE	Partial differential equation
PIC	Particle-in-cell
TAE	Toroidicity-induced Alfvén eigenmode
TEM	Trapped electron mode

Conventions

- Gaussian cgs units
- Thermal speed $v_{ts} \equiv \sqrt{2T_s/m_s}$
- Coulomb gauge: $\nabla \cdot \mathbf{A} = 0$.

Chapter 1: Introduction

1.1 Motivation

The ultimate goal of the global fusion research program is to sustain a plasma in a *burning* state: where the energetic products of the nuclear fusion reaction provide sufficient heating to keep the plasma at fusion-relevant temperatures. The easiest fusion reaction to achieve (based on the required plasma temperature) is that between two isotopes of hydrogen, deuterium and tritium:

$$\mathrm{H}_2 + \mathrm{H}_3 \rightarrow \mathrm{He}_4\,(3.5\mathrm{MeV}) + \mathrm{n}_1\,(14.1\mathrm{MeV})\,. \tag{1.1}$$

In magnetic confinement experiments, a plasma with a temperature of at least 10 keV (about 11 million kelvin) is kept isolated from cool material by strong magnetic fields. Charged particles (of a particular species s, such as deuterons, tritons, or electrons) in magnetic fields are known to follow *Larmor orbits* in the plane perpendicular to the magnetic field. In a strong enough magnetic field (to be elaborated upon in chapter 2), this orbit is a circle of a radius proportional to its perpendicular speed $v_\perp$. This radius is known as as the Larmor- or gyro-radius. On the other hand, the motion of a charged particle along a straight magnetic field line is unaf-

fected by the magnetic field. This characteristic motion is a critical component to magnetic confinement, but it is not sufficient. Other phenomena, such as gradients in the field, pressure gradients, imposed electromagnetic waves, radiation, collisions, fluid and kinetic instabilities all play crucial roles in the feasibility of a confinement scheme. The tokamak and stellarator are two configurations that have gotten the most attention and are currently the most promising technologies for controlled fusion.

From the D-T reaction (1.1), it is clear that the neutron carries away most of the energy produced by fusion. There is no way to confine a neutron in a magnetic field, and since its collision cross section is so small, it will escape the plasma. Power plant concepts (such as DEMO) rely upon these high energy neutrons to heat a "blanket", which converts the neutron energy into heat. Such high energies can also cause problems for other components, the mitigation of which is an important line of study.

Since neutrons escape the plasma, if we wish to have a burning plasma which requires little or no external heating, it is the alpha particle which must eventually provide energy to the plasma. This transfer of energy will most likely occur through collisions, although there are alternative concepts to capture this energy in waves for efficiency (a hypothetical technique known as *alpha channelling* [7, 8]). We will describe this basic collisional heating mechanism later in section 1.4.2.

Despite decades of research, this burning state has not yet been achieved, and one of the critical roadblocks was the experimental discovery of "anomalous" transport. We now know that this escape of energy is caused by turbulence driven

by plasma microinstabilities that feed off of the free energy in equilibrium gradients. This turbulence limits, for example, how strongly the ion temperature (an increase in which is necessary for fusion) can increase throughout the core of the device. The turbulence generated also has effects, either beneficial or detrimental, on the transport of plasma impurities[1]. Once an alpha particle has slowed down and lost its usefulness in heating the plasma, it is considered an impurity: spent fuel known as helium *ash*.

This dissertation focuses on the effect of this turbulence on the transport of fusion-produced alpha particles.

1.2 Scope of this work

Since the fate of alpha particles is so important to the goal of fusion, it has gotten a lot of attention, and the most important aspects have been identified and studied. Also because the topic is important, we as a community ought to thoroughly understand all sources of alpha transport. This dissertation represents an effort to develop a unified view of alpha particles in the context of primarily electrostatic drift wave turbulence.

One important effect of alpha particles is the destabilization of Alfvén waves under certain conditions [9–11]. These waves, in turn, can have a dramatic effect on alpha particle transport. For example, wave-particle interaction can cause resonance overlap [12, 13], which opens an especially efficient channel for radial transport of alphas. While not the focus of this dissertation, appendix A includes a brief study of

[1] Defined, for our purposes, as anything that isn't fusion fuel or neutralizing electrons

non-Maxwellian effects on TAE destabilization. We make no claim that turbulent transport is dominant over these Alfvénic phenomena when and where they are active. However, turbulence is nearly ubiquitous and provides a baseline level of transport, and will be present even if these other transport mechanisms are somehow solved or mitigated. Furthermore, since turbulence plays a role in determining the alpha particle profile, it can have an effect on when and where this enhanced Alfvénic activity occurs. Indeed, stiff transport models for TAEs, combined with anomalous transport, are actively being developed [14]. It is in this context that this dissertation can be most appreciated: as part of a radially-global, comprehensive transport model for alpha particles.

An important transport mechanism of alpha particles we do not consider here is so-called *ripple-loss*. Neoclassical effects are usually small for fast ions in tokamaks, but the breaking of axisymmetry (due to a finite number of toroidal magnetic coils, for example) enhances this neoclassical transport to appreciable levels. This is expected to occur mostly in the edge region, where the error field (that which is not axisymmetric) is the highest. As an alpha particle gets even closer to the edge, its finite-orbit size could cause it to directly escape the confined plasma.

This dissertation focuses on tokamak geometry, which is toroidal with an axisymmetric magnetic field. A key feature of the tokamak is a plasma current that induces a magnetic field in the poloidal direction (the "short way" around the torus) that is necessary for confinement. The techniques developed and insights gained in this dissertation, however, apply equally well to stellarators or to any other magnetized confinement concept in which gyrokinetic turbulence plays a significant role.

1.3 Present state of research and the approach of this dissertation

There has been a considerable amount of work done on the topic of turbulence and alpha particles. Estrada-Mila, Candy, Waltz [15] performed numerical simulations using `GYRO` [16] and found significant transport of high-energy alpha particles in the core due to electrostatic turbulence. This was confirmed by Albergante [17] using `GENE` [18], and it was stressed that turbulence can result in a pinch of low-energy helium ash, a result which Angioni [19] also found with `GS2` [20, 21]. Dannert [22] also used `GENE` to study the effect of turbulence on anisotropic beam ions. All of these nonlinear gyrokinetic simulations of alpha particle transport were performed by treating the alpha particle population as a hot Maxwellian species, using the so-called *equivalent Maxwellian* approximation. This approximation has been in use for a long time [23], and was formalized in reference [15].

However, alpha particles are not Maxwellian [24], a fact which is well-recognized in the above references. Indeed, care was taken to show that using a Maxwellian of the same temperature gave approximately accurate linear results for their particular cases. Then, linear simulations using `GS2` were performed using the non-Maxwellian slowing-down distribution [25] to obtain the radial flux of alpha particles, where attention was drawn to the incorrectness of the radial gradient of the equivalent Maxwellian. In this work, we demonstrate that the numerical value of the alpha particle flux found this way can be poorly estimated, depending on the local parameters used. The equivalent Maxwellian approximation is inadequate, and we present a method to rigorously obtain the correct energy-dependent flux which is valid in

the trace[2] limit.

However, turbulent diffusion is selectively relevant depending on energy, in which there is a wide range of scales between the bulk temperature at 10 keV and the alpha particle birth energy $E_\alpha \approx 3.5\,\mathrm{MeV}$. Therefore, an overall integrated diffusion coefficient cannot be expected to capture all the relevant physics. An effort at IPP Garching, lead by Hauff, Jenko [26, 27], and later Pueschel [28] sought to develop energy scalings of turbulent diffusion by treating the electrostatic ion-scale turbulence as a given background field with known properties, to which the energetic particles passively react. It was found [15,29] that the diffusion of energetic particles scales inversely with energy (E^{-1}) for particles with high pitch angle ($v_\parallel \sim v$), and as $E^{-3/2}$ for deeply-trapped energetic particles. It was later pointed out [28] that this is an expansion in Larmor radius, with the former result valid only for prohibitively large pitch angles for particles of such high energy. Therefore, an overall $E^{-3/2}$ scaling is expected, a result we confirm. This is in contrast to parallel work by Zhang, Lin, and colleagues [30], who find a different energy scaling from their simulations.

This work builds upon these foundations to solve for the global transport of alpha particles, coupled in radius and energy. The basic technique for trace transport (described fully in chapter 4) was first applied by Albergante [17] to the simpler case of Maxwellian trace species. We expand upon this by solving for the entire equilibrium distribution as a function of radius and energy with no *a priori* assumptions

[2]When we refer to a species as "trace", what is meant is a species that contributes negligibly to the electromagnetic fields, usually because of its /low concentration in the plasma.

about its form, apart from imposed boundary conditions. This approach is indebted to the insights of Hauff [27] in treating the diffusion coefficient as a strong function of energy, and to Angioni [25] in recognizing the linear dependence of the fluxes on the energy-dependent equilibrium.

We begin in chapter 2 by formally deriving gyrokinetics for a non-Maxwellian species, including the transport equation for the equilibrium, which will depend upon the steady-state behavior of the turbulence. We choose to use the Eulerian flux-tube gyrokinetic solver `GS2` to solve the gyrokinetic equation because of issues encountered with the δf particle-in-cell algorithm, discussed in appendix B. Furthermore, a method to retain spectral accuracy for velocity space integrals for an arbitrary isotropic distribution was found and developed (see appendix C), which further influenced this decision. With `GS2` so upgraded to handle non-Maxwellian species, in chapter 3 and reference [31], we challenge several assumptions commonly used in the analysis of alpha particles. We show that the Maxwellian model for fast alpha particles is inadequate, but also that the slowing-down distribution (discussed in the next section), the next-best approximation, is also invalid due to the influence of turbulent transport. Since we therefore need to solve the gyrokinetic equation without knowing the form of the equilibrium distribution, a novel technique is required. Based on the trace approximation, we showcase a new code in chapter 4, `T3CORE`, which acts as a post-processor to existing gyrokinetic simulations and constructs the radius-energy coupled equilibrium distribution, taking into account the effects of collisions and microturbulence. Finally, we apply this new tool to the problem of alpha particle transport in chapter 5 and show that turbulence has a

significant effect on the most interesting and important aspects of alpha particles in fusion plasmas.

1.4 Basic alpha particle physics

We begin by introducing some of the basic ideas that we will be revisiting throughout this dissertation. We do so by chronologically telling the story of a fusion-produced alpha particle as it slows down in the plasma. In the process, we will derive the analytic slowing-down distribution of Gaffey [24], which is now a textbook plasma physics problem [32, 33]. While this work challenges the strict validity of this distribution in the presence of microturbulence, it is the structure upon which we build, and the physics that go into its derivation remain important.

1.4.1 High-energy source

From the DT fusion reaction (1.1), alpha particles are born universally at a constant energy $E_\alpha \approx 3.5\,\mathrm{MeV}$. So one may choose to define the source as a Dirac delta function:

$$S_{\alpha,m}(v) = \frac{\sigma_\alpha}{4\pi v_\alpha^2}\delta(v - v_\alpha), \tag{1.2}$$

where $v_\alpha = \sqrt{2E_\alpha/m_\alpha}$ is the alpha particle birth speed. The total source of alpha particles σ_α is a function of plasma density, temperature, and composition, and can be approximated [34] by:

$$\sigma_\alpha = 3.68 \times 10^{-18}\frac{\mathrm{m}^3}{\mathrm{s}} n_D n_T \left(\frac{T_i}{\mathrm{keV}}\right)^{-2/3} \exp\left[-19.94\left(\frac{T_i}{\mathrm{keV}}\right)^{-1/3}\right], \tag{1.3}$$

where n_D and n_T are the number densities of deuterium and tritium respectively, and T_i is the ion temperature, assumed common to both species.

The mono-energetic source in equation (1.2) is as measured in the *center of mass frame of the reactant ions*. We must transform into the lab frame[3] to get the apparent distribution in energy from the perspective of the bulk plasma. One might think that, since the typical energies of the reactant deuterium and tritium ions are so much smaller than E_α, that this spread is negligible. However, it is *not* typical ions that fuse; only the most energetic ones do. Therefore, this spread is determined by the speed of *fusing* ions, not thermal ions. The actual source of alpha particles can be approximated by a Gaussian in energy [36,37], with a width proportional to the geometric mean of E_α and T_i:

$$S_\alpha(v) = A \exp\left[-\frac{m_n + m_\alpha}{16 m_\alpha} \frac{m_\alpha^2 \left(v^2 - v_\alpha^2\right)^2}{T_i E_\alpha}\right], \tag{1.4}$$

where m_α and m_n are the masses of an alpha particle and a neutron, respectively. The normalization constant A is chosen so that $\int S_\alpha \, \mathrm{d}^3\mathbf{v} = \sigma_\alpha$ from equation (1.3). A representative shape of this source is shown in figure 1.1.

Another common misconception about the source of alpha particles is that it is a very strong function of temperature. One may then expect that the majority of alpha particles are only produced very close to the magnetic axis, where the ion temperature is the highest. However, this is not the case. Even though T_i appears in an exponent in equation (1.3), it does so only with a fractional power. In figure 1.2,

[3] or at least to the rest-frame of the plasma or even a particular flux surface, see reference [35]

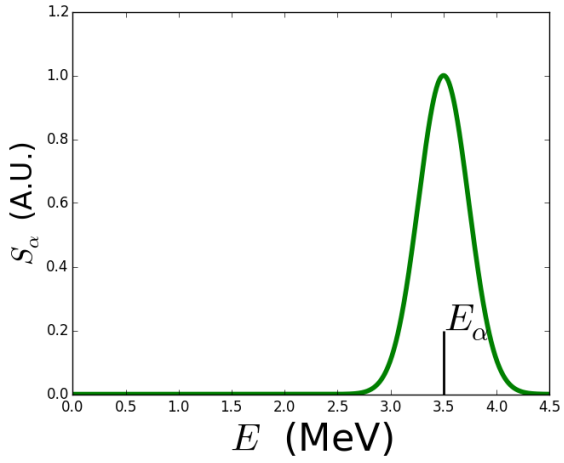

Figure 1.1: The shape of the alpha particle source in the plasma rest frame at $T_i = 10\,\mathrm{keV}$.

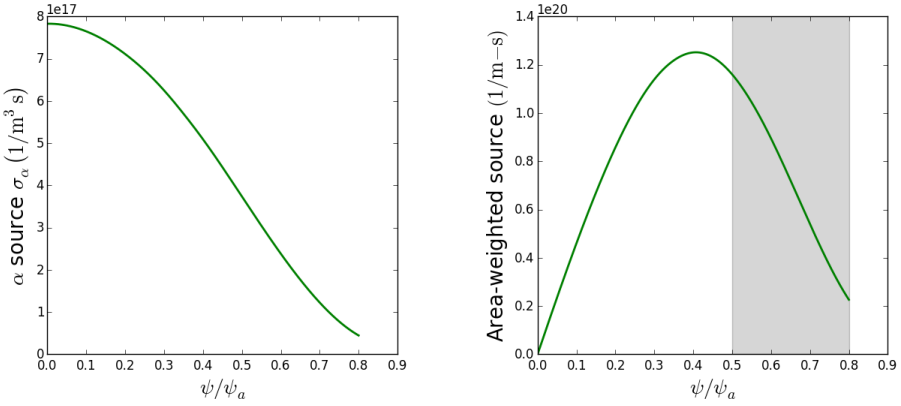

Figure 1.2: The radial dependence of the fusion cross section $\sigma_\alpha/n_D n_T$ in a typical ITER scenario [1]. On the right, the area of the flux surfaces are taken into account to illustrate the relative total number of alpha particles produced at different radii. The shaded region is the computational domain studied in chapter 5.

we plot the radial dependence of the fusion cross section for a representative ITER scenario (one which we will revisit in chapters 3 and 5). We can see that a significant fraction of alpha particles are produced in the region where microturbulence is most active.

When alphas are born at this high energy, they typically have a very large Larmor radius as a result, about an order of magnitude larger than that of the bulk ions. The turbulence generated by these slower ions has eddies of a characteristic

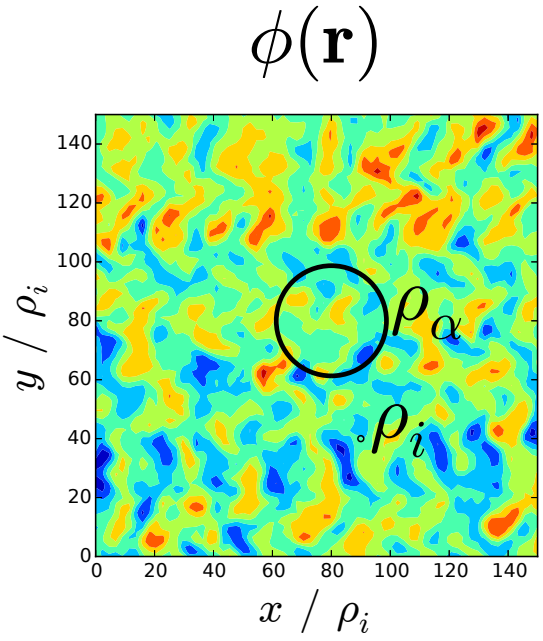

Figure 1.3: A Larmor orbit of a 3.5 MeV alpha particle super-imposed on a representative snapshot of the electrostatic potential in ITG turbulence, along with that of a thermal deuterium ion. When the potential is averaged over such an orbit, one observes an attenuated effective potential. Note that the thermal ion Larmor radius is the scale in the x and y directions.

size several times larger than the Larmor radius of the ions, but still significantly less than that of the alpha particles. See figure 1.3 for an illustration of these scales.

Furthermore, the magnetic orbit of an alpha particle (characterized by the poloidal Larmor radius; see table 1.1) is even larger still, and these effects combine to weaken the response of the highest-energy alpha particles to the turbulence, since their orbits average over many fluctuations. As alpha particles slow down, they begin responding more and more strongly to the turbulence.

If the poloidal Larmor radius is too large, however, this means that the magnetic orbit causes a significant deviation from a flux surface, and as a result the local flux-tube approach of gyrokinetics can be called into question. For this reason, we focus on ITER results, since that is the device in which one could most rigorously

Table 1.1: Properties of some typical tokamak properties, using the radial-average values from [1]. Ion species is deuterium, and alpha particle parameters are taken at 3.5 MeV.

		TFTR	JET	ITER
Toroidal ion gyroradius	ρ_i/a	0.0028	0.0037	0.0013
Toroidal alpha gyroradius	ρ_α/a	0.040	0.058	0.018
Poloidal ion gyroradius	$\rho_{i,pol}/a$	0.026	0.026	0.0079
Poloidal alpha gyroradius	$\rho_{\alpha,pol}/a$	0.37	0.41	0.11
Ion-ion collision frequency	$\nu_{ii}a/v_{ti}$	2.7×10^{-5}	5.0×10^{-5}	1.6×10^{-4}
α-e slowing-down frequency	$\nu_s^{\alpha e}a/v_{ti}$	1.3×10^{-6}	2.4×10^{-6}	5.9×10^{-6}
Slowing-down time (s)	τ_s	0.48	1.0	0.85
Energy confinement time (s)	τ_E	0.13	0.59	2.98

apply the flux tube approximation for alpha particles.

1.4.2 Collisional slowing-down

To examine how alpha particles slow down and scatter off of the background, we must introduce the distribution of their positions and velocities. Much of plasma physics is concerned with describing the behavior of charged particles in a statistical sense through the distribution function f_s, with s labelling a particle species which has charge $Z_s e$ and mass m_s. This distribution is a function of spatial position $\mathbf{r}$, particle velocity $\mathbf{v}$, and time, normalized such that the probability dP of finding a particle in a infinitesimal volume spanned by $\mathbf{r}$ and $\mathbf{r} + \mathrm{d}^3\mathbf{r}$, and with an infinitesimal range of velocities between $\mathbf{v}$ and $\mathbf{v} + d^3\mathbf{v}$ at a particular time t is given by:

$$\mathrm{d}P = f_s\left(\mathbf{r}, \mathbf{v}, t\right)\, \mathrm{d}^3\mathbf{r}\, \mathrm{d}^3\mathbf{v}. \tag{1.5}$$

The spatial distribution of the plasma is almost always relevant, but it is often

helpful and sufficient to average over velocity space by taking *moments* such as density:

$$n_s \equiv \int f_s \, \mathrm{d}^3\mathbf{v}, \tag{1.6}$$

flow velocity

$$\mathbf{u}_s \equiv \frac{1}{n_s} \int f_s \mathbf{v} \, \mathrm{d}^3\mathbf{v}, \tag{1.7}$$

and temperature

$$T_s \equiv \frac{1}{n_s} \frac{m_s}{3} \int f_s \left|\mathbf{v} - \mathbf{u}_s\right|^2 \, \mathrm{d}^3\mathbf{v}. \tag{1.8}$$

Descriptions of plasma which are primarily concerned with achieving a closed set of equations for moments and manipulating them directly are known as *fluid theories*, and if a phenomenon is well-described by such equations, we say the plasma *is* a fluid in that context. This is in contrast to *kinetic theory*, which is concerned with the evolution of f_s directly to account for phenomena such as Landau damping, wave-particle interaction, and collisions. Kinetic theory has the advantage of being a more complete description of the plasma, but is often computationally and analytically intractable. Nevertheless, there are useful reductions that make the kinetic problem easier to solve. Gyrokinetics, discussed in chapter 2, is one such reduction.

The effects that inter-particle collisions have on the distribution function are represented by a *collision operator*. The Fokker-Planck collision operator is applicable to fully ionized plasma [32] such as found in fusion devices. For collisions of

test particles against a Maxwellian field, it is:

$$\begin{aligned} C\left[f_s\right] &= \sum_{s'} C\left[f_s, f_{s'}\right] \\ &= \sum_{s'} \left[\frac{\nu_D^{s,s'}}{2} \frac{\partial}{\partial \xi} \left(1-\xi^2\right) \frac{\partial f_s}{\partial \xi} + \frac{1}{v^2} \frac{\partial}{\partial v} \left(\nu_s^{s,s'} v^3 f_s + \frac{1}{2} \nu_\parallel^{s,s'} v^4 \frac{\partial f_s}{\partial v} \right) \right] \end{aligned} \tag{1.9}$$

To clarify the perhaps confusing notation of $\nu_s^{s,s'}$, the subscript s stands for "slowing-down" and the superscripts s and s' refer to species. The pitch angle $\xi \equiv v_\parallel / v$ is the ratio of the speed parallel to the magnetic field to the total speed. In this dissertation, we concern ourselves with isotropic f_s, and when averaging over pitch angle, the first term in equation (1.9) (the Lorentz operator) vanishes. The quantities ν_s and $\nu_\parallel$, when f_s collides with Maxwellian species s', are defined in our notation as:

$$\nu_s^{s,s'}\left(v\right) \equiv \frac{4\pi n_{s'} Z_s^2 Z_{s'}^2 e^4 \ln \Lambda_{s,s'}}{m_s T_{s'}} \frac{G\left(\frac{v}{v_{ts'}}\right)}{v} \tag{1.10}$$

$$\nu_\parallel^{s,s'}\left(v\right) \equiv \frac{8\pi n_{s'} Z_s^2 Z_{s'}^2 e^4 \ln \Lambda_{s,s'}}{m_s^2} \frac{G\left(\frac{v}{v_{ts'}}\right)}{v^3}, \tag{1.11}$$

where $\ln \Lambda_{s,s'}$ is the Coulomb logarithm, and the Chandrasekhar function G is related to the error function by:

$$G\left(x\right) \equiv \frac{\mathrm{Erf}\left(x\right) - \frac{2}{\sqrt{\pi}} x e^{-x^2}}{2x^2}. \tag{1.12}$$

This function has the following asymptotic forms, which will shortly come in handy:

$$G\left(x \ll 1\right) \approx \frac{2x}{3\sqrt{\pi}} \tag{1.13}$$

$$G\left(x \gg 1\right) \approx \frac{1}{2x^2}. \tag{1.14}$$

Now, let us consider what all this means for isotropic alpha particles colliding against a bulk background of ions and electrons:

$$C\left[f_\alpha\right] = \frac{1}{v^2}\frac{\partial}{\partial v}\left[v^3\left(\nu_s^{\alpha i} + \nu_s^{\alpha e}\right) f_\alpha + \frac{1}{2}v^4\left(\nu_\parallel^{\alpha i} + \nu_\parallel^{\alpha e}\right)\frac{\partial f_s}{\partial v}\right]. \tag{1.15}$$

Even though newly-born alphas have very high energy, thermal electrons are significantly faster. Therefore, we will apply the small argument expansion of G (1.13) to the alpha-electron terms in equation (1.15) and the large-argument expansion (1.14) to the alpha-ion terms. Furthermore, we will consider *only* the slowing-down term, because energy diffusion (as the $\nu_\parallel$ term is called) is only appreciable when $v \sim v_{ti}$. We are left with the following approximate form for the collision operator

$$C\left[f_\alpha\right] \approx \frac{1}{\tau_s}\frac{1}{v^2}\frac{\partial}{\partial v}\left[\left(v_c^3 + v^3\right) f_\alpha\right], \tag{1.16}$$

valid for $v_{ti} \ll v \ll v_{te}$. We have defined the *critical speed*

$$v_c \equiv v_{te}\left(\frac{3\sqrt{\pi}}{4}\sum_i \frac{n_i m_e}{n_e m_i} Z_i^2\right)^{1/3} \tag{1.17}$$

and the characteristic *slowing-down time*:

$$\tau_s \equiv \frac{3}{16\sqrt{\pi}} \frac{m_\alpha m_e v_{te}^3}{Z_\alpha^2 e^4 n_e \ln \Lambda_{\alpha e}}. \tag{1.18}$$

For simplicity, let us solve for the distribution which balances the mono-energetic source (1.2), with the approximate collision operator. That is, we seek an approximate steady-state solution to the equation

$$\frac{\partial f_\alpha}{\partial t} = C\left[f_\alpha\right] + S_{\alpha,m}. \tag{1.19}$$

When we plug in equation (1.16), we can solve for f_α as the analytic *slowing down distribution*:

$$F_s\left(v\right) \equiv \frac{3}{4\pi} \frac{1}{\ln\left(1 + v_\alpha^3/v_c^3\right)} \frac{n_\alpha}{v_c^3 + v^3}, \tag{1.20}$$

where we have chosen to express it in terms of the alpha particle density n_α, directly related to the source by:

$$n_\alpha = \frac{\sigma_\alpha \tau_s}{3} \ln\left(1 + \frac{v_\alpha^3}{v_c^3}\right). \tag{1.21}$$

If we know the gradients of the equilibrium properties, we can find the gradient

of the slowing down distribution as follows:

$$\begin{aligned}\frac{\nabla F_{S\alpha}}{F_{S\alpha}} =& \frac{1}{F_{S\alpha}}\frac{\partial F_{S\alpha}}{\partial n_\alpha}\nabla n_\alpha + \frac{1}{F_{S\alpha}}\frac{\partial F_{S\alpha}}{\partial v_c}\nabla v_c \\ =& \frac{\nabla n_\alpha}{n_\alpha} + \frac{1}{F_{S\alpha}}\frac{\partial F_{S\alpha}}{\partial v_c}\left(\frac{\partial v_c}{\partial T_e}\nabla T_e + \frac{\partial v_c}{\partial n_i}\nabla n_i + \frac{\partial v_c}{\partial n_e}\nabla n_e\right) \\ =& \frac{\nabla n_\alpha}{n_\alpha} + \left[\frac{v_\alpha^3}{v_c^3+v_\alpha^3}\frac{1}{\ln\left(1+v_\alpha^3/v_c^3\right)} - \frac{v_c^3}{v_c^3+v^3}\right]\times \\ & \left(\frac{3}{2}\frac{\nabla T_e}{T_e} - \frac{\nabla n_e}{n_e} + \frac{\sum_i Z_i^2\nabla n_i/m_i}{\sum_i Z_i^2 n_i/m_i}\right).\end{aligned} \tag{1.22}$$

Let us introduce the scale-length notation, in which we will find it convenient to express radial gradients, with an arbitrary radial coordinate[4] ψ. The density and temperature scale lengths for species s, for example, are respectively:

$$\frac{1}{L_{ns}} \equiv -\frac{1}{n_s}\frac{\partial n_s}{\partial \psi} \tag{1.23}$$

and

$$\frac{1}{L_{Ts}} \equiv -\frac{1}{T_s}\frac{\partial T_s}{\partial \psi}. \tag{1.24}$$

With this notation, we can also define a scale length for the alpha critical speed:

$$\frac{1}{L_{v_c}} \equiv -\frac{\partial}{\partial \psi}\ln v_c = \frac{3}{2}\frac{1}{L_{T_e}} - \frac{1}{L_{n_e}} + \frac{\sum_i Z_i^2 n_i/m_i L_{n_i}}{\sum_i Z_i^2 n_i/m_i}. \tag{1.25}$$

At the high energies at which they are born, alpha particles' main interaction with the plasma is collisional heating of the electrons. As they slow down, scattering

[4]Not to be confused with the toroidal or poloidal magnetic flux, which are *specific choices* of radial coordinate

against ions becomes more important, and they begin heating as well. Overall, depending on v_c, only about 30-40% of the alpha particle power goes to the ions [38]. This preferential heating of electrons can be seen as an inefficiency, since electrons do not fuse.

1.4.3 Thermalization

The fact that we were able to find a steady-state solution to equation (1.19) should give us pause; that equation does not admit a steady-state because it has a source! This can be easily verified by noting that the collision operator conserves density:

$$\left(\frac{\partial n_s}{\partial t}\right)_{\text{coll}} = \frac{\partial}{\partial t}\int C\left[f_s\right]\,\mathrm{d}^3\mathbf{v} = 0, \tag{1.26}$$

and integrating equation (1.19) over velocity space. Recall that we applied the approximation $v_{ti} \ll v \ll v_{te}$ to simplify the collision operator in equation (1.16), so this added density must build up where this approximation is not valid, namely where $v \sim v_{ti}$. So one cannot simply wait for a larger population of hot alpha particles to develop; the high-energy tail of the slowing down distribution is indeed a steady state. The alpha particles that build up are of lower energy.

Consider equation (1.19) without a source, or at least a very weak one. The steady-state solution is a *Maxwellian distribution*:

$$f_{Ms} \equiv n_s\left(\frac{m_s}{2\pi T_s}\right)^{3/2} e^{-m_s v^2/2T_s}, \tag{1.27}$$

parametrized by density n_s and temperature T_s[5]. It stands to reason that the low-energy part of the distribution (where collisions are much stronger) is Maxwellian in equilibrium with the ions, with ever-increasing density. This population of "cold" helium is what we refer to as "ash".

1.4.4 Transport

Of course, the density of this thermalized helium cannot continue growing forever. Eventually, radial transport must play a role. If the population of ash builds to too high of a level, it can get in the way of the fusion reaction. Effectively, if the total density of the plasma is fixed, then any non-fusing ions like ash decrease the densities n_D and n_T in equation (1.3). This effect is known as *dilution*.

However, it is not only the Maxwellian ash that transports. The primary result of this dissertation is that transport interferes with collisional slowing-down at moderate energies [31], modifying the distribution function further. Effectively, there should be an additional term in equation (1.19) accounting for the radial transport, such as in equation (4.16). This modification of f_α is not trivial and has important order-unity effects on key alpha particle diagnostics (see chapter 5). Figure 1.4 shows the overall effect of microturbulent radial transport from simulation on the alpha particles trajectories.

The remainder of this dissertation is organized to motivate this modification to the alpha particle distribution, convince the reader that it is physical and ought

[5]More generally, the mean flow $\mathbf{u}_s$ can also play a role. However, for clarity in this thesis, we ignore flow and the associated transport of momentum.

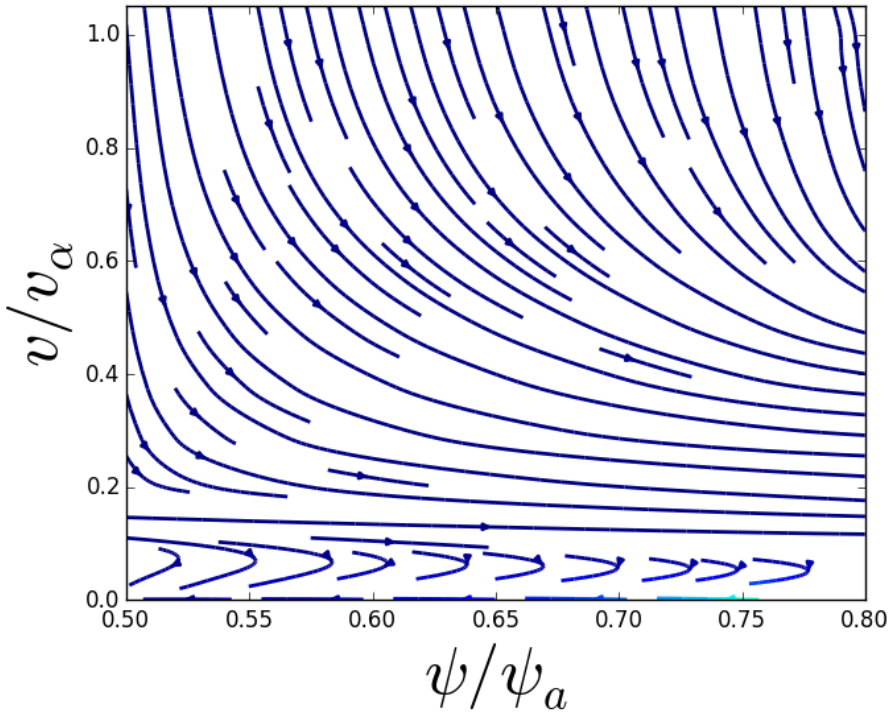

Figure 1.4: Streamlines of alpha particle trajectories in phase space under the influence of collisions and microturbulence for the baseline ITER scenario discussed in chapter 5.

to be accounted for, and to present an efficient solution method to find such a modification from first principles. The primary results concerning alpha particle transport are contained in chapter 5, and should be readable without building up the formalities of chapters 2 or 4. If the reader is interested in a basic motivation of why this work is necessary, chapter 3, based on reference [31], might be a useful place to start.

Chapter 2: Non-Maxwellian gyrokinetics

With the goal of studying alpha particles, a natural reduced kinetic formalism to use is gyrokinetics, since fast ions have a large Larmor radius compared to typical eddy sizes (see figure 1.3). Although the original treatments of gyrokinetics [39, 40] were derived for general anisotropic non-Maxwellian equilibrium distributions, the codes that have since been developed to solve the nonlinear gyrokinetic equation typically assume a Maxwellian equilibrium. Furthermore, the equation for the time evolution of a non-Maxwellian equilibrium (*i.e.*, the *transport equation*) has not been developed until recently [41, 42]. For high-energy alpha particles, the collision frequency is low, and the alpha particles do not form a Maxwellian distribution and instead form a power law (1.20). Therefore, the gyrokinetic ordering necessitates a low-collisionality generalization if it is to be useful in the study of alpha particles.

This chapter will present a derivation of gyrokinetics, allowing for isotropic non-Maxwellian distributions. This derivation is indebted to, and attempts to closely follow, the derivation of Abel and colleagues [35]. Here, we generalize for non-Maxwellian equilibrium, while excluding for clarity sonic flow, flow shear, and neoclassical corrections. This is not to be interpreted as dismissing the importance of these phenomena; in fact, these are rich topics of great importance to fusion. The

inclusion of equilibrium flow and neoclassical effects are coupled in subtle ways, a proper exposition of which is a dissertation in its own right [43], and to give it the attention it deserves herein would distract from the goal at hand, which is to illustrate the ways in which low-collisionality gyrokinetics differs from the "standard" Maxwellian treatment.

We start from the Fokker-Planck equation:

$$\frac{\partial f_s}{\partial t} + \mathbf{v} \cdot \nabla f_s + \frac{Z_s e}{m_s} \left(\mathbf{E} + \frac{1}{c} \mathbf{v} \times \mathbf{B} \right) \cdot \frac{\partial f_s}{\partial \mathbf{v}} = C\left[f_s \right] + S_s, \tag{2.1}$$

which describes the evolution of the distribution function f_s in the presence of a source $S_s\left(\mathbf{r}, \mathbf{v}\right)$, and self-consistent electric and magnetic fields $\mathbf{E}$ and $\mathbf{B}$ respectively. The velocity $\mathbf{v}$ has components parallel and perpendicular to the equilibrium magnetic field: $v_{\parallel}$ and $\mathbf{v}_{\perp}$ respectively. The collision operator is given by equation 1.9, and includes contributions from all species: $C\left[f_s\right] = \sum_{s'} C\left[f_s, f_{s'}\right]$.

Let us perform a change of variables [44] of equation (2.1) into coordinates defined by the orbit *gyrocenter*

$$\mathbf{R} \equiv \mathbf{r} - \frac{1}{\Omega_s} \mathbf{b} \times \mathbf{v}, \tag{2.2}$$

where $\Omega_s \equiv Z_s e B / m_s c$ is the frequency of cyclotron motion, and $\mathbf{b} \equiv \mathbf{B}/B$ is the unit vector along the magnetic field. The velocity space coordinates are defined by energy E, approximate magnetic moment μ, gyro-motion phase angle ϑ, and the sign of the parallel velocity $\sigma_{\parallel}$ (without which the velocity would not be fully defined

in terms of only E and μ). These quantities are defined respectively as follows:

$$E \equiv \tfrac{1}{2} m_s v^2 + Z_s e\phi, \tag{2.3}$$

$$\mu = \frac{m_s v_\perp^2}{2B}, \tag{2.4}$$

$$\vartheta \equiv \tan^{-1}\left(\frac{v_y}{v_x}\right), \tag{2.5}$$

$$\sigma_\parallel \equiv \frac{v_\parallel}{\left|v_\parallel\right|}. \tag{2.6}$$

The electrostatic potential is ϕ such that the electric field can be represented as $\mathbf{E} = -\nabla\phi - c^{-1}\partial\mathbf{A}/\partial t$, with vector potential $\mathbf{A}$ defined such that $\nabla \times \mathbf{A} = \mathbf{B}$. In equation (2.5), v_x and v_y are two mutually-perpendicular velocity components in the plane normal to the magnetic field.

In these coordinates, equation (2.1) becomes

$$\frac{\partial f_s}{\partial t} + \dot{\mathbf{R}} \cdot \frac{\partial f_s}{\partial \mathbf{R}} + \dot{E}\frac{\partial f_s}{\partial E} + \dot{\mu}\frac{\partial f_s}{\partial \mu} + \dot{\vartheta}\frac{\partial f_s}{\partial \vartheta} = C\left[f_s\right] + S_s, \tag{2.7}$$

where the over-dot notation represents the convective derivative in phase space:

$$\dot{g} \equiv \frac{dg}{dt} \equiv \frac{\partial g}{\partial t} + \mathbf{v} \cdot \nabla g + \frac{Z_s e}{m_s}\left(\mathbf{E} + \frac{1}{c}\mathbf{v} \times \mathbf{B}\right) \cdot \frac{\partial g}{\partial \mathbf{v}}, \tag{2.8}$$

for any function g.

2.1 Orderings

In this chapter, we are performing an expansion of equation (2.7) in the ratio of Larmor radius $\rho_s \equiv v_{ts}/\Omega_s$ (where $v_{ts} \equiv \sqrt{2T_s/m_s}$ is the thermal speed[1]) to an equilibrium length scale length a (here taken to be the minor radius of a tokamak):

$$\rho_s^* \equiv \frac{v_{ts}}{a\Omega_s}. \tag{2.9}$$

We expand the distribution function into an equilibrium slowly-varying in time and space, and a more rapidly-varying fluctuation (though still slow compared to the cyclotron frequency) :

$$f_s = F_{0s} + f_{1s} + f_{2s} \ldots. \tag{2.10}$$

Similarly, we expand the magnetic field as

$$\mathbf{B} = \mathbf{B_0} + \delta\mathbf{B} + \ldots \tag{2.11}$$

$$= \mathbf{B_0} + \delta B_\parallel \mathbf{b} + \nabla \times \left(A_\parallel \mathbf{b}\right) + \ldots. \tag{2.12}$$

Since we are not considering sonic flows, the $\mathbf{E} \times \mathbf{B}$ drift speed should be small compared to the thermal speed, and ϕ has *only* a small fluctuating component ($\phi = \delta\phi$). Similarly, unless otherwise stated, when we write the vector potential $\mathbf{A}$, it will refer only to the fluctuating magnetic field (such that $\delta\mathbf{B} = \nabla \times \mathbf{A}$), and not

[1] "Temperature" (and thus "thermal") will always refer to the second moment of the distribution function, divided by the zeroth moment. Later, we will find it convenient to define a different characteristic speed for alpha particles $v_\alpha \equiv \sqrt{2E_\alpha/m_\alpha}$. Care will be taken to specify which is being referred to when the time comes.

to the equilibrium field (which will always be denoted with $\mathbf{B}_0$).

We are developing a theory valid for when the fluctuating quantities δf_s, ϕ, $A_\parallel$, and $\delta B_\parallel$ vary on a characteristic timescale $\omega \sim v_{ts}/a$. Fluctuations are taken to be spatially anisotropic: they vary much more slowly along the magnetic field than in the plane perpendicular. A characteristic of gyrokinetics, indeed its greatest strength, is its ability to describe perpendicular fluctuations on the scale of a Larmor radius, which is beyond the reach of orderings such as drift kinetics [45] and MHD [46]. In return, however, gyrokinetics forfeits the ability to describe very fast drift velocities or cyclotron timescales.

The primary role of collisions is to determine the form of the equilibrium (including any necessary neoclassical corrections, for which collisions play a crucial role), and to provide dissipation in a turbulent cascade. If collisions are "strong" such that the collision frequency $\nu \sim \omega$, then it can be shown [35, 47] that F_{0s} is a Maxwellian distribution (1.27). However, for non-Maxwellian species, we shall order the collisions as weak in the sense that $C\left[F_{0s}\right] \sim \partial F_{0s}/\partial t$, at which timescale other physics come into play (particularly, transport due to turbulence). Formally, this means that collisions are ordered as $\nu \sim \mathcal{O}\left(\rho_s^{*3}\Omega_s\right)$, which is justified by the parameters for alpha particles in 1.1. The parallel length scale is characterized by wavenumber $k_\parallel \sim 1/qR \sim 1/a$, and the perpendicular length scale by $k_\perp \sim 1/\rho_s$.

To summarize, our orderings are:

$$\frac{\omega}{\Omega_s} \sim \frac{k_\parallel}{k_\perp} \sim \frac{\rho_s}{a} \sim \frac{\delta f_s}{F_{0s}} \sim \frac{\partial F_{0s}/\partial t}{\partial \delta f_s/\partial t} \ll 1, \tag{2.13}$$

while

$$C\left[F_{0s}\right] \sim \frac{\partial F_{0s}}{\partial t}. \tag{2.14}$$

2.2 Averaging operations

Before we proceed, we introduce the operations critical to our expansion: the gyroaverage and the turbulence average.

2.2.1 Gyroaverage

In our expansion, the gyrophase ϑ will be largely treated as a redundant (cyclic) coordinate, as it is in MHD. In contrast to MHD, this redundancy comes not from the small size of the Larmor radius, but from the fast timescale of the cyclotron motion. However, we must take care to ensure this averaging over gyrophase is done correctly, since we wish to capture the relevant dynamics on the Larmor radius scale.

To this end, let us define two complementary spatial averages: the gyroaverage at fixed gyrocenter $\mathbf{R}$,

$$\langle Q \rangle_{\mathbf{R}} \equiv \frac{1}{2\pi} \int_0^{2\pi} Q\left(\mathbf{r}\right) d\vartheta; \tag{2.15}$$

and the gyroaverage at fixed position $\mathbf{r}$,

$$\langle Q \rangle_{\mathbf{r}} \equiv \frac{1}{2\pi} \int_0^{2\pi} Q\left(\mathbf{R}\right) d\vartheta \tag{2.16}$$

for some arbitrary scalar Q. The former relation is perhaps the clearest; it represents

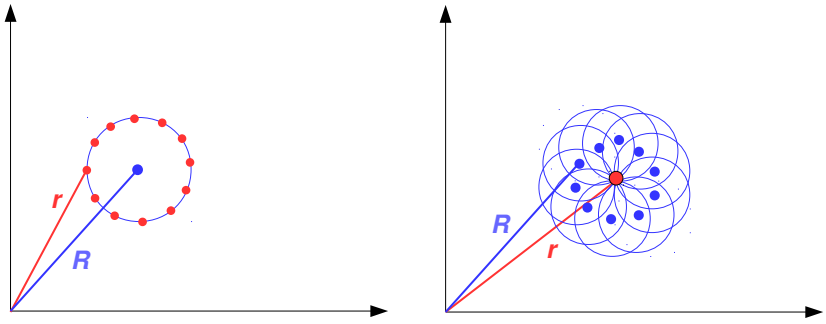

Figure 2.1: An illustration of the gyroaverage at fixed gyrocenter $\mathbf{R}$ (on left), and spatial position $\mathbf{r}$ (at right). In the latter, many particles with different gyrocenters $\mathbf{R}$ contribute to the charge at $\mathbf{r}$. Note that what is represented as a discrete set of particles over which to average (red dots on the left, blue dots on the right), is actually a continuous function, discretized only for the sake of illustration.

the average over the Larmor orbit of a particle whose gyrocenter is $\mathbf{R}$ and perpendicular speed is $v_\perp$. For example, in figure 1.3, the field experienced by the alpha particle (whose guiding center motion is described by $\mathbf{R}$) is the average of the field (which is a function $\mathbf{r}$) over its Larmor orbit. Conversely, equation (2.16) is a bit more subtle; it can be used to find, for example, the effective charge at a given point in space $\mathbf{r}$ as provided by many particles of perpendicular speed $v_\perp$ whose Larmor orbit happens to intersect with the point $\mathbf{r}$, and thus have a gyrocenter a distance $\rho = v_\perp/\Omega_s$ away from $\mathbf{r}$ (see figure 2.1). This latter average is used for the purposes of calculating fluctuating electromagnetic fields such as $\phi(\mathbf{r})$, as determined from the cyclotron-rotating charges at various gyrocenters $\mathbf{R}$.

Since our simulations are in a periodic flux-tube geometry, it is worth drawing attention to the form that the gyroaverage takes in Fourier space. Suppose the

quantity $\tilde{Q}(\mathbf{k})$ is the Fourier transform of $Q(\mathbf{r})$:

$$\tilde{Q} = \frac{1}{(2\pi)^{3/2}} \int Q e^{-i\mathbf{k}\cdot\mathbf{r}} \, \mathrm{d}^3\mathbf{r}, \tag{2.17}$$

$$Q = \frac{1}{(2\pi)^{3/2}} \int \tilde{Q} e^{i\mathbf{k}\cdot\mathbf{r}} \, \mathrm{d}^3\mathbf{r}. \tag{2.18}$$

Then, if $\langle Q \rangle_{\mathbf{R}}$ is the gyroaverage of Q, then its Fourier transform is:

$$\begin{aligned} \left\langle \tilde{Q} \right\rangle_{\mathbf{R}} &= \frac{1}{(2\pi)^{3/2}} \int Q e^{-i\mathbf{k}\cdot(\mathbf{R}+\mathbf{v}_\perp/\Omega_s)} \, \mathrm{d}^3\mathbf{R} \\ &= \frac{1}{(2\pi)^{3/2}} \int Q e^{-i\mathbf{k}\cdot\mathbf{R}} e^{-ik_\perp \rho \cos\eta} \, \mathrm{d}^3\mathbf{R} \\ &= J_0\left(\tfrac{k_\perp v_\perp}{\Omega_s}\right) \tilde{Q}, \end{aligned} \tag{2.19}$$

where η is the angle between $\mathbf{k}_\perp$ and $\boldsymbol{\rho} = \mathbf{v}_\perp/\Omega_s$, and J_0 is the zeroth-order Bessel function. In equation (2.19), we used the fact that $\mathrm{d}^3\mathbf{R} = \mathrm{d}^3\mathbf{r}$ when integrating over the entire spatial domain. The same relation holds for the gyroaverage at fixed $\mathbf{r}$. Therefore, the effect of the gyroaverage in Fourier space is simply multiplication by a Bessel function, a fact which is immensely useful in numerical calculations.

Note that successive applications of equation (2.15) and equation (2.16) do not undo each other. In fact, when integrating such a doubly-gyroaveraged function over velocity space, we will find the following identity useful:

$$\int \frac{e^{-v^2/v_{ts}^2}}{\pi^{3/2} v_{ts}^3} \left[J_0\left(\tfrac{k_\perp v_{ts}}{\Omega_s}\right) \right]^2 \mathrm{d}^3\mathbf{v} = e^{-k_\perp^2 \rho_s^2/2} I_0\left(\tfrac{k_\perp \rho_s}{2}\right) \equiv \Gamma_0\left(k_\perp \rho_s\right), \tag{2.20}$$

with zeroth-order modified Bessel function I_0.

An important property of the gyroaverage that we will make use of is in converting from the gyrophase derivative in one basis to another:

$$\left.\frac{\partial Q}{\partial \vartheta}\right|_{\mathbf{R}} = \left.\frac{\partial Q}{\partial \vartheta}\right|_{\mathbf{r}} - \frac{1}{\Omega_s}\mathbf{v}_\perp \cdot \nabla Q. \tag{2.21}$$

Using periodicity of any physical operand Q with respect to ϑ, the gyroaverage of equation (2.21) is:

$$\langle \mathbf{v}_\perp \cdot \nabla Q \rangle_{\mathbf{R}} = \Omega_s \left\langle \left.\frac{\partial Q}{\partial \vartheta}\right|_{\mathbf{r}} \right\rangle_{\mathbf{R}}. \tag{2.22}$$

Particularly, since ϑ is a velocity coordinate, note that if Q is not a function of velocity, such as the case of electromagnetic fields, then (2.22) vanishes:

$$\langle \mathbf{v}_\perp \cdot \nabla Q \rangle_{\mathbf{R}} = 0 \qquad \text{for } Q = Q(\mathbf{r}). \tag{2.23}$$

2.2.2 Turbulence average

Even though the equilibrium distribution F_{0s} is stationary with respect to the fluctuations, it still evolves in time, but on a longer timescale. How it evolves will depend on the steady-state turbulent fluxes (which can and do persist for long time scales). Therefore, we seek an averaging operation which obtains the long-time average of a fluctuating quantity:

$$\langle Q \rangle_T \equiv \frac{1}{T}\int_0^T Q(t')dt', \tag{2.24}$$

where T is a suitably large time (much larger than the correlation time).

In addition to time-averaging, we will also wish to average over a flux surface. From the theory of MHD equilibria, a flux surface is one on which magnetic field lines stay, and ψ labels such a surface. Particularly, if a coordinate system is defined by this ψ, a toroidal angle ζ (in which an axisymmetric magnetic field does not change by definition), and a poloidal coordinate θ, then $\nabla\psi$ is the coordinate perpendicular to the magnetic field:

$$\mathbf{b} \cdot \nabla\psi = 0. \tag{2.25}$$

Any flux function which is zero at the magnetic axis, and monotonic with respect to increasing radius can be a suitable generalized radial coordinate.

The *flux surface average* of a quantity Q is defined as:

$$\langle Q \rangle_\psi \equiv \lim_{\delta\psi \to 0} \frac{\int_{\delta\psi} Q \, \mathrm{d}^3\mathbf{r}}{\int_{\delta\psi} \mathrm{d}^3\mathbf{r}}, \tag{2.26}$$

where $\delta\psi$ is the volume between the flux surface labelled by ψ and an infinitesimally-close neighboring surface labelled by $\psi + \Delta\psi$. A defining property of the flux surface average is that it eliminates the parallel derivative operator:

$$\langle \mathbf{B} \cdot \nabla Q \rangle_\psi = 0. \tag{2.27}$$

Another useful identity is that the flux surface average of a divergence is:

$$\langle \nabla \cdot \mathbf{\Gamma} \rangle_\psi = \frac{1}{\mathcal{V}'(\psi)} \frac{\partial}{\partial\psi} \left(\mathcal{V}'(\psi) \langle \mathbf{\Gamma} \cdot \nabla\psi \rangle_\psi \right). \tag{2.28}$$

Here, $\mathbf{\Gamma}$ is an arbitrary vector, and $\mathcal{V} = \mathcal{V}(\psi)$ (whose derivative appears in equation 2.28) is the volume enclosed by the flux surface labelled by ψ.

In averaging over turbulent scales, we will often combine both operations (2.24) and (2.26) into the *turbulence average*:

$$\langle Q \rangle_t \equiv \left\langle \langle Q \rangle_\psi \right\rangle_T \tag{2.29}$$

2.3 The gyrokinetic hierarchy

In this section, the dynamical equation for the fluctuating part of the distribution function is derived as an expansion in $\epsilon \equiv \rho^*$. The strategy is as follows: at the fastest timescale we learn that the equilibrium distribution function is gyrotropic (*i.e.*, does not depend on gyrophase). This allows us to apply the gyroaverage operator at the next order, when we find that F_{0s} is constant along a field line (and is therefore a flux function). Furthermore, we find that the fluctuation f_{1s} is also gyrotropic. Next, we gyroaverage at order ϵ^2 to obtain the gyrokinetic equation. The transport equation at order ϵ^3, which finally deals with the time evolution of the equilibrium in terms of the time-averaged turbulent fluxes, is considered in the next section. Refer to table 2.1 to aid in the organization of the expansion.

At this point, it is helpful to calculate the coefficient time derivatives in equation (2.7) in a useful form considering our orderings. Firstly, μ is defined to be

Table 2.1: Organizing which terms appear at what order in the low-collisionality gyrokinetic expansion, when acting on which part of the distribution function. Order in $\epsilon = \rho^*$ is in terms of $\Omega_s f_s$ as it appears in equation (2.7). Here, all terms of higher order than ϵ^3 are ignored.

$\frac{\partial}{\partial t}$	$v_\parallel \mathbf{b}\cdot\nabla$	$\dot{\mathbf{R}}_\perp\cdot\nabla_\perp$	$\dot{E}\frac{\partial}{\partial E}$	$\dot{\vartheta}\frac{\partial}{\partial \vartheta}$	$C[\ ]$	Acting on ...
ϵ^3	ϵ^1	ϵ^2	ϵ^2	ϵ^0	ϵ^3	F_{0s}
ϵ^2	ϵ^2	ϵ^2	ϵ^3	ϵ^1		f_{1s}
ϵ^3	ϵ^3	ϵ^3		ϵ^2		f_{2s}
				ϵ^3		f_{3s}

exactly conserved (and is only approximately $m_s v_\perp^2/2B$ to leading order):

$$\dot{\mu} = 0, \tag{2.30}$$

so that term will always vanish in the expansion below. Also, since the cyclotron frequency is the dominant frequency, the change in gyrophase is dominated by the circular cyclotron motion:

$$\dot{\vartheta} \approx -\Omega_s. \tag{2.31}$$

For the other two convective derivatives in equation (2.7), it is convenient to define the acceleration from the fields:

$$\dot{\mathbf{v}} = \Omega_s \mathbf{v}\times\mathbf{b} - \frac{Z_s e}{m_s}\nabla\phi - \frac{Z_s e}{m_s c}\frac{\partial \mathbf{A}}{\partial t}, \tag{2.32}$$

where the first term is the centripetal acceleration from the magnetic field and the last two terms are the acceleration from the electric field. To find $d\mathbf{R}/dt$, we take the convective derivative of equation (2.2), keeping the equilibrium magnetic field

constant in time:

$$\begin{aligned}\dot{\mathbf{R}} &= \mathbf{v} - \mathbf{v}\cdot\nabla\left[\left(\frac{\mathbf{b}}{\Omega_s}\right)\times\mathbf{v}\right] - \frac{\mathbf{b}\times\dot{\mathbf{v}}}{\Omega_s} \\ &= \mathbf{v} - \mathbf{v}\cdot\nabla\left[\left(\frac{\mathbf{b}}{\Omega_s}\right)\times\mathbf{v}\right] + \frac{c}{B}\mathbf{b}\times\nabla\chi + \frac{1}{B}\mathbf{b}\times\frac{d\mathbf{A}}{dt},\end{aligned} \tag{2.33}$$

where the *electromagnetic potential* is

$$\chi \equiv \phi - \frac{1}{c}\mathbf{v}\cdot\mathbf{A}. \tag{2.34}$$

Upon gyroaveraging, equation 2.33 becomes:

$$\left\langle\dot{\mathbf{R}}\right\rangle_{\mathbf{R}} = v_\parallel\mathbf{b} + \mathbf{v}_{ds} + \frac{c}{B}\mathbf{b}\times\nabla\left\langle\chi\right\rangle_{\mathbf{R}}. \tag{2.35}$$

Here, we have defined the magnetic drift velocity of species s due to curvature and gradient of the magnetic field:

$$\mathbf{v}_{ds} \equiv \frac{1}{\Omega_s}\mathbf{b}\times\left(v_\parallel^2\mathbf{b}\cdot\nabla\mathbf{b} + \tfrac{1}{2}v_\perp^2\nabla\ln B\right). \tag{2.36}$$

In deriving (2.35), we noted that $\partial/\partial t \sim v_\parallel\mathbf{b}\cdot\nabla \ll \mathbf{v}_\perp\cdot\nabla$ in equation 2.8 and applied identity (2.23) so that, to leading order:

$$\left\langle\dot{\mathbf{A}}\right\rangle_{\mathbf{R}} = \left\langle\mathbf{v}_\perp\cdot\nabla\mathbf{A}\right\rangle_{\mathbf{R}} = 0. \tag{2.37}$$

Now, take the total time derivative of equation (2.3):

$$\begin{aligned}\dot{E} &= Z_s e\dot{\phi} + m_s \mathbf{v}\cdot\dot{\mathbf{v}} \\ &= Z_s e\frac{\partial\phi}{\partial t} - \frac{Z_s e}{c}\mathbf{v}\cdot\frac{\partial \mathbf{A}}{\partial t} \\ &= Z_s e\frac{\partial\chi}{\partial t},\end{aligned} \tag{2.38}$$

whose gyroaverage is:

$$\left\langle \dot{E}\right\rangle_{\mathbf{R}} = Z_s e\frac{\partial \left\langle\chi\right\rangle_{\mathbf{R}}}{\partial t}. \tag{2.39}$$

With the Fokker-Planck equation (2.7), combined with the relations (2.33), (2.38), (2.30), and (2.31), we proceed with the gyrokinetic expansion, using orderings that are described in the next section.

2.3.1 $\mathcal{O}\left(\Omega_s f_s\right)$

Upon applying the orderings equations (2.13)-(2.7) and expanding f_s, we find the leading-order equation is simply:

$$\frac{d\vartheta}{dt}\frac{\partial F_{0s}}{\partial\vartheta} = -\Omega_s\frac{\partial F_{0s}}{\partial\vartheta} = 0, \tag{2.40}$$

which means that F_{0s} is independent of gyrophase ϑ.

2.3.2 $\mathcal{O}(\epsilon\Omega_s f_s)$

At next order, we have:

$$v_\parallel \mathbf{b}\cdot\nabla F_{0s} - \Omega_s \frac{\partial f_{1s}}{\partial \vartheta} = 0. \tag{2.41}$$

First, we gyroaverage equation (2.41) to eliminate the last two terms. We discover that $\mathbf{b}\cdot\nabla F_{0s} = 0$, which says F_0 is constant along a field line.

We will be working in a flux tube geometry, which is densely populated with irrational surfaces. There would also be rational surfaces (perhaps low-order), where the magnetic field is periodic after a finite number of toroidal revolutions, but these are arbitrarily close to (and thus influenced by the finite-Larmor radius effects of) a nearby irrational surface. Therefore, we consider the only spatial dependence of F_{0s} to be the radial variable ψ because magnetic fields lines densely cover an irrational flux surface. In other words, $F_{0s} = F_{0s}(\psi, E, \mu)$ is a flux function in the sense of equation (2.25). Furthermore, since we are working with alpha particles, which enter the plasma isotropically, we will assume isotropy in velocity space and we thus have $F_{0s} = F_{0s}(\psi, E)$ exclusively.

The assumption of isotropy might give one pause in recalling that Hauff and colleagues [29] obtain different scalings for the transport of passing and trapped alpha particles. However, as pointed out by [28], this is actually an expansion in Larmor radius, and in order to obtain the "passing" scaling in [29], one must consider alpha particles of very small gyroradius, of which there is a vanishingly small number

(since the alpha particles of interest have high energy). In chapter 3, we verify that the latter scaling is dominant for the alpha particle population overall. Therefore, we consider ourselves justified in [31] by treating the alpha particles as isotropic.

Since the first term in equation (2.41) vanishes, we are left with the fact that $f_{1s} \equiv h_s$ is also independent of gyrophase. Following convention, we will use h_s from here on to refer to the perturbed distribution. We break from convention, however, in the fact that $f_{1s} = h_s$ instead of the usual relationship $f_{1s} = -q\phi F_{0s}/T_s + h_s$ in more traditional derivations of gyrokinetics [35, 40]. This is ultimately due to the fact that we include the potential ϕ in the energy variable, and there is therefore no large contribution from dE/dt that occurs at this order.

Consider the fact that $m_s v^2 \gg e\phi$ in equation (2.3) and Taylor expand $F_{0s}(E)$ about E for the small correction to $m_s v^2/2$.:

$$F_{0s}(E) = F_{0s}\left(\tfrac{1}{2} m_s v^2\right) + Z_s e\phi \frac{\partial F_{0s}}{\partial E} + \mathcal{O}\left(\epsilon^2 F_{0s}\right). \tag{2.42}$$

The second term is the so-called *adiabatic response* to the electrostatic potential ϕ. We will use it when calculating velocity moments of F_{0s} in the field equations.

2.3.3 $\mathcal{O}\left(\epsilon^2 \Omega_s f_s\right)$

At this order, the evolution of the fluctuating distribution function is found, while the equilibrium is still treated as a static background. The remaining terms

at this order are:

$$\left(\frac{\partial}{\partial t}+\mathbf{b}\cdot\nabla+\dot{\mathbf{R}}_{\perp}\cdot\nabla_{\perp}\right)h_s+\left(\dot{\mathbf{R}}_{\perp}\cdot\nabla_{\perp}+\dot{E}\frac{\partial}{\partial E}\right)F_{0s}-\Omega_s\frac{\partial f_{2s}}{\partial\vartheta}=0. \tag{2.43}$$

First, we must get rid of the terms involving f_{2s}. We accomplish this by gyroaveraging, noting that each remaining term includes at most one factor that depends on gyroangle:

$$\left(\frac{\partial}{\partial t}+\mathbf{b}\cdot\nabla+\left\langle\dot{\mathbf{R}}_{\perp}\right\rangle_{\mathbf{R}}\cdot\nabla_{\perp}\right)h_s+\left(\left\langle\dot{\mathbf{R}}_{\perp}\right\rangle_{\mathbf{R}}\cdot\nabla_{\perp}+\left\langle\dot{E}\right\rangle_{\mathbf{R}}\frac{\partial}{\partial E}\right)F_{0s}=0. \tag{2.44}$$

Before proceeding, we note that the term $\mathbf{v}_{\mathrm{d}s}\cdot\nabla F_{0s}$ plays a role in the neoclassical correction to the equilibrium distribution F_1. As noted earlier, in this dissertation we are focusing on the fluctuating part, h_s.

Combining equations (2.44), (2.35), and (2.39), we arrive at the collisionless *gyrokinetic equation*:

$$\begin{aligned}&\frac{\partial h_s}{\partial t}+\left(v_{\parallel}\mathbf{b}+\mathbf{v}_{\mathrm{d}s}+\mathbf{v}_{\chi}\right)\cdot\nabla h_s \\ &\qquad=-Z_s e\frac{\partial\left\langle\chi\right\rangle_{\mathbf{R}}}{\partial t}\frac{\partial F_{0s}}{\partial E}-\frac{\partial F_{0s}}{\partial\psi}\mathbf{v}_{\chi}\cdot\nabla\psi,\end{aligned} \tag{2.45}$$

where $\mathbf{v}_{\chi}$ is defined as:

$$\mathbf{v}_{\chi}=\frac{c}{B}\mathbf{b}\times\nabla\left\langle\chi\right\rangle_{\mathbf{R}}. \tag{2.46}$$

2.4 A note about the parallel nonlinearity

In the low-collisionality ordering presented here, there is no collision operator acting on h_s in equation (2.45). However, as pointed out by Krommes [48], this could leave us vulnerable to the entropy paradox, because dissipation is required to reach a steady-state. The gyrokinetic equation typically includes an appropriate collision operator [49–51] that provides this dissipation. By allowing extraordinarily-fine structure in velocity space that can occur in a situation with very weak collisions, it is possible that the nonlinear term $\dot{E}\,\partial h_s/\partial E$ could be promoted and needed in equation (2.45). This is the so-called *parallel nonlinearity*, whose name comes from the form in takes in $v_\parallel - \mu$ coordinates.

Previous work [52] studied in-depth the relevance of the parallel nonlinearity in gyrokinetic simulations, and it was found to have little to no effect on turbulence simulations with realistic values of ρ^*. However, that study did not account for the possibility of extremely fine-scale structure.

In order for the parallel nonlinearity to be of appreciable size, fine structure must develop velocity space. If this were the case, one would expect a lack of convergence in energy grid resolution. Figure 2.2 demonstrates that this is not the case for a sample ITG simulation including alpha particles in `GS2`. Note the lack of fine-scale structure and the lack of a trend in the flux at ever-increasing energy resolution. The alpha particles in the simulation have a low - but realistic - density, but are not taken to be perfectly trace. Furthermore, the alpha particles are collisionless. This is taken as evidence that the parallel nonlinearity would not

have a significant effect on the flux of alpha particles, even if it were included in the simulation and velocity space resolution were high enough to resolve it.

Through most of this thesis, we consider alpha particles of such low density that they are only passively affected by the turbulence. The cascade path (whether through spatial or velocity space structure, or some combination) of a high-energy collisionless passive species remains an open problem and deserves further study. Even if energy does end up at extremely small scales in velocity space, it is unclear if this is relevant when considering the larger-scale dynamics.

In addition, numerical simulations inevitably include some finite amount of numerical dissipation. While not strictly physical, this can at times act as a suitable proxy for collisions in gyrokinetic simulations. In order to reduce this numerical dissipation and allow extremely fine-scale velocity space structure, one requires a factor of ρ^{*-1} finer resolution, which remains beyond the capacity of current technology.

For these reasons, we ignore this term in equation (2.45), and in the simulations presented in this thesis. We justify this decision *a posteriori* by examining the dependence of the velocity space resolution on the turbulent fluxes. For consistency, by ignoring the parallel nonlinearity, we also exclude collisions acting on the perturbed distribution. In other words, if one is going to account for extremely fine scale velocity space structure in the fluctuating distribution, one must do so consistently.

Furthermore, we have the option to perform a subsidiary expansion on the orderings presented herein. Particularly, the assumption that $\tau_E \gg \tau_s$, used in the derivation of the slowing-down distribution, can be interpreted as a statement

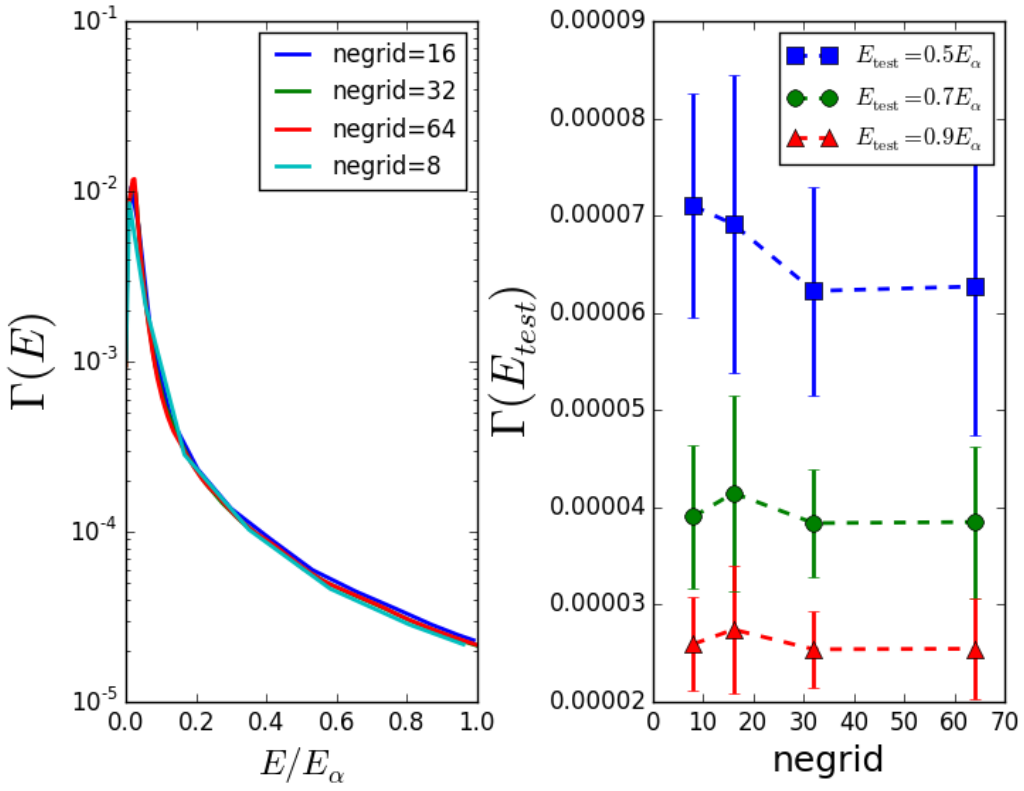

Figure 2.2: Demonstrating the convergence of $\Gamma_\psi(E)$ on energy grid resolution (`negrid`) for an electrostatic ITG case with collisionless alpha particles. The plot on the left shows the different resolutions super-imposed. On the right, a few select test energies are chosen and the radial flux at that energy is plotted as function of resolution.

that collisions are a bit stronger than the more general theory allows. If collisions are so strengthened, it would dissipate velocity space structure before the parallel nonlinearity becomes respectably large. This of course depends on this subsidiary expansion being valid, which we will find in chapter 3 is not the case at all energies. However, as energy increases (where we would expect the parallel nonlinearity to be most relevant), the confinement of alpha particles becomes stronger, as does this particular argument.

An important caveat is that the physics present in this term (the nonlinear effects of particle trapping due to a parallel electric field) accounts for the primary saturation mechanism of a few discrete unstable Aflvén eigenmodes [12, 53]. Therefore, our gyrokinetic simulations, which drop the parallel nonlinearity and its associated fine-scale velocity space structure, cannot be expected to capture this phenomenon.

While it would be surprising if the inclusion of the parallel nonlinearity makes a substantial difference to results in this dissertation, further study is of course welcomed.

2.5 Maxwell's equations

The dynamical equation (2.45) is not closed until one solves for the fields ϕ, $A_\parallel$, and $\delta B_\parallel$. In this section, we will apply the gyrokinetic orderings, keeping $F_{0s}(E, \psi)$ arbitrary. Since the fields are functions of spatial position $\mathbf{r}$ and we use the coordinate $\mathbf{R}$ for the distribution function, we will be making use of the gyroaverage

at constant $\mathbf{r}$ (see equation 2.16).

2.5.1 Poisson's equation / quasineutrality

To leading order, Poisson's equation is the quasi-neutrality relation of the equilibrium:

$$\sum_s Z_s e \left\langle \int F_{0s} \, \mathrm{d}^3\mathbf{v} \right\rangle_{\mathbf{r}} = \sum_s Z_s e n_s = 0. \tag{2.47}$$

The fluctuations, as well as the adiabatic response (2.42) play a role at next order:

$$\sum_s Z_s e \delta n_s = 0 \sum_s Z_s e \left(Z_s e \phi \int \frac{\partial F_{0s}}{\partial E} \, \mathrm{d}^3\mathbf{v} + \int \langle h_s \rangle_{\mathbf{r}} \, \mathrm{d}^3\mathbf{v} \right) = 0, \tag{2.48}$$

which can be rearranged to solve for ϕ:

$$\phi = -\frac{\sum_s Z_s e \int \langle h \rangle_{\mathbf{r}} \, \mathrm{d}^3\mathbf{v}}{\sum_s Z_s^2 e^2 \int \frac{\partial F_{0s}}{\partial E} \, \mathrm{d}^3\mathbf{v}}. \tag{2.49}$$

2.5.2 Parallel Ampere's Law

Consistent with our orderings, we ignore the displacement current in Ampere's law, leaving:

$$\nabla \times \mathbf{B} = -\nabla^2 \mathbf{A} = \frac{4\pi}{c} \mathbf{j}, \tag{2.50}$$

where we make use of the definition of $\mathbf{A}$ and our choice of the Coulomb gauge: $\nabla \cdot \mathbf{A} = 0$. The current density is $\mathbf{j} = \delta\mathbf{j}$, and under our assumption that F_{0s} is isotropic in velocity space (see the discussion at the beginning of this chapter), to

leading order, the parallel component reads:

$$-\nabla_\perp^2 A_\parallel = \frac{4\pi}{c}\sum_s Z_s e \int \langle h_s \rangle_{\mathbf{r}} \, v_\parallel \, \mathrm{d}^3\mathbf{v}. \tag{2.51}$$

2.5.3 Perpendicular Ampere's Law

To find a suitable equation for $\delta B_\parallel$, first operate on equation (2.50) with $\nabla\cdot\mathbf{b}\times$ to obtain:

$$\nabla\cdot\mathbf{b}\times(\nabla\times\delta\mathbf{B}) \approx \nabla_\perp^2 \delta B_\parallel = \frac{4\pi}{c}\nabla\cdot\sum_s Z_s e\int \langle \mathbf{b}\times\mathbf{v}h_s\rangle_{\mathbf{r}} \, \mathrm{d}^3\mathbf{v}. \tag{2.52}$$

Now, commute the gyroaverage outside of the integral, use the equation (2.21), and integrate by parts in ϑ to write the left-hand side as

$$\begin{aligned}\int \langle h_s \mathbf{b}\times\mathbf{v}_\perp\rangle_{\mathbf{r}} \, \mathrm{d}^3\mathbf{v} &= \left\langle \int \mathbf{v}_\perp \left(\frac{\partial h_s}{\partial\vartheta}\right)_{\mathbf{r}} \mathrm{d}^3\mathbf{v}\right\rangle_{\mathbf{r}}. \\ &= -\left\langle \int \frac{1}{\Omega_s}\mathbf{v}_\perp\left(\mathbf{v}_\perp\cdot h_s\right)\mathrm{d}^3\mathbf{v}\right\rangle_{\mathbf{r}}.\end{aligned} \tag{2.53}$$

Now substitute this into equation (2.52) and use the definition of Ω_s to obtain:

$$B_0\nabla_\perp^2\delta B_\parallel = -4\pi\sum_s m_s\int\langle \mathbf{v}_\perp\mathbf{v}_\perp : \nabla_\perp\nabla_\perp h_s\rangle_{\mathbf{r}} \, \mathrm{d}^3\mathbf{v}. \tag{2.54}$$

2.6 The low-collisionality transport equation

In this section, we follow the approach of references [35, 47] and break from the formal hierarchy to aid in the derivation of the transport equation. This equation determines the temporal evolution of the equilibrium F_{0s} due to collisions and turbulent transport. Its form is similar to that given in reference [41].

In working with the collision operator, we will find it convenient to use the speed coordinate v instead of $E = m_s v^2/2$. Furthermore, to keep the velocity space Jacobian separable, it is useful to use the pitch-angle coordinate λ for integrating:

$$\lambda \equiv \frac{\mu}{E} = \frac{v_\perp^2}{Bv^2}. \tag{2.55}$$

In these coordinates, the velocity space volume element is:

$$\mathrm{d}^3\mathbf{v} = \sum_{\sigma_\parallel} \mathcal{J}_v dv d\lambda d\vartheta = \sum_{\sigma_\parallel} \frac{Bv^2}{2} \frac{dv d\lambda d\vartheta}{\sqrt{1-\lambda B}}, \tag{2.56}$$

which defines the velocity space Jacobian of these coordinates:

$$\mathcal{J}_v \equiv \frac{Bv^2}{2\sqrt{1-\lambda B}}. \tag{2.57}$$

Return to the Fokker-Planck equation (2.7), and this time write it in flux-conservative form:

$$\frac{\partial}{\partial t}\left(\mathcal{J} f_s\right) + \sum_i \frac{\partial}{\partial z_i}\left(\mathcal{J} \dot{z}_i f_s\right) = \mathcal{J}\left(C\left[f_s\right] + S_s\right) \tag{2.58}$$

with a set of phase-space variables z_i, whose Jacobian is $\mathcal{J}$. In the coordinates $(\mathbf{R}, v, \lambda)$, this is the velocity space Jacobian to leading order[2]

$$\mathcal{J} = \mathcal{J}_v + \mathcal{O}(\epsilon) = \frac{Bv^2}{2\sqrt{1-\lambda B}} + \mathcal{O}(\epsilon). \tag{2.59}$$

Now, take the gyro-average of equation (2.58):

$$\begin{aligned} \frac{\partial}{\partial t}\langle \mathcal{J} f_s \rangle_{\mathbf{R}} + v_\parallel \mathbf{b}\cdot\nabla \langle \mathcal{J} f_s \rangle_{\mathbf{R}} + \frac{\partial}{\partial \mathbf{R}_\perp}\cdot\left\langle \mathcal{J}\dot{\mathbf{R}}_\perp f_s \right\rangle_{\mathbf{R}} \\ + \frac{\partial}{\partial v}\langle \mathcal{J}\dot{v} f_s\rangle_{\mathbf{R}} = \langle \mathcal{J}\left(C\left[f_s\right] + S_s\right)\rangle_{\mathbf{R}}. \end{aligned} \tag{2.60}$$

Now perform the turbulence average equation (2.29) directly on equation (2.60), noting that single powers of fluctuating quantities vanish by definition:

$$\begin{aligned} \frac{\partial}{\partial t}\left(\mathcal{J} F_{0s}\right) + \left\langle \frac{\partial}{\partial \mathbf{R}_\perp}\cdot\left\langle \mathcal{J}\dot{\mathbf{R}}_\perp h_s\right\rangle_{\mathbf{R}}\right\rangle_t + \left\langle \frac{\partial}{\partial v}\langle \mathcal{J}\dot{v} h_s\rangle_{\mathbf{R}}\right\rangle_t \\ = \langle \mathcal{J}\langle C\left[F_{0s}\right] + S_s\rangle_{\mathbf{R}}\rangle_t \end{aligned} \tag{2.61}$$

Note that the turbulence average includes a flux-surface-average, which annihilated the second term in equation (2.58). By equation (2.28), we can write the second term in equation (2.61) as:

$$\begin{aligned} \left\langle \frac{\partial}{\partial \mathbf{R}_\perp}\cdot\left(\left\langle \mathcal{J}\dot{\mathbf{R}}_\perp h_s\right\rangle_{\mathbf{R}}\right)\right\rangle_t &= \left\langle \nabla\cdot\left\langle \mathcal{J}\dot{\mathbf{R}}_\perp h_s\right\rangle_{\mathbf{R}}\right\rangle_t \\ &= \frac{1}{\mathcal{V}'(\psi)}\frac{\partial}{\partial\psi}\left[\mathcal{V}'(\psi)\left\langle\left\langle \mathcal{J} h_s \dot{\mathbf{R}}_\perp\cdot\nabla\psi\right\rangle_{\mathbf{R}}\right\rangle_t\right]. \end{aligned} \tag{2.62}$$

[2] We perform a change of variables from the phase-space Jacobian derived in reference [43]

Define the turbulence-averaged radial flux:

$$\Gamma_{\psi s} \equiv \left\langle \sum_{\sigma_\parallel} \int h_s \frac{c}{B} \left(\mathbf{b} \times \langle \nabla \chi \rangle_{\mathbf{R}}\right) \cdot \nabla \psi \frac{\pi B \mathrm{d}\lambda}{\sqrt{1-\lambda B}} \right\rangle_t \tag{2.63}$$

where the $\mathbf{v}_{\mathrm{d}s} \cdot \nabla h_s$ term vanishes because $\mathbf{v}_{\mathrm{d}s}$ is non-fluctuating, and thus its product with h_s vanishes upon time-averaging. Similarly, the flux in speed[3] is defined as:

$$\Gamma_{vs} \equiv \frac{Z_s e}{m_s v} \left\langle \sum_{\sigma_\parallel} \int h_s \frac{\partial \langle \chi \rangle_{\mathbf{R}}}{\partial t} \frac{\pi B \mathrm{d}\lambda}{\sqrt{1-\lambda B}} \right\rangle_t . \tag{2.64}$$

So now, when we take the λ integral of equation (2.61), which eliminates the pitch-angle part of the collision operator. After dividing through by v^2, we finally arrive at the transport equation for general isotropic F_0:

$$\begin{aligned} &\frac{\partial F_{0s}}{\partial t} + \frac{1}{\mathcal{V}'} \frac{\partial}{\partial \psi} \left(\mathcal{V}' \Gamma_{\psi s}\right) + \frac{1}{v^2} \frac{\partial}{\partial v} \left(v^2 \Gamma_{vs}\right) \\ &\quad = \frac{1}{v^2} \frac{\partial}{\partial v} \left(\nu_s^{(s)} v^3 F_{0s} + \frac{1}{2} \nu_\parallel^{(s)} v^4 \frac{\partial F_{0s}}{\partial v} \right) + S_s. \end{aligned} \tag{2.65}$$

If we integrate over velocity space by applying $\int 4\pi v^4 dv$ to equation (2.65), then we recover the usual transport equation for particle density. That is,

$$\frac{\partial n_s}{\partial t} + \frac{1}{\mathcal{V}'} \frac{\partial}{\partial \psi} \left(\mathcal{V}' \Gamma_{ps}\right) = S_{ps}, \tag{2.66}$$

[3]Where there is no ambiguity, we will also call this quantity the flux in energy even when working in the coordinate v

where the source of particles is $S_{ps} = \int S_s \, \mathrm{d}^3\mathbf{v}$, and

$$\Gamma_{ps} = 4\pi \int \Gamma_{\psi s} v^2 dv \tag{2.67}$$

is the particle flux. Similarly, we can obtain a pressure transport equation by taking the second moment of equation (2.65):

$$\frac{\partial p_s}{\partial t} + \frac{1}{\mathcal{V}'} \frac{\partial}{\partial \psi} \left(\mathcal{V}' q_s \right) - \int m_s v \Gamma_{vs} \, \mathrm{d}^3\mathbf{v} = S_{ps} \tag{2.68}$$

where the heat flux is

$$q_s = \int \tfrac{1}{2} m_s v^2 \Gamma_{\psi s} \, \mathrm{d}^3\mathbf{v}, \tag{2.69}$$

and the last term on the left hand side of equation (2.68) is the turbulent heat exchange. Note that an analogous term does not appear in equation (2.66) because, even though turbulence can heat an individual species (at the expense of another), it does not create particles.

We have nearly closed the problem. What remains is to calculate the steady-state radial (2.63) and energy (2.64) fluxes by numerically solving the gyrokinetic equation (2.45) for h_s. Once this is done, we can solve for the solution of the equilibrium that satisfies equation (2.65). However, the solution of equation (2.45) *itself* depends on the equilibrium, whose form we do not know yet! Later, we will solve this issue by making ample use of the trace approximation. In the next chapter, we proceed on the assumption that the slowing down distribution (1.20) is accurate and examine the gyrokinetic behavior of alpha particles.

Chapter 3: Testing alpha particle assumptions in electrostatic turbulence

In the previous chapter, we laid out the theory of low-collisionality gyrokinetics: an appropriate theory for the dynamics of energetic non-Maxwellian alpha particles. The nonlinear flux-tube code `GS2` was upgraded [31] to handle non-Maxwellian equilibria[1]. Armed with the ability to self-consistently model general energy distributions, we proceed to use this tool to validate several assumptions commonly used by the community to model alpha particles.

First, we will verify that alpha particles at realistic concentrations have little effect on electrostatic turbulence. Then we demonstrate that, if one is interested in the response of alpha particles to turbulence, the correct distribution function must be used, and the usual practice of using an "equivalent Maxwellian" produces incorrect results. Then, with the alpha particle flux calculated from simulations, we compare this to a characteristic collision time for ITER-like parameters. This is used to verify the assumption, used in the derivation of the slowing-down distribution (1.20), that $\tau_E \gg \tau_s$. It is found that this subsidiary ordering holds at high energies, where the transport is very weak, and at low energies, where collisions are strong.

[1] In the `alphas` branch as of revision 3682

However, at moderate energies, these timescales compete and one can have transport occurring on at least as fast of a timescale as collisions. This calls the slowing-down distribution (1.20) itself into question, the consequences of which are elaborated upon in chapter 5.

This chapter concerns itself with microturbulence driven by ITG, which is primarily electrostatic in nature, so we limit ourselves to the electrostatic limit of gyrokinetics. Finite-beta effects are expected to have a significant effect on alpha particle transport [29], and recent results imply that the presence of fast ions could have a stabilizing effect on the turbulence [54]. A linear study of some finite-beta effects is given in appendix A.

3.1 The trace-alphas approximation

At what concentration do alpha particles begin contributing to the turbulent dynamics? In any of the existing or planned fusion devices, the fraction n_α/n_e is expected to peak at most around 1% [1]. Considering that alpha particles have such high energy, it is not immediately obvious whether or not they contribute to the electrostatic nonlinear dynamics of the plasma.

When the density of a charged species is negligible, so is its contribution to the right hand side of the quasineutrality condition (2.48). In the limit of $n_\alpha \to 0$, ϕ no longer depends on the perturbation h_α, in which case the gyrokinetic equation

(2.45) is linear in h_α. We can therefore write the gyrokinetic equation (2.45) as:

$$\mathcal{L}\left[h_\alpha, \phi\right] = -Z_\alpha e \frac{\partial F_{0\alpha}}{\partial E} \frac{\partial \left\langle \phi \right\rangle_{\mathbf{R}_s}}{\partial t} - \frac{c}{B}\mathbf{b} \times \nabla \left\langle \phi \right\rangle_{\mathbf{R}_s} \cdot \nabla F_{0\alpha}, \tag{3.1}$$

where $\mathcal{L}$ is the linear operator defined by the left hand side of equation (2.45), and ϕ is treated as a given function of space and time, determined by the turbulent dynamics of the other, non-negligible species. Note that this does not imply that the usually-nonlinear $\mathbf{E} \times \mathbf{B}$-drift term in (2.45) is ignored. Invert equation (3.1) to obtain h_α and plug into equation (2.67). It follows that we can write the particle flux in the form [25]:

$$\frac{R}{n_\alpha}\Gamma_\alpha = D\frac{R}{L_{n_\alpha}} + D_E \frac{R}{L_{T_e}} + V_p. \tag{3.2}$$

From left to right, the terms are: particle diffusion, thermodiffusion, and the pinch flux (flux at zero gradient). Following reference [25], the *electron* temperature gradient appears here because that is the dominant dependence of the v_c parameter when a single ion species is present with $Z_i = 1$ and $n_i \approx n_e$ in equation (1.22). This ability to rigorously write the flux in terms of diffusion coefficients is one of the benefits of the trace approximation, and one that we will revisit throughout this dissertation.

3.1.1 Linear theory

A first estimate of how much of an effect alphas have on the plasma can be obtained by examining the linear growth rate of an unstable ITG mode. We examine

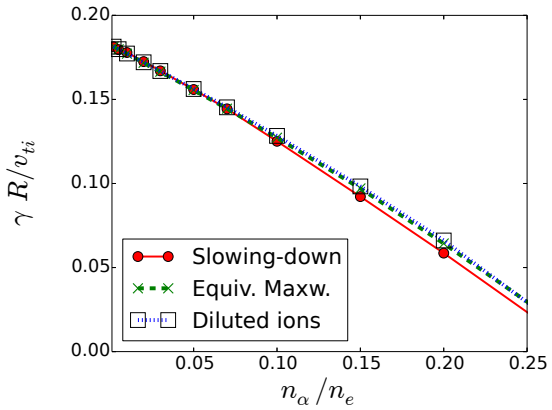

Figure 3.1: Comparison of linear growth rates for different models of alpha particles at a range of concentrations. Calculations were performed by running `GS2` for a single $k_y = 0.3$ mode of the cyclone base case [2] with $R/L_{n\alpha} = R/L_{ni} = R/L_{ne} = 2.2$. Agreement between all three is within 1% up to $n_\alpha/n_e \approx 0.05$, and still within 10% up to an impossibly-large $n_\alpha/n_e \approx 0.15$. Note that the equivalent Maxwellian and diluted-ion models are nearly identical.

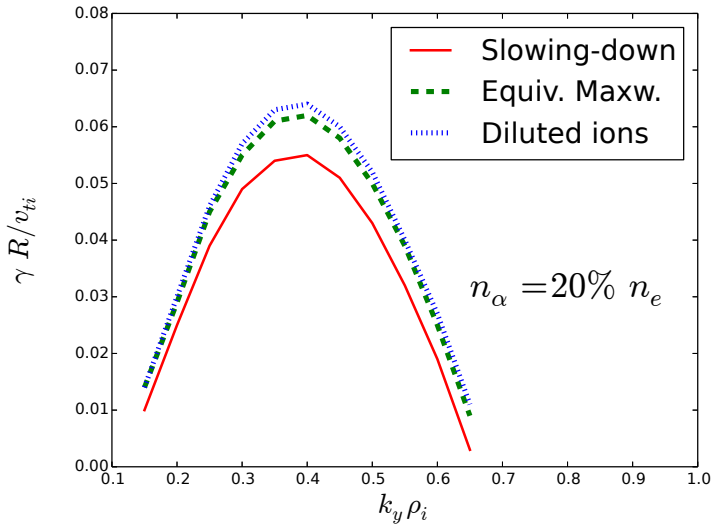

Figure 3.2: Growth rate spectrum of linear ITG growth rate at a 20% alpha particle concentration. Same case as figure 3.1.

the frequency and growth rate of the $k_y\rho_i = 0.4$ poloidal mode as alpha particles are introduced at ever-increasing density in figure 3.1. The growth rate decreases with increasing alpha particle concentration, but only changes by about 5% up to an alpha particle concentration of 2%. Even at a concentration of 20%, we still see in figure 3.2 that there is no qualitative and little quantitative difference in the poloidal spectrum. We find that the effect of a small population of alpha particles is negligible, at least linearly.

As n_α/n_e increases, the relative fraction of main ions (whose temperature gradient drives the instability) must decrease to compensate and maintain equilibrium quasineutrality, resulting in a dilution of the turbulence [55,56]). It could be argued whether this effect alone is responsible for the change in growth rate shown in figures 3.1 and 3.2. Therefore, what is also shown (labelled "diluted ions") is the case where alphas do not contribute to the field at all, even at significant density. Indeed, it takes very high concentrations of alpha particles ($\gtrapprox 10\%$) to distinguish between the different models (see section 3.2 for an explanation of the "equivalent Maxwellian" model), and no model at all. This suggests that, even beyond realistic reactor densities, the primary effect of alpha particles on electrostatic turbulence is only to dilute the ITG-driving ions, introducing no particularly interesting electrostatic effects of their own.

3.1.2 Nonlinear simulations

We then proceed to demonstrate that these conclusions continue to hold in turbulence. We turn on the nonlinear term in equation (2.45) and examine the evolution of fluxes to an approximate steady-state. The time evolution to saturation of the total heat flux is shown in figure 3.3. In this case, the decrease in outward total heat flux is due to the combined effect of: 1) alpha particles carrying some heat inward; and 2) reducing the ITG drive by the main ions. An inward heat and particle flux for the alpha particles is seen because there is an inward flux of alphas due to the second two terms in equation 3.2, but the alpha density gradient is not strong enough in this case (with $R/L_{n\alpha} = R/L_{ni}$) for the diffusion term to dominate and drive the alpha particles outward.

Even at high concentrations of alpha particles ($\sim$ 10%), the effect on the turbulence is indistinguishable from that of mere dilution of the main ions, consistent with linear theory. This is demonstrated in figure 3.5, which shows only a 10% difference in the heat fluxes between the case with alpha particles and that without. In the latter, only the ion dilution effect is taken into account.

To see the effect this has on alpha transport, let us also compare the alpha particle flux. If alphas have little or no effect on the turbulence, we would then expect Γ_α/n_α to be constant as the concentration changes. The time-averaged value of Γ_α/n_α compared to alpha particle concentration is shown in figure 3.4. It is clear that no significant change occurs below a concentration of about 5%.

As mentioned previously, by assuming energetic ions are of negligible density,

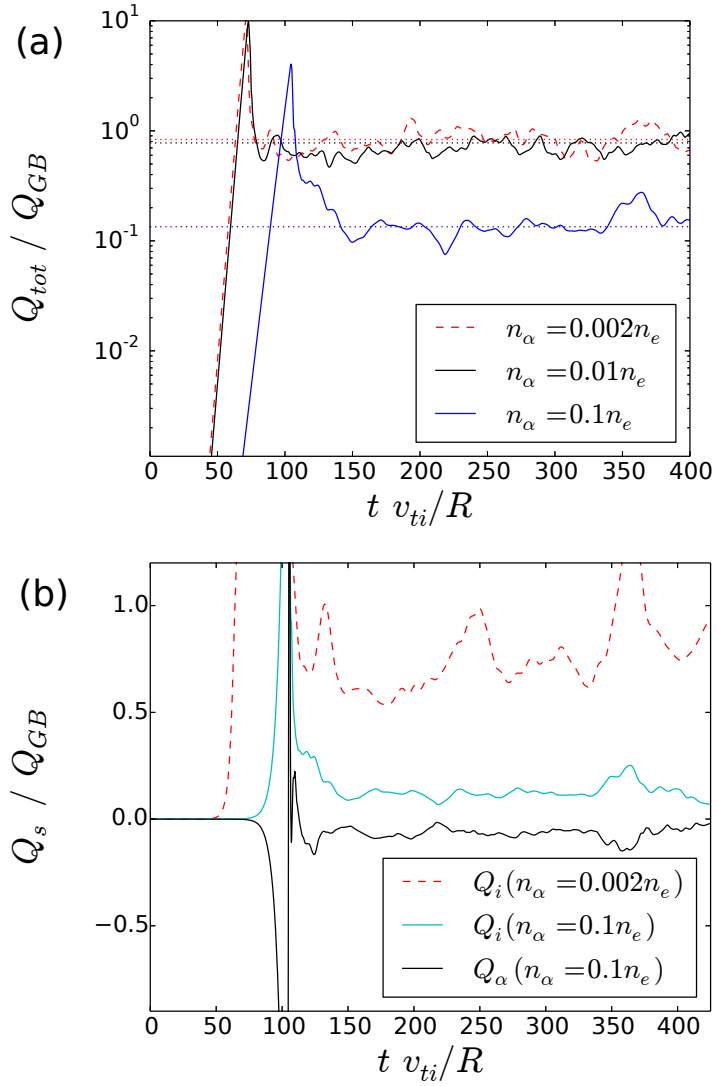

Figure 3.3: Time evolution of the turbulent heat flux. The dotted horizontal lines are the time-averaged heat fluxes for the different concentrations of alpha particles. Here, the normalization factor is $Q_{GB} \equiv 2 n_e v_{ti} T_i \rho^{*2}$. (a) shows the total heat flux for different alpha particle concentrations, and (b) shows the breakdown by species at $n_\alpha/n_e = 0.1$, compared to the ion heat flux at negligible alpha density.

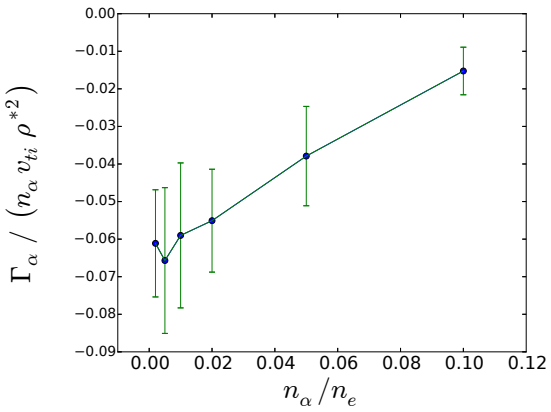

Figure 3.4: Steady-state turbulent flux of alpha particles as a function of alpha particle concentration. Units are gyro-Bohm normalised by the alpha particle density. Error bars indicate the standard deviation of the departure of fluctuations from the time average, and is intended to put into context the variations of flux at low concentration.

it can be shown [28, 29] that for almost all pitch angles (the dependence on which is not covered in this work since we are focusing on isotropic alpha particles), the diffusion coefficient scales like $E^{-3/2}$. To make sense of this quantity, consider the energy-dependent analogue of equation (3.2) consistent with the energy-dependent flux of equation (2.63):

$$\frac{R}{F_{0\alpha}(E)}\Gamma_\alpha(E) = D(E)\frac{R}{L_{n_\alpha}} + D_E(E)\frac{R}{L_{T_e}} + V_p(E). \tag{3.3}$$

Note that, with this definition, $D(E)$ has the same units as its energy-integrated counterpart. By performing several nonlinear runs with a range of density gradients, a linear fit of $\Gamma_\alpha(E)$ versus R/L_{n_α} was obtained, the slope of which is proportional to the diffusion coefficient $D(E)$. The results are plotted in figure 3.6, with a scaling and approximate magnitude consistent with references [28, 29].

The conclusion of this section is to confirm that in the presence of electrostatic

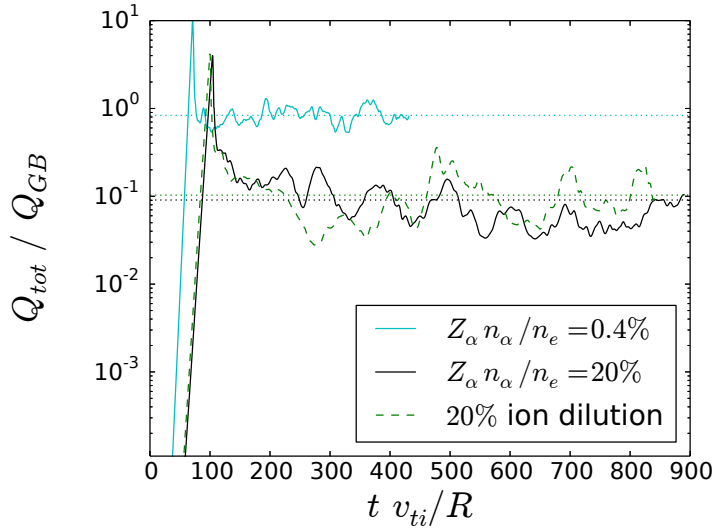

Figure 3.5: Time evolution of the turbulent heat flux, comparing the case of: a small alpha population (solid cyan), a large alpha population (solid black), and a case where the presence of alphas is "simulated" only by diluting the ion density (dashed green)

turbulence, an energetic species has little effect up to a concentration of at least 2%. However, even beyond such a density, they do not have much of a direct effect on the turbulence. Instead, their effect is simply to dilute the main ions, decreasing the ITG drive. This dilution effect is the dominant influence of fast ions up to at least a concentration of 10%.

3.2 The equivalent-Maxwellian approximation

Even though a concentration of fast ions appears to have little effect on electrostatic turbulence, the response of alpha particles to that turbulence depends quite explicitly on the equilibrium distribution function, and especially its radial gradient.

To take advantage of existing tools to solve the gyrokinetic equation for Maxwellian equilibria, it is often suggested that, instead of representing the alpha particles with

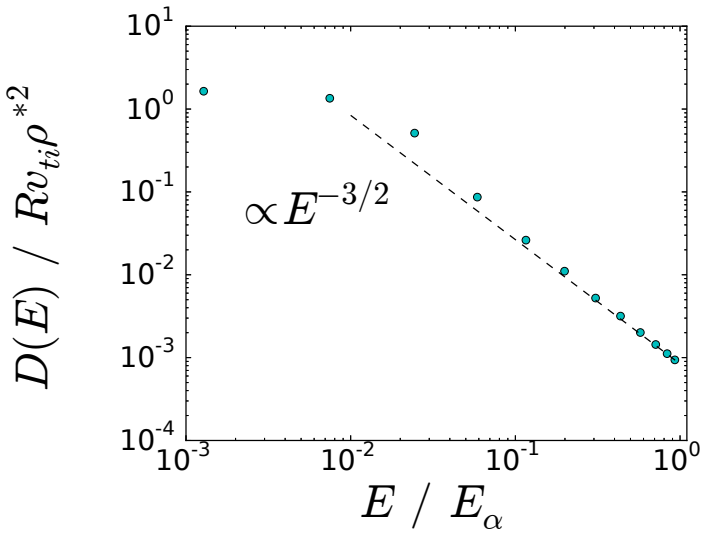

Figure 3.6: Diffusion coefficient of trace alpha particles ($n_\alpha = 0.002 n_e$) as a function of energy.

a slowing-down distribution (1.20), one could instead define a Maxwellian that has the same temperature, and that this may provide satisfactory results. This method of modelling alpha particles has been widely used in gyrokinetic studies of alpha particles [15, 17, 19, 28, 30, 54, 57, 58].

3.2.1 Definitions

The zeroth and second moment of the slowing-down distribution, equation (1.20), can be evaluated analytically. We use these to define an effective temperature $T_{\text{eff}} = T_{\text{eff}}\,(v_c/v_\alpha)$ such that:

$$3 n_\alpha T_{\text{eff}} = \int F_{M\alpha} m_\alpha v^2 \,\mathrm{d}^3\mathbf{v} = \int F_{S\alpha} m_\alpha v^2 \,\mathrm{d}^3\mathbf{v}, \tag{3.4}$$

so [15]:

$$T_{\text{eff}} = \frac{m_\alpha v_c^2}{2\ln\left(1+v_\alpha^3/v_c^3\right)} \times \left[\frac{v_\alpha^2}{v_c^2} - \frac{1}{3}\ln\left(\frac{v_\alpha^2 - v_\alpha v_c + v_c^2}{\left(v_\alpha + v_c\right)^2}\right) - \frac{1}{2\sqrt{3}}\tan^{-1}\left(\frac{2v_\alpha - v_c}{\sqrt{3}v_c}\right) - \frac{\pi}{3\sqrt{3}}\right]. \tag{3.5}$$

However, the gradient of the equivalent Maxwellian also appears in the gyrokinetic equation (2.45), so we need a way of calculating it. Fortunately, v_c (hence T_{eff}) is a known function of ion and electron parameters, so we can find the effective Maxwellian temperature gradient scale length by using the chain rule, similarly to equation (1.22):

$$\frac{\nabla F_{M\alpha}}{F_{M\alpha}} = \frac{\nabla n_\alpha}{n_\alpha} + \frac{1}{T_{\text{eff}}}\frac{\mathrm{d}T_{\text{eff}}}{\mathrm{d}v_c}\left(\frac{\partial v_c}{\partial T_e}\nabla T_e + \frac{\partial v_c}{\partial n_i}\nabla n_i + \frac{\partial v_c}{\partial n_e}\nabla n_e\right)\left(\frac{E}{T_{\text{eff}}} - \frac{3}{2}\right). \tag{3.6}$$

We take the derivative of equation (3.5) and write down an expression for $R/L_{T_{\text{eff}}}$ as a function of $x \equiv v_c/v_\alpha$:

$$\frac{R}{L_{T_{\text{eff}}}} = \frac{R}{L_{v_c}}\frac{1}{\ln\left(1+x^{-3}\right)}\left[\frac{1}{1+x^3} - \frac{x^2}{3}\left(\frac{E_\alpha}{T_{\text{eff}}}\right)\frac{2\pi}{3\sqrt{3}} + \frac{2}{\sqrt{3}}\tan^{-1}\left(\frac{2-x}{\sqrt{3}x}\right) + \frac{1}{3}\ln\left(\frac{x^2-x+1}{\left(1+x\right)^2}\right) - \frac{x}{\left(1+x\right)\left(x^2-x+1\right)}\right] \tag{3.7}$$

where R/L_{v_c} is given by equation (1.25).

3.2.2 Linear theory

Proceeding in a manner analogous to section 3.1, we analyze the linear mode that results from a concentration of alpha particles using the equivalent Maxwellian versus the slowing-down distribution. Consistent with [15] (which used a different test case), we find that the growth rates for the slowing-down and Maxwellian distributions in the cyclone base case follow each other very closely up to relatively high concentration (see figure 3.1). This is unsurprising given the conclusion of the previous section: that a modest concentration of alpha particles plays no electrostatic role except dilution.

We proceed to ask the inverse question: how do alpha particles respond to a given linearly unstable eigenfunction, and how does the equilibrium distribution function used affect the result? We can use quasilinear theory to estimate the fluxes with the same method as [25]. That is, for each set of parameters, we choose a single unstable mode and calculate the alpha particle flux (equation 2.67) as a function of time. Because it is exponentially growing, we must normalize it to a quantity growing at the same rate, such as the flux of ash. This only works because in both cases, the density is taken to be trace, otherwise there would be a small but finite difference in exponential growth rates. This ratio of alpha flux to ash flux in response to the linear eigenfunction is what we calculate.

Consider again the fact that, in the trace limit, the right-hand side of the gyrokinetic equation (3.1) is linear in the equilibrium gradients. Then, equation (3.2) holds, and the particle flux is easily found after finding the coefficients D,

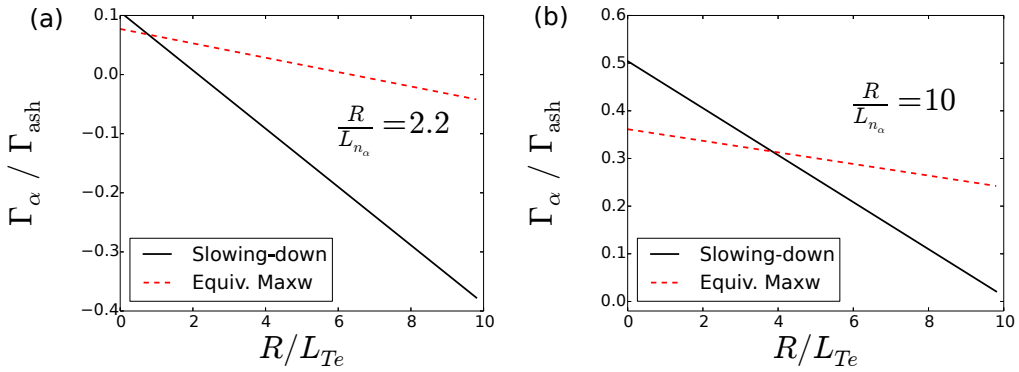

Figure 3.7: Quasilinear alpha particle flux determined by finding linear fits for the coefficients in equation (3.2). Showing the dependence on the electron temperature gradient for (a) $R/L_{n_\alpha} = R/L_{n_i} = 2.2$, and (b) $R/L_{n_\alpha} = 10$.

D_E, and V_p. After fitting these coefficients to a series of linear simulations for the cyclone case, we plot the dependence of particle flux on the dominant parameters (R/L_{n_α} and R/L_{T_e}) in figure 3.7. From inspection, one can see that, depending on the problem parameters, we can achieve anything from very good to very poor agreement between the slowing-down distribution and the equivalent Maxwellian.

3.2.3 Nonlinear simulations

The disagreement between the flux of Maxwellian alphas versus the slowing down distribution continues for nonlinear simulations (see figure 3.8). Using the same parameters as before, figure 3.8 compares the total heat flux for the two distributions. Since they are both sufficiently below the threshold to be considered trace, there is little statistical difference in the total heat flux between these two, as would be expected. However, the turbulent fluxes shown in figure 3.8 demonstrate that the equivalent Maxwellian gets the wrong direction of the alpha particle flux and is off by more than an order of magnitude.

While we do not claim that this strong of a disagreement will be seen in all relevant cases, the observation that: a) such an agreement is so sensitive to the parameters of the problem; b) a drastic difference is found for such a common test case as cyclone; and c) that such an agreement, when it does exist by coincidence, has no physical basis, should be enough to convince the reader that any results for alpha particle flux obtained by using an equivalent-Maxwellian ought to be treated with skepticism. Any disagreement in the fluxes is especially troublesome if one is performing a critical-gradient analysis to determine the alpha particle profile. From inspection of figure 3.7, one can observe very different critical gradients (the gradient for which $\Gamma_\alpha \to 0$) between the two distribution functions.

3.2.4 Explanation of discrepancy

To explain this disagreement, consider the $\nabla F_{0\alpha}$ term in the gyrokinetic equation (2.45). For a Maxwellian distribution, $\nabla F_{M\alpha}/F_{M\alpha}$ is linear in energy, but the gradient of the slowing-down distribution has a different energy dependence as in equation (1.22). From figure 3.9, we see that when $E \sim T_i$ (near which the interaction with the ion-scale turbulence is expected to be the strongest), the gradient of $F_{0\alpha}$ is off by over an order of magnitude. This stark difference in the right hand side of equation (2.45) ultimately carries through to the particle flux, resulting in the discrepancies in figures 3.7 and 3.8.

We conclude that the equivalent Maxwellian approximation is wrong precisely because it fails to capture the energy dependence of $\nabla F_{0\alpha}$, and at least sometimes

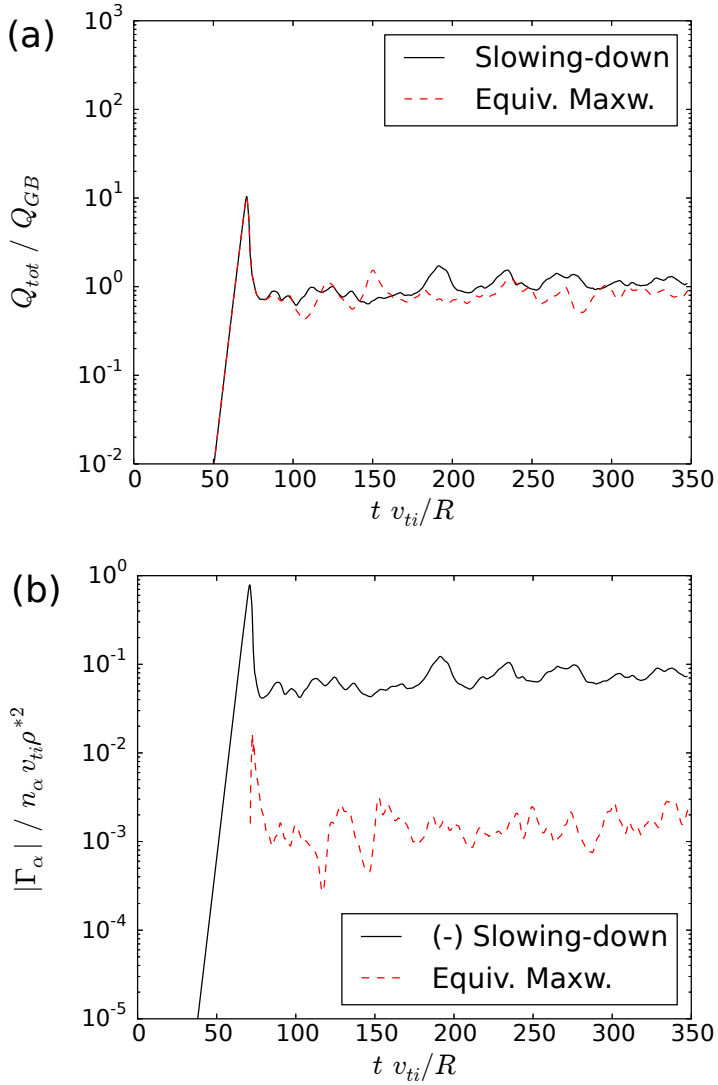

Figure 3.8: Time evolution of (a) total heat flux, and (b) alpha particle flux. Comparing two models for the alphas particles: the slowing down distribution (solid black), and the equivalent Maxwellian (dashed red). In both cases, the alpha particle concentration is 0.1%. The negative particle flux for the slowing-down distribution is shown, since the signs do not agree.

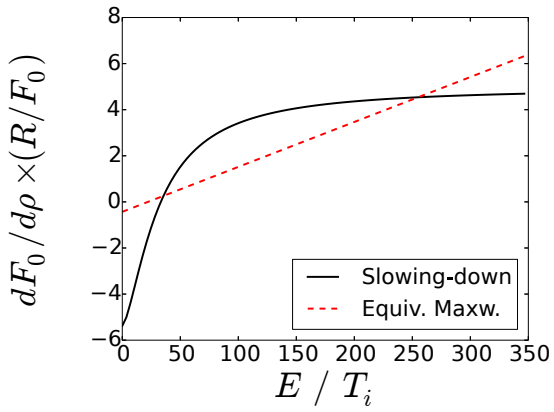

Figure 3.9: Comparing the energy dependence of the radial spatial derivative of $F_{0\alpha}$ for the two models of alpha particle distributions. In both cases, the gradient is found from the density gradient of alpha particles, and the gradient of v_c, which can be found as a function of the equilibrium parameters of other species, particularly T_e.

strongly disagrees at the most relevant energies. In the particle-diffusive limit, where the gradient of $F_{0\alpha}$ is dominated by ∇n_α, this energy dependence is not as important, and one would expect the equivalent Maxwellian to predict at least the correct order of magnitude. Even so, if one wishes to find the gradient $R/L_{n\alpha}$ that eliminates the alpha particle flux, the balance with D_E (which *is* sensitive to the energy dependence of $\nabla F_{S\alpha}$) and V_p in equations (3.2) and (3.3) is necessary.

3.2.5 Correcting the equivalent Maxwellian

We can take advantage of the trace approximation to decompose the energy dependence of the transport coefficients given in equation (3.3). Doing so will allow one to obtain the fluxes that one would get from a simulation with the slowing-down distribution, provided the coefficients D, D_E and V_p are known from a series of equivalent Maxwellian simulations.

Consider again the linearity of (3.1). Decompose the right hand side into terms

with the known velocity dependences of $\partial F_0/\partial E$ and ∇F_0 factored out. When using the slowing-down distribution, we can write the gyrokinetic equation as:

$$\frac{1}{F_{S\alpha}}\mathcal{L}\left[h_\alpha\right] = a_0 M_0^{(S)} + a_1 M_1^{(S)}\frac{R}{L_{n_\alpha}} + a_2 M_2^{(S)}\frac{R}{L_{v_c}}. \tag{3.8}$$

Analogously for the equivalent Maxwellian:

$$\frac{1}{F_{M\alpha}}\mathcal{L}\left[h_\alpha\right] = a_0 M_0^{(M)} + a_1 M_1^{(M)}\frac{R}{L_{n_\alpha}} + a_2 M_2^{(M)}\frac{R}{L_{v_c}}. \tag{3.9}$$

The following quantities are defined:

$$M_0^{(S)} = -E_\alpha\frac{\partial}{\partial E}\ln F_{S\alpha} = \frac{3}{2}\frac{v^2 v_\alpha}{v_c^3 + v^3} \tag{3.10}$$

$$M_0^{(M)} = -E_\alpha\frac{\partial}{\partial E}\ln F_{M\alpha} = \frac{E_\alpha}{T_{\text{eff}}} \tag{3.11}$$

$$M_1^{(S)} = M_1^{(M)} = 1 \tag{3.12}$$

$$M_2^{(S)} = v_c\frac{\partial}{\partial v_c}\ln F_{S\alpha} = \frac{3v_\alpha^3}{v_c^3 + v_\alpha^3}\frac{1}{\ln\left(1 + v_\alpha^3/v_c^3\right)} - \frac{3v_c^3}{v_c^3 + v^3} \tag{3.13}$$

$$M_2^{(M)} = v_c\frac{\partial T_{\text{eff}}}{\partial v_c}\frac{\partial}{\partial T_{\text{eff}}}\ln F_{M\alpha} = \left(\frac{E}{T_{\text{eff}}} - \frac{3}{2}\right)\frac{L_{v_c}}{L_{T_{\text{eff}}}}, \tag{3.14}$$

where L_{v_c} and $L_{T_{\text{eff}}}$ are given by equations (1.25) and (3.7) respectively. These factors together contain the only dependence on F_0 that appear in the gyrokinetic equation. The other factors a_0, a_1, and a_2 are allowed to depend on velocity, but not through F_0. Therefore, these factors are the same in both equations (3.8) and (3.9), and the dependence on the equilibrium distribution is entirely contained in the *a priori*-known functions M_0, M_1, and M_2.

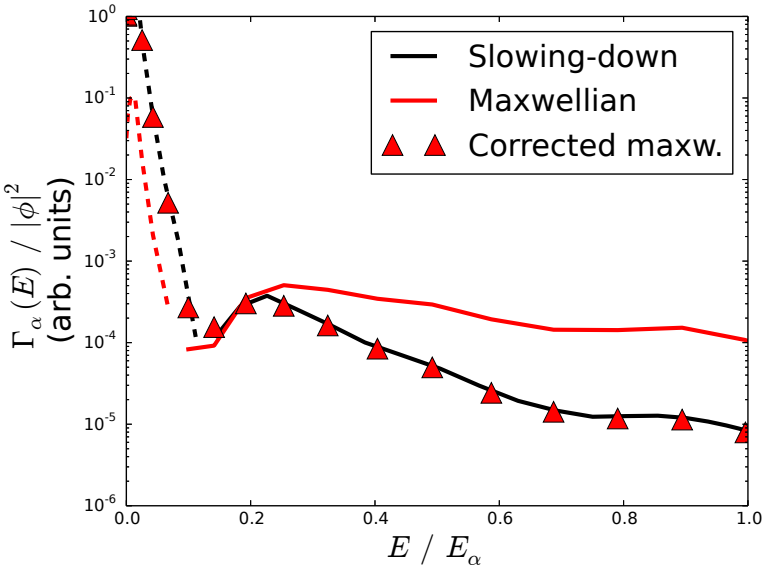

Figure 3.10: Quasilinear radial flux for the $k_y\rho_i = 0.3$ mode normalized to the total amplitude of ϕ. Triangles represent adjustments made directly to the equivalent Maxwellian via equations (3.15) to (3.17). Dashed lines represent negative values.

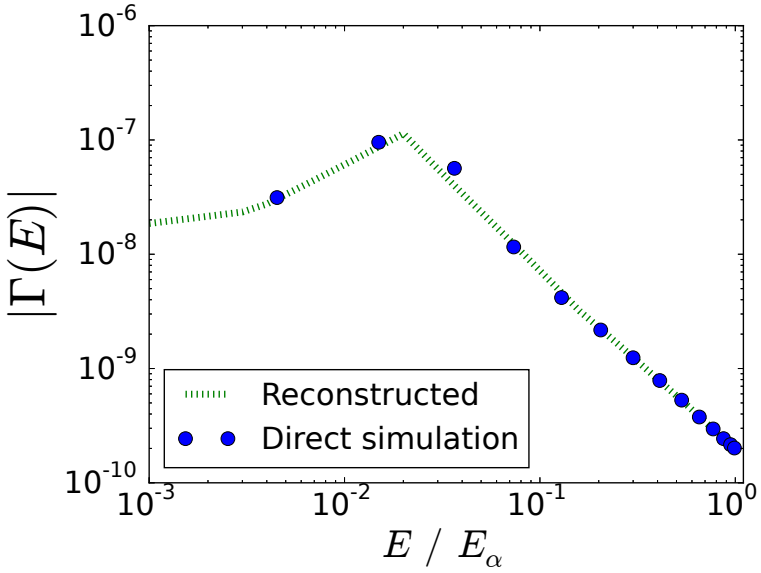

Figure 3.11: Turbulent radial flux of alpha particles for the ITER case of section 3.3. Blue dots are the energy-dependent fluxes as run with the slowing down distribution, and the dotted green line is the reconstructed flux from a simulation with Maxwellian alphas, using equations (3.15) to (3.17).

Suppose we know, from a simulation campaign using Maxwellian distributions, the energy-dependent diffusion coefficients $D^{(M)}(E)$, $D_E^{(M)}(E)$, and $V_p^{(M)}(E)$. We can find the corresponding turbulent transport coefficients $D^{(S)}(E)$, $D_E^{(S)}(E)$, $V_p^{(S)}(E)$, and hence the radial flux $\Gamma_\alpha(E)$ for the slowing-down distribution, even if a gyrokinetic simulation with $F_{S\alpha}$ was never run. To convert between the two:

$$D^{(S)}(E) = D^{(M)}(E) \tag{3.15}$$

$$D_E^{(S)}(E) = \frac{M_2^{(S)}}{M_2^{(M)}} D_E^{(M)}(E) \tag{3.16}$$

$$V_p^{(S)}(E) = \frac{M_0^{(S)}}{M_0^{(M)}} V_p^{(M)}(E), \tag{3.17}$$

and apply equation (3.3). For the case whose nonlinear particle flux is shown in figure 3.8, these relationships were applied to the quasilinear flux of the fastest-growing mode. Figure (3.10) shows the $\Gamma_\alpha(E)$ that results when the equivalent Maxwellian is corrected for a linear simulation, and figure (3.11) is for a nonlinear turbulent simulation.

This technique of finding the turbulent flux of one distribution in terms of that of another, will be liberally applied in chapter 4 where a transport model is built around it.

3.3 Confinement of alpha particles in ITG turbulence

Implicit in the use of the slowing-down distribution (1.20) is the assumption that alpha particles are well-confined in the sense that all collisional slowing-down

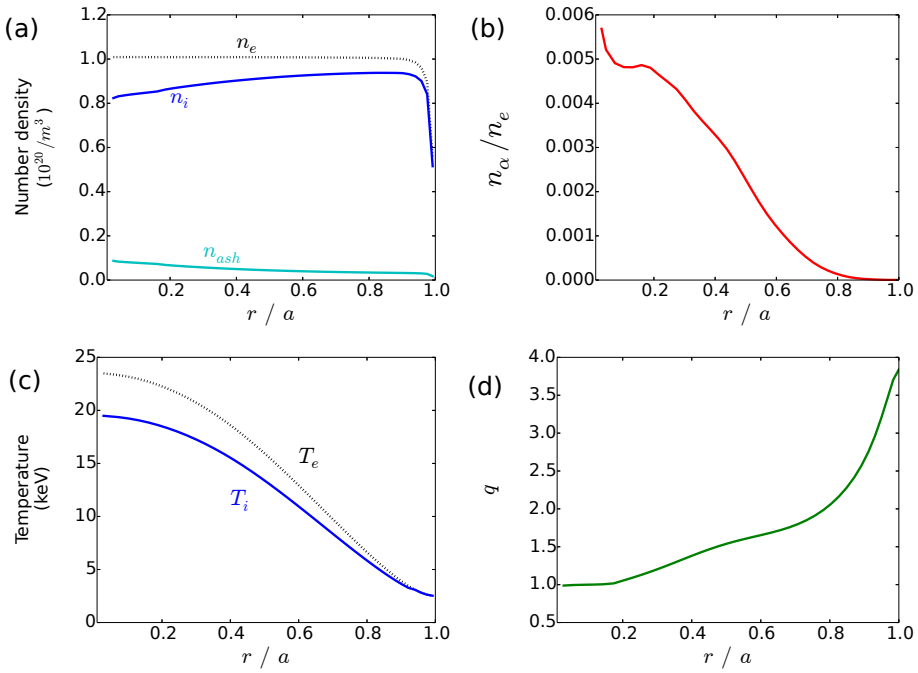

Figure 3.12: Global steady-state profiles for ITER scenario 10010100. For these plots, r is the half-diameter on the plane of the magnetic axis, and serves to label the flux surface. Plots show, as a function of radius, (a) number density of bulk ions, electrons and cold helium ash, (b) relative concentration of alpha particles, (c) temperature, and (d) safety factor q

happens on approximately the same flux surface: that the particle transport time is long compared to the slowing-down time. In this section, we will analyze this assumption using the results from a nonlinear local ITER simulation. Said analysis will be *a posteriori*: assuming a classical slowing-down velocity distribution for fast alpha particles, how likely is it to remain so when taking into account turbulent transport?

3.3.1 Test case

We move from the cyclone base case to a projected ITER ELMy H-mode scenario (case #10010100) from the CCFE 2008 public release database [59, 60],

with radial profiles obtained from`TRANSP` simulations [1]. Figure 3.12 shows radial profiles of some of the equilibrium properties. We use a Miller expansion [61] of the geometry about a flux tube on the surface defined by $r/a = 0.6$, which gives the following geometrical properties: safety factor $q = 1.66$, magnetic shear $\hat{s} = 0.39$, ellipticity $\kappa = 1.53$ (with $a\kappa'(r) = 0.35$), triangularity $\delta = 0.22$ ($a\delta'(r) = 0.41$), and a Shafronov shift derivative of $\Delta'(r) = -0.097$. Electrons are assumed to be adiabatic, with an alpha particle concentration of $n_\alpha/n_e = 0.12\%$, and an ash concentration of $n_{\text{ash}}/n_e = 7.9\%$. The gradient length scales were $a/L_{n_e} = 0.0$, $a/L_{n_i} = -0.37$, $a/L_{n_{\text{ash}}} = 0.95$, $a/L_{n_\alpha} = 6.9$, and $a/L_{T_i} = a/L_{T_{\text{ash}}} = 2.2$. The main ions were taken to be a species with an averaged mass weighted by the density of deuterium, tritium, and a small amount of heavy impurities, resulting in $m_i/m_D = 1.484$, and $Z_i = 1$. The ash is assumed to be at the same temperature as the ions: $T_i = 0.847T_e$, and $T_e = 10.9\,\text{keV}$. The box size is $319\rho_i \times 157\rho_i$ in x and y respectively, with $N_x = 144$ and $N_y = 96$. This large box size is not strictly necessary, but was chosen to ensure that many alpha-particle gyroradii fit inside the simulation domain. The parallel and velocity space resolutions are: $N_\theta = 32$, $N_v = 16$, and $N_\lambda = 33$. The total heat flux resulting from this simulation is shown in figure 3.13 for reference.

3.3.2 Characteristic time scales

We define the alpha particle transport time as a characteristic timescale on which the turbulent particle flux acts. It is found by balancing the appropriate

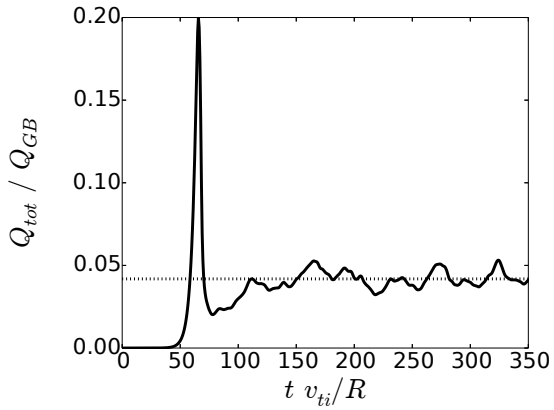

Figure 3.13: The time-evolution of the total heat flux at $r = 0.6a$ for the ELMy H-mode ITER shot 10010100.

terms in the transport equation (2.65):

$$\frac{\partial F_{0\alpha}}{\partial t} + \nabla \cdot \mathbf{\Gamma}(E) \sim \frac{F_{0\alpha}}{\tau_\Gamma} - \frac{\Gamma(E)}{L_{n_\alpha}}, \tag{3.18}$$

where L_{n_α} is chosen as the characteristic length scale on which the alpha particle flux varies. This serves to define:

$$\tau_\Gamma(E) \equiv \frac{L_{n_\alpha} F_{0\alpha}}{\Gamma(E)}. \tag{3.19}$$

We wish to compare this transport time to a timescale representative of the effects of collisions. The energy-diffusion term is given by:

$$C_E\left[F_{0\alpha}\right] = \sum_{s=i,e} \frac{1}{v^2}\frac{\partial}{\partial v}\left(\nu_s^{\alpha s} v^3 F_{0\alpha} + \frac{1}{2}\nu_\parallel^{\alpha s} v^4 \frac{\partial F_{0\alpha}}{\partial v}\right), \tag{3.20}$$

where ν_s and $\nu_\parallel$ are given by equations (1.10) and (1.11). For the slowing-down distribution $\partial F_{S\alpha}/\partial v = -3v^2 F_{S\alpha}/\left(v_c^3 + v^3\right)$, so we will use this to estimate the

derivative in the $\nu_\parallel$ terms in equation (3.20) for a slightly more general $F_{0\alpha}$.

Adding all these terms, we can define a total collision time by:

$$\frac{1}{\tau_c} \sim \frac{1}{F_{0\alpha}} C_E\left[F_{0\alpha}\right] \approx \sum_{s=i,e} \frac{16\pi n_s Z_s^2 e^4 \ln\Lambda_{\alpha s}}{m_\alpha^2}\left[\frac{m_\alpha}{T_s v} - \frac{3}{v_c^3 + v^3}\right] G\left(\frac{v}{v_{ts}}\right). \tag{3.21}$$

Now, by comparing equations (3.19) and (3.21), we can make a reasonable estimate of how relevant a transport term would be in an equation like (2.65). This is shown in figure 3.14. Around $E_\alpha = 3.5\,\mathrm{MeV}$, we see that collisions are dominant over transport, and τ_c flattens out to the slowing-down time τ_s as expected. Also, if τ_Γ is interpreted as a particle confinement time, we expect hot alphas to be well-confined on the order of several seconds. This is roughly consistent with previous work [19]. Our local estimate for the actual alpha particle confinement time (defined as the average number of alpha particles leaving a flux surface divided by the total number of particles contained within the flux surface) is about 2.4 s in our simulation, roughly consistent with the energy confinement time estimated in table 1.1.

However, at lower energies, but still well above the ion or ash temperatures, the radial transport of alpha particles becomes important compared to collisions. For this case, it can be seen in figure 3.14 that the relative importance peaks near the critical speed. There is no reason to believe this is more than coincidence: there are a number of parameters that could, in principle, be independently tuned. For example, the transport time scale scales quadratically with both ρ^* and $L_{n\alpha}$, neither of which would have a direct effect on the characteristic collision time.

Since these simulations were run with adiabatic electrons, kinetic electrons

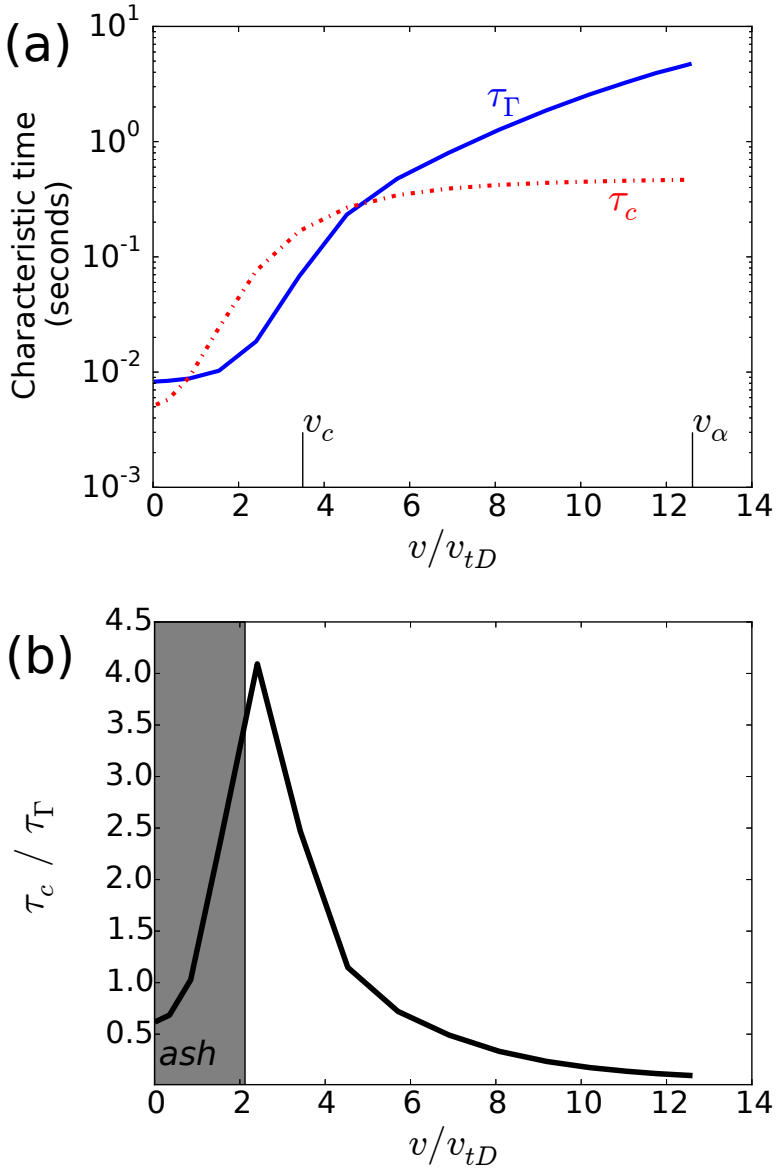

Figure 3.14: Comparing characteristic transport time (τ_Γ) and collision time (τ_c) as a function of speed. (a) shows the characteristic times directly, whereas (b) shows the relative importance of radial transport compared to collisions: τ_c/τ_Γ. The shaded region represents the area up to $v = 3 \times v_{t,\mathrm{ash}}$ (assuming $T_{\mathrm{ash}} = T_i$), where the slowing-down distribution is not valid and is dominated by Maxwellianized helium ash. The critical speed v_c and birth speed v_α have been marked for reference.

would change the numerical value of the flux and thus the ratio of collision time to transport time. However, in our experience, including kinetic electrons generally tends to increase the fluctuation amplitudes, which would increase the alpha particle flux accordingly. Therefore, the analysis presented here is a best-case scenario: more rigorous simulations with kinetic electrons would make any modification to the slowing-down distribution even stronger. In later chapters, electrons are included as a kinetic species in the local gyrokinetic simulations.

This chapter established: a) that the trace limit is well-justified for alpha particles in electrostatic turbulence, b) that the equivalent Maxwellian gives incorrect particle fluxes, and c) that that the form of distribution function could be sensitive to the strength of the turbulence. This motivates the work of the remaining chapters in solving for the coupled radial-energy transport of alpha particles.

Chapter 4: Coupled radius-energy trace transport

The results of the previous chapter suggested that the slowing down distribution (1.20) is insufficient to describe alpha particles in microturbulence. In this section, we briefly outline these difficulties and showcase a novel algorithm to efficiently solve for the microturbulent transport of a trace species.

4.1 Difficulties with current technology

In the previous chapter, we found that not only does a Maxwellian model give incorrect results for the turbulent flux of alpha particles, but the slowing-down distribution does as well. As such, the equilibrium distribution needs to be solved self-consistently with the turbulence, and such a distribution cannot be easily parametrized by quantities such as n_s, T_s, or even v_c.

One solution is to use a global full-f algorithm for gyrokinetics [62, 63] in the first place. While in some ways this is the most straightforward solution, it is far from optimal. There is a separation of scales that provides an efficiency advantage to flux-tube gyrokinetics [64], even for high-energy alpha particles[1]. If the goal is to routinely solve for the turbulent dynamics, it would be wasteful to ignore this

[1] Finite orbit widths in smaller devices notwithstanding. See table 1.1.

efficiency advantage. Running a full-f simulation for a confinement time (which is the scale on which the transport evolves) has only recently been achieved [65]. Multiscale gyrokinetics is fully capable of solving for global transport when local simulations are coupled to transport codes such as `Trinity` [66] and `TGYRO` [67], provided the gyrokinetic ordering $\rho^* \ll 1$ holds [68].

These codes utilize the local flux tube approximation to solve for the turbulent fluxes given an initial equilibrium profile. With these steady-state fluxes, these transport codes self-consistently evolve the equilibrium profile of density, flow, and temperature, and the process is iterated. `Trinity` in particular is well-optimized to limit the number of times the expensive nonlinear simulations need to be run.

However, these transport codes work by parametrizing the equilibrium distribution F_{0s} and solve for the global transport of these parameters. In principle, these tools could be generalized to include collisions at the transport-scale, and evolve each energy coupled together via collisions. A serious difficulty presents itself: instead of needing to evolve the global profile of n_s and T_s, for example, one must solve for an entire grid of F_{0s} according to the energy-dependent transport equation (2.65). This increases the simulation cost by at least an order of magnitude. Since a full transport simulation already costs on the order of 1 million CPU hours, this is an unacceptable computational cost for routine use in the near future. This is particularly frustrating if the dynamics of the troublesome species is well-approximated as only passively responding to the turbulence, such as the case of alpha particles in electrostatic turbulence.

4.2 Trace transport

Since a full multiscale transport simulation is already quite expensive, and full-f simulations are even worse, there is always a market for reduced models for the turbulence, such as gyrofluid [64,69] or analytic approximations. Here, we present a model based on the trace approximation of section 3.1, applicable to alpha particles in electrostatic turbulence.

In the trace approximation, we can write the gyrokinetic equation (2.45) schematically as:

$$\mathcal{L}h_\alpha = -\frac{Z_\alpha e}{m_\alpha v}\frac{\partial \langle\phi\rangle_{\mathbf{R}}}{\partial t}\frac{\partial F_{0\alpha}}{\partial v} - \frac{c}{B}\frac{\partial F_{0\alpha}}{\partial \psi}\mathbf{b}\times\nabla\langle\phi\rangle_{\mathbf{R}}\cdot\nabla\psi, \tag{4.1}$$

where $\mathcal{L}$ is a linear operator that depends on ϕ and all phase space variables, and represents the left-hand side of the gyrokinetic equation, *including the turbulent* $\mathbf{E}\times\mathbf{B}$ *drift term*. It does *not*, however, depend on the equilibrium distribution, whose dependence in the collisionless gyrokinetic equation is given entirely in the right hand side of equation (4.1). Note that we have changed variables from E to v for later convenience, and we will maintain this convention throughout this chapter. Also, we will treat the electrostatic case in this chapter and the next for simplicity, but the general method and the `T3CORE` code itself also works for electromagnetic fluctuations as long as the trace approximation still holds.

By treating $\phi(\mathbf{r},t)$ as given (determined by the dynamics of the other, non-trace species), equation (4.1) is a linear partial differential equation for h_α. It is *not*

linear in the sense of quasilinear theory, where the $\mathbf{E} \times \mathbf{B}$ drift is assumed to be weak, nor does it mean that h_α is proportional to ϕ. But it does mean that h_α is a linear function of $\partial F_{0\alpha}/\partial v$ and $\partial F_{0\alpha}/\partial \psi$:

$$h = -\mathcal{L}^{-1}\left[\frac{Z_\alpha e}{m_\alpha v}\frac{\partial \langle\phi\rangle_{\mathbf{R}}}{\partial t}\right]\frac{\partial F_{0\alpha}}{\partial v} - \mathcal{L}^{-1}\left[\frac{c}{B}\mathbf{b}\times\nabla\langle\phi\rangle_{\mathbf{R}}\cdot\nabla\psi\right]\frac{\partial F_{0s}}{\partial \psi}. \tag{4.2}$$

Here and henceforth, we drop the subscript α on the equilibrium distribution and particle fluxes, taking it as implicit that we are speaking of alpha particles. The technique described in this chapter, however, is more general and can be applied to any trace impurity.

Now, integrate equation (4.2) in a manner prescribed by equation (2.63), factoring out the dependence on F_0 to write the radial flux as:

$$\Gamma_\psi = -D_{\psi\psi}\frac{\partial F_0}{\partial \psi} - D_{\psi v}\frac{\partial F_0}{\partial v}, \tag{4.3}$$

and similarly for the energy flux (2.64):

$$\Gamma_v = -D_{v\psi}\frac{\partial F_0}{\partial \psi} - D_{vv}\frac{\partial F_0}{\partial v}. \tag{4.4}$$

The quantities $D_{\psi\psi}$, $D_{\psi v}$, $D_{v\psi}$, and D_{vv} are the four diffusion coefficients that now determine the dynamics of trace alpha particles, and are themselves general functions of ψ and v. Formally, we can write these coefficients in terms of the

gyrokinetic operator $\mathcal{L}$ as:

$$D_{\psi\psi} = \left\langle \sum_{\sigma_\parallel} \int \mathcal{L}^{-1} \left[\frac{c}{B} \mathbf{b} \times \nabla \langle \phi \rangle_{\mathbf{R}} \cdot \nabla \psi \right] \left(\frac{c}{B} \mathbf{b} \times \nabla \langle \phi \rangle_{\mathbf{R}} \cdot \nabla \psi \right) \mathcal{J}_v \mathrm{d}\lambda \right\rangle_t \tag{4.5}$$

$$D_{\psi v} = \left\langle \sum_{\sigma_\parallel} \int \mathcal{L}^{-1} \left[\frac{\partial \langle \phi \rangle_{\mathbf{R}}}{\partial t} \right] \frac{Ze}{mv} \left(\frac{c}{B} \mathbf{b} \times \nabla \langle \phi \rangle_{\mathbf{R}} \cdot \nabla \psi \right) \mathcal{J}_v \mathrm{d}\lambda \right\rangle_t \tag{4.6}$$

$$D_{v\psi} = \left\langle \sum_{\sigma_\parallel} \int \mathcal{L}^{-1} \left[\frac{c}{B} \mathbf{b} \times \nabla \langle \phi \rangle_{\mathbf{R}} \cdot \nabla \psi \right] \frac{Ze}{mv} \left(\frac{\partial \langle \phi \rangle_{\mathbf{R}}}{\partial t} \right) \mathcal{J}_v \mathrm{d}\lambda \right\rangle_t \tag{4.7}$$

$$D_{vv} = \left\langle \sum_{\sigma_\parallel} \int \mathcal{L}^{-1} \left[\frac{\partial \langle \phi \rangle_{\mathbf{R}}}{\partial t} \right] \frac{Z^2 e^2}{m^2 v^2} \left(\frac{\partial \langle \phi \rangle_{\mathbf{R}}}{\partial t} \right) \mathcal{J}_v \mathrm{d}\lambda \right\rangle_t . \tag{4.8}$$

To obtain these, we plugged equation (4.2) into the definitions for the fluxes in equations (2.63) and (2.64), factoring out the dependence of F_0 according to equations (4.3) and (4.4).

Equations (4.3) and (4.4) are identical to the 2×2 system suggested by reference [41]. Their study, however, was a quasilinear model for alpha particles, whereas our treatment is rigorous for full turbulence. Both models require the trace approximation for equations (4.3) and (4.4) to be rigorously valid.

This is a generalization of the technique used in chapter 3 to correct the turbulent flux for a Maxwellian, and we use the example therein as a proof-of-principle. We are now in a position to use this generality to solve for the global transport of alpha particles.

4.3 The T3CORE code

Combined with the transport equation (2.65), equations (4.3) and (4.4) are sufficient to solve for $F_0(\psi, v)$, provided the diffusion coefficients are known. These must be found from turbulence simulations, or perhaps a reduced model. There are two options on how to proceed rigorously:

1. Save $\phi(\mathbf{r}, t)$ from a turbulence simulation and use this to solve the (linear) gyrokinetic equation, energy-by-energy, for the alpha particles and construct the radial and energy fluxes.

2. Use two or more simulations including a trace species to solve for the diffusion coefficients.

Both techniques have their advantages and disadvantages. The first option involves more code development, but would be more efficient since the trace species need not be included in the nonlinear simulation. In this thesis, we use the second option, taking advantage of additional diagnostics such as the energy-dependent flux (2.63).

Explicitly, assume we have the radial flux for two Maxwellian species (with the same charge Z and mass m) in a gyrokinetic simulation: $\Gamma_{\psi 1}$ and $\Gamma_{\psi 2}$. Each of these species is permitted to have its own density (n_1 and n_2), temperature (T_1 and T_2), and radial gradients thereof, and are described by equilibrium distributions F_{M1} and F_{M2}, all respectively. From equations (4.3) and (4.4), we can then write

$$\Gamma_{\psi 1}/F_{M1} = D_{\psi\psi}\left[\frac{1}{L_{n1}} + \frac{1}{L_{T1}}\left(\frac{mv^2}{2T_1} - \frac{3}{2}\right)\right] + D_{\psi v}\frac{mv}{T_1}, \tag{4.9}$$

and

$$\Gamma_{\psi 2}/F_{M2} = D_{\psi\psi}\left[\frac{1}{L_{n2}} + \frac{1}{L_{T2}}\left(\frac{mv^2}{2T_2} - \frac{3}{2}\right)\right] + D_{\psi v}\frac{mv}{T_2}. \tag{4.10}$$

Note that the diffusion coefficients are the same for both of the species. This is because they respond to the same turbulence and have the same charge and mass, thus the operator $\mathcal{L}$ is the same. We solve for the diffusion coefficients in terms of these two fluxes (which are found from simulation):

$$D_{\psi\psi} = \frac{\frac{T_1}{T_2}\left(\Gamma_{\psi 1}/F_{M1}\right) - \left(\Gamma_{\psi 2}/F_{M2}\right)}{d} \tag{4.11}$$

$$\begin{aligned} D_{\psi v} = -\frac{T_1}{mv}\frac{1}{d} \times \Bigg\{ & \left[\frac{1}{L_{n2}} + \frac{1}{L_{T2}}\left(\frac{mv^2}{2T_2} - \frac{3}{2}\right)\right]\left(\Gamma_{\psi 1}/F_{M1}\right) \\ & - \left[\frac{1}{L_{n1}} + \frac{1}{L_{T1}}\left(\frac{mv^2}{2T_1} - \frac{3}{2}\right)\right]\left(\Gamma_{\psi 2}/F_{M2}\right)\Bigg\}, \end{aligned} \tag{4.12}$$

where

$$d \equiv \left[\frac{1}{L_{n1}} + \frac{1}{L_{T1}}\left(\frac{mv^2}{2T_1} - \frac{3}{2}\right)\right]\frac{T_1}{T_2} - \frac{1}{L_{n2}} - \frac{1}{L_{T2}}\left(\frac{mv^2}{2T_2} - \frac{3}{2}\right). \tag{4.13}$$

Note that this 2×2 system can be singular under certain conditions. One can inoculate against this by choosing the two sample species so that $1/L_{T1} = 1/L_{T2} = 0$. The diffusion coefficients for the energy flux ($D_{v\psi}$ and D_{vv}) are calculated the same

way:

$$D_{v\psi} = \frac{\frac{T_1}{T_2}\left(\Gamma_{v1}/F_{M1}\right) - \left(\Gamma_{v2}/F_{M2}\right)}{d} \tag{4.14}$$

$$\begin{aligned} D_{vv} = -\frac{T_1}{mv}\frac{1}{d} \times \Bigg\{ &\left[\frac{1}{L_{n2}} + \frac{1}{L_{T2}}\left(\frac{mv^2}{2T_2} - \frac{3}{2}\right)\right]\left(\Gamma_{v1}/F_{M1}\right) \\ &- \left[\frac{1}{L_{n1}} + \frac{1}{L_{T1}}\left(\frac{mv^2}{2T_1} - \frac{3}{2}\right)\right]\left(\Gamma_{v2}/F_{M2}\right)\Bigg\}, \end{aligned} \tag{4.15}$$

Now that we have a prescription for finding these four diffusion coefficients, valid for *any* equilibrium distribution, we can use equations (4.3) and (4.4) to find the radial and energy fluxes. Finally, we assemble all terms of the transport equation (2.65) including the collision operator and source to obtain:

$$\begin{aligned} &\frac{\partial F_0}{\partial t} - \frac{1}{\mathcal{V}'}\frac{\partial}{\partial \psi}\left(\mathcal{V}' D_{\psi\psi}\frac{\partial F_0}{\partial \psi} + \mathcal{V}' D_{\psi v}\frac{\partial F_0}{\partial v}\right) - \frac{1}{v^2}\frac{\partial}{\partial v}\left(v^2 D_{v\psi}\frac{\partial F_0}{\partial \psi} + v^2 D_{vv}\frac{\partial F_0}{\partial v}\right) \\ &\quad = S_\alpha + \frac{1}{v^2}\frac{\partial}{\partial v}\left[\left(\sum_s \nu_s^{\alpha s}\right) v^2 F_0 + \frac{1}{2}\left(\sum_s \nu_\parallel^{\alpha s}\right) v^4 \frac{\partial F_0}{\partial v}\right], \end{aligned} \tag{4.16}$$

where we used $\mathcal{J}_v \propto v^2$, the alpha particle source S_α (1.4), and the index s is summed is over the bulk ions and electrons. Equation (4.16) is a linear second-order partial differential equation for $F_{0\alpha}$ in ψ-v space.

The `T3CORE` code, written in the Julia programming language [70], solves equation (4.16) using finite-differences, with the fluxes defined on a staggered grid spanning $\psi_{\min} < \psi < \psi_{\max}$ and $0 < v < v_{\max}$. The boundary conditions are defined as follows:

- $\Gamma_\psi\left(\psi_{\min}, v\right)$ is fixed, with a magnitude given by the internal source of alphas,

and is Maxwellian at the local ion temperature and gradient. In other words, only cool ash enters the domain from the inner core $\psi < \psi_{\min}$.

- $F_0(\psi_{\max}, v)$ fixed to be the analytic slowing-down distribution, plus a population of Maxwellian helium at the local ion temperature to bring the total density to a value input by the user.

- $\Gamma_{v,\text{tot}}(\psi, v = 0) = 0$ for all ψ.

- $F_0(\psi, v_{\max}) = 0$.

The total flux in energy $\Gamma_{v,\text{tot}}$ includes the flux from collisions:

$$\Gamma_{v,\text{tot}} \equiv \Gamma_v + v\nu_s + \frac{1}{2}v^2\nu_{\|}, \tag{4.17}$$

and is included as part of the boundary condition so that no alphas slow down through $v = 0$.

To elaborate upon on the first boundary condition above, we consider the velocity space integral of equation (2.65) (recall that the collision operator conserves density so $\int C[F_0]\, \mathrm{d}^3\mathbf{v} = 0$):

$$\frac{\partial n}{\partial t} + \nabla \cdot \mathbf{\Gamma}_p = S_p. \tag{4.18}$$

So, in steady-state, integrate from the magnetic axis ($\psi = 0$) to $\psi_{\min}$ and apply the

divergence theorem:

$$\int \mathbf{\Gamma}_p \cdot \mathbf{n}\, \mathrm{d}\mathbf{S} = \frac{\Gamma_p A_{\psi_{\min}}}{|\nabla\psi|_{\psi_{\min}}} = \int_0^{\psi_{\min}} S_p \mathcal{V}' d\psi, \tag{4.19}$$

where $A_{\psi_{\min}}$ is the physical area of the $\psi_{\min}$ flux surface and $\Gamma_p = \mathbf{\Gamma}_p \cdot \nabla\psi$. This determines the velocity-integrated particle flux, but we furthermore impose a Maxwellian velocity dependence:

$$\Gamma_{\text{in}}(v) \propto D_{\psi\psi} \left[\frac{1}{L_{ni}} + \frac{1}{L_{Ti}} \left(\frac{mv^2}{2T_i} - \frac{3}{2} \right) \right] e^{-m_\alpha v^2/2T_i} \tag{4.20}$$

This is equivalent to assuming that the core is sufficiently collisional (or alternatively, sufficiently quiescient) so that all alpha particles born inside $\psi_{\min}$ slow-down before entering the computational domain of the code, which they do in a way such that their velocity-dependence mirrors that of the bulk ions.

The recipe for using this algorithm is thus:

1. Determine the radial profiles of density and temperature for the bulk species, and calculate associated fusion cross sections from equation (1.3).

2. Run the `GS2` code with the energy-dependent flux diagnostic turned on, and with two additional Maxwellian species, each with the same mass and charge as alpha particles, and whose velocity grid spans the domain up to $v_{\max}$..

3. Calculate the turbulent diffusion coefficients (4.11) and (4.14) from the `GS2` simulations, and interpolate onto a uniform ψ-v grid.

4. Invert a global matrix representing the finite-difference approximation to the transport equation (4.16) to determine either the steady-state solution, or implicitly advance in time as desired.

For the rest of the thesis, we will consider only steady-state solutions to equation (4.16), so that $\partial F_0/\partial t = 0$. The ψ grid is indexed by $1 \leq i \leq N_\psi$, v is indexed by $1 \leq j \leq N_v$, and both coordinates are discretized on a uniform grid.

Once the diffusion coefficients are known from the turbulence simulations, the problem is a 2D partial differential equation, which we solve by finite differences. For a generic interior grid point (ψ_i, v_j), the finite difference equation is:

$$
\begin{aligned}
& v_j^2 \frac{1}{\Delta\psi}\left(\mathcal{V}'^{i+\frac{1}{2}}\Gamma_\psi^{i+\frac{1}{2},j} - \mathcal{V}'^{i-\frac{1}{2}}\Gamma_\psi^{i-\frac{1}{2},j}\right) + \mathcal{V}_i' \frac{1}{\Delta v}\left(v_{j+\frac{1}{2}}^2 \Gamma_v^{i,j+\frac{1}{2}} - v_{j-\frac{1}{2}}^2 \Gamma_v^{i,j-\frac{1}{2}}\right) \\
& + \mathcal{V}_i' \frac{1}{2\Delta v}\left[\left(\nu_s v^3 F_0\right)^{i,j+1} - \left(\nu_s v^2 F_0\right)^{i,j-1}\right] \\
& + \mathcal{V}_i' \frac{1}{2\Delta v}\left[\left(\nu_\parallel v^4 \frac{\partial F_0}{\partial v}\right)^{i,j+\frac{1}{2}} - \left(\nu_\parallel v^4 \frac{\partial F_0}{\partial v}\right)^{i,j-\frac{1}{2}}\right] = v_j^2 \mathcal{V}_i' S_{i,j}
\end{aligned}
\tag{4.21}
$$

where:

$$\Gamma_{\psi}^{i+\frac{1}{2},j} = -\frac{1}{\Delta\psi}\left[D_{\psi\psi}^{i+\frac{1}{2},j}\left(F_0^{i+1,j}-F_0^{i,j}\right)\right] \tag{4.22}$$
$$-\frac{1}{4\Delta v}\left[D_{\psi v}^{i+\frac{1}{2},j}\left(F_0^{i+1,j+1}-F_0^{i+1,j-1}+F_0^{i,j+1}-F_{0i,j-1}\right)\right]$$
$$\Gamma_{\psi}^{i-\frac{1}{2},j} = -\frac{1}{\Delta\psi}\left[D_{\psi\psi}^{i-\frac{1}{2},j}\left(F_0^{i,j}-F_0^{i-1,j}\right)\right] \tag{4.23}$$
$$-\frac{1}{4\Delta v}\left[D_{\psi v}^{i-\frac{1}{2},j}\left(F_0^{i,j+1}-F_0^{i,j-1}+F_0^{i-1,j+1}-F_0^{i-1,j-1}\right)\right]$$
$$\Gamma_{v}^{i,j+\frac{1}{2}} = -\frac{1}{4\Delta\psi}\left[D_{v\psi}^{i,j+\frac{1}{2}}\left(F_0^{i+1,j+1}-F_0^{i-1,j+1}+F_0^{i+1,j}-F_0^{i-1,j}\right)\right]$$
$$-\frac{1}{\Delta v}\left[D_{vv}^{i,j+\frac{1}{2}}\left(F_0^{i,j+1}-F_0^{i,j}\right)\right] \tag{4.24}$$
$$\Gamma_{v}^{i,j-\frac{1}{2}} = -\frac{1}{4\Delta\psi}\left[D_{v\psi}^{i,j-\frac{1}{2}}\left(F_0^{i+1,j}-F_0^{i-1,j}+F_0^{i+1,j-1}-F_0^{i-1,j-1}\right)\right]$$
$$-\frac{1}{\Delta v}\left[D_{vv}^{i,j-\frac{1}{2}}\left(F_0 i,j-F_0^{i,j-1}\right)\right] \tag{4.25}$$

For the boundary condition at $\psi = \psi_{\min}$, the "left" flux at $\psi^{1/2}$ is replaced with the given quantity

$$\Gamma_{\psi}^{\frac{1}{2},j} = \Gamma_{\text{in}}^{j}, \tag{4.26}$$

and put on the right-hand side as an effective part of the source. The distribution $F_0^{N_\psi,j} = F_{0,edge}^{j}$ is fixed at the outer boundary. At the upper boundary in speed, we have $F_0^{i,N_v+1} = 0$. The zero-flux condition at $v = 0$ means that $\Gamma_{v,tot}^{i,1} = 0$.

Before proceeding, it is useful to characterize equation (4.16). As a two-dimensional linear PDE, its *discriminant* is:

$$\Delta \equiv (D_{\psi v} + D_{v\psi})^2 - 4\left(D_{vv} + \frac{1}{2}v^2\sum_s \nu_{\parallel}^{\alpha s}\right)D_{\psi\psi}. \tag{4.27}$$

If $\Delta < 0$, then equation (4.16) is elliptic, and if $\Delta > 0$, it is hyperbolic. We expect a transport equation of this form to be elliptic, but there is no known reason why this ought to be so *a priori*. Whatever symmetry may exist in quasilinear theory is not obeyed for turbulent transport coefficients [71]. Because of this ambiguity in the sign of Δ, we ought to proceed with caution because mixed-type equations require special handling.

4.4 Validation

The algorithm has been tested using a constructed analytic test case. Fixed forms for F_0 and the diffusion coefficients were chosen, and the source that would satisfy equation (4.16) was calculated. Then the code was run using these diffusion coefficients and source to solve for F_0 numerically, and the error with respect to the constructed analytic distribution was analyzed. For this test, circular geometry is used, in which $\psi \equiv r$, the physical radius, and $\mathcal{V}' = d\mathcal{V}/dr \propto r$. We will be making use of normalizing values a and v_{ref} for the r and v coordinates respectively such that $\hat{r} \equiv r/a$ and $\hat{v} \equiv v/v_{\text{ref}}$ are dimensionless. A reference diffusion coefficient D_{ref} is also chosen.

The chosen analytic forms of the diffusion coefficients are:

$$\begin{aligned} D_{rr} &= D_{\text{ref}} \left(3 - \frac{r}{a}\right) \\ D_{rv} = D_{vr} &= D_{\text{ref}} b \frac{v_{\text{ref}}}{a} e^{-2v/v_{\text{ref}}} \\ D_{vv} &= D_{\text{ref}} \frac{v_{\text{ref}}^2}{a^2} e^{-v/v_{\text{ref}}}, \end{aligned} \tag{4.28}$$

where b is a dimensionless parameter. For these coefficients, the condition that the equation be elliptic is provided by:

$$b < \text{Min}\left(e^{3\hat{v}}\sqrt{3-\hat{r}}\right) = \sqrt{2} \tag{4.29}$$

This condition is in the collisionless limit, which is conservative. If we choose the form of F_0 to be:

$$F_0 = \left(2-\hat{r}^2\right)e^{-\hat{v}^2}, \tag{4.30}$$

then the collision operator vanishes and equation (4.16) is satisfied if the source is given by:

$$\begin{aligned} S_{\text{test}} =& \frac{D_{\text{ref}}}{a^2}e^{-\hat{v}^2}\left[6\left(2-\hat{r}\right)+\hat{v}^{-2}\left(2-\hat{r}^2\right)\left(6-2\hat{v}-4\hat{v}^2\right)e^{-\hat{v}}\right. \\ &\left.+2be^{-2\hat{v}}\hat{r}\left(\frac{2\hat{v}}{\hat{r}^2}-5\hat{v}-2+\frac{2}{\hat{v}}\right)\right] \end{aligned} \tag{4.31}$$

With this analytic solution, along with the boundary conditions it satisfies, we can rigorously test the `T3CORE` code. The comparison of the analytic to numerical solution is given in figures 4.1 and 4.2, while figure 4.3 shows the absolute error throughout the domain. The absolute error was chosen in favor of the relative error because the analytic solution is small but nonzero at $v = v_{\text{max}}$, while the numerical solution is forced to vanish. This fact tends to dominate the relative error near that boundary, but is judged unimportant. Figure 4.4 shows the convergence of maximum absolute error as a function of resolution.

With this data, and similar behavior occurring with several different choices

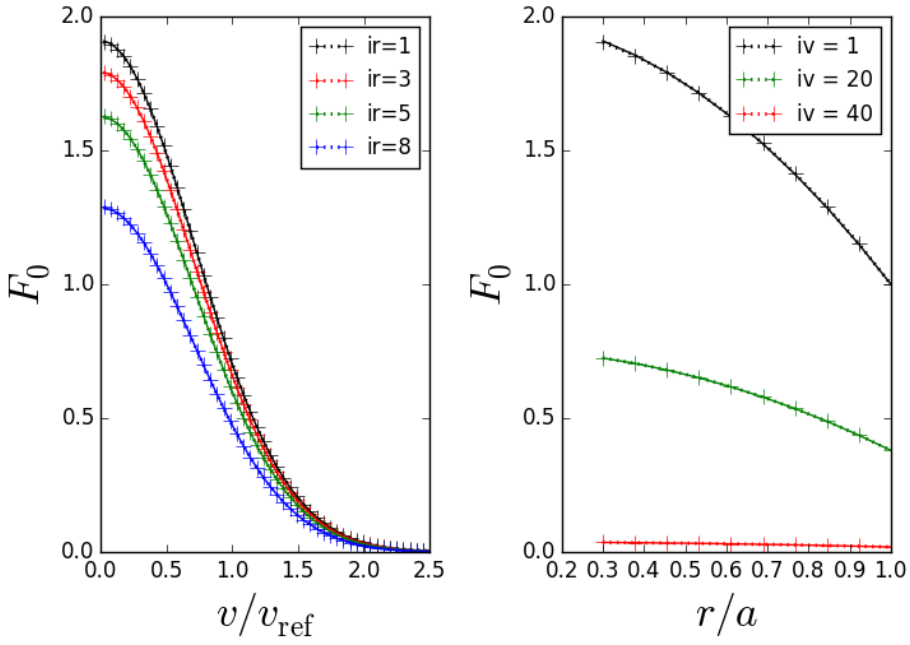

Figure 4.1: Numerical versus analytic solution of F_0 (4.30) at various cross-sections of the domain. The solid lines are the analytic solution, and the dotted lines with crosses of the same color as the corresponding numerical prediction. The resolution is $N_r = 10 \times N_v = 100$, with $b = 0.5$.

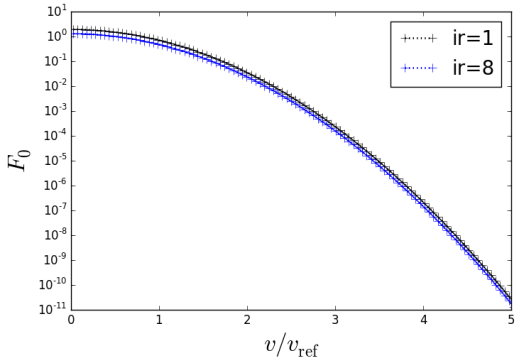

Figure 4.2: Same as the left plot in figure 4.1, but plotted on a logarithmic scale. The good agreement continues through many orders of magnitude.

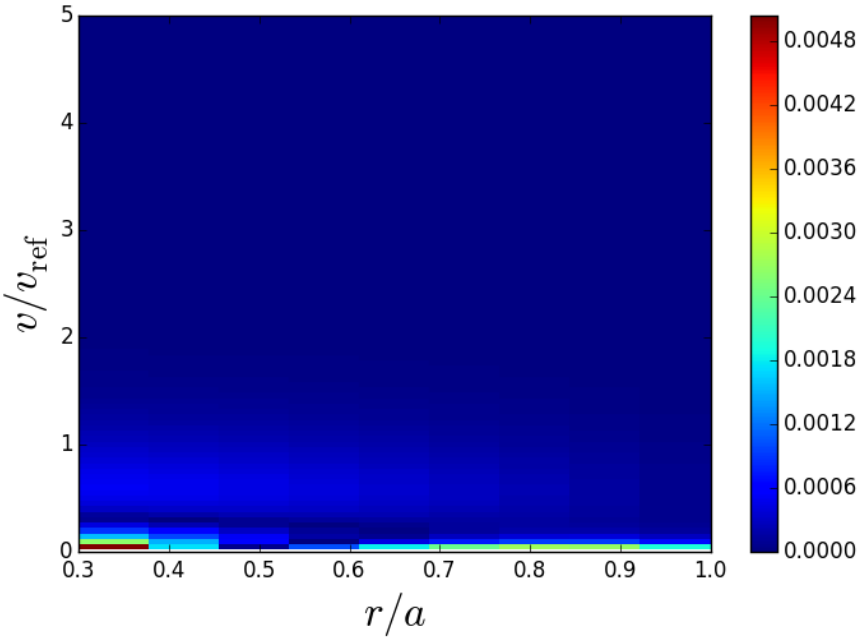

Figure 4.3: A representative example of the absolute errors in `T3CORE` versus the analytic solution (4.30). The resolution is $N_r = 10 \times N_v = 100$, with $v_{\rm max} = 5v_{\rm ref}$, $b = 0.5$, and $D_{\rm ref} = 5$.

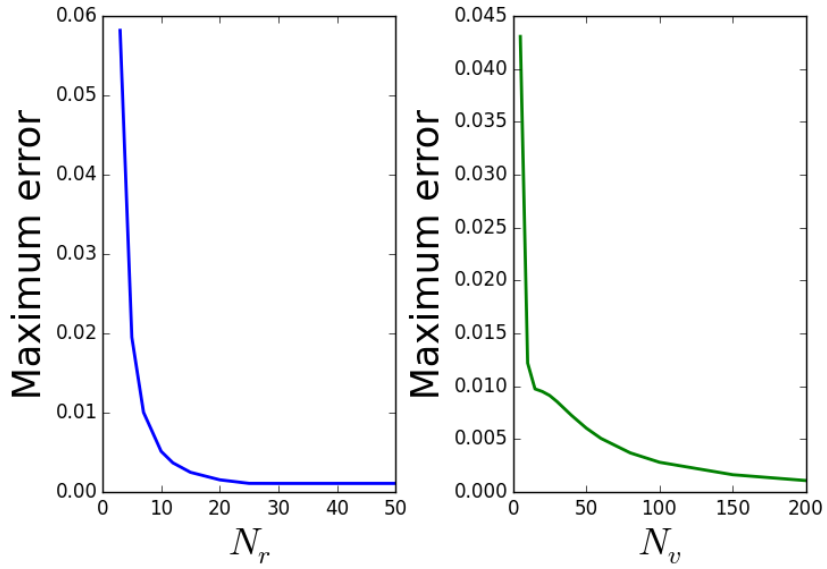

Figure 4.4: The maximum absolute error (which usually occurs at `ir`=`iv`=1, see figure 4.3) as a function of radial resolution at fixed $N_v = 200$ on the left, and velocity resolution at fixed $N_r = 30$ on the right.

of D_{ref} and b, we conclude that the basic `T3CORE` algorithm works well at recreating an arbitrary analytic solution to the transport equation (4.16), and we proceed to apply this tool in the next chapter.

Chapter 5: Effect of turbulence on alpha particles in an ITER-like scenario

The tool described in chapter 4 is generally applicable to any isotropic trace species, with diffusion coefficients provided by turbulence simulations (though, in principle, they could be obtained by any other diffusion model). In this chapter, we apply the `T3CORE` code to the problem of alpha particles in a realistic ITER scenario. We take advantage of the flexibility of the tool to vary several properties of the equilibrium, including the overall fluctuation amplitude profile, magnetic geometry, and the inclusion of a simple dilution model.

5.1 Properties of the background turbulence

We obtain a radial profile from the CCFE public database [59], specifically case 10010100: a typical ELMy H-mode scenario for ITER as run by Budny using `TRANSP` [1]. This is the same case studied in reference [31] and chapter 3. Some bulk equilibrium properties were given in figure 3.12. In this chapter, however, the helium ash is not considered part of the bulk, so the deuterium and tritium densities (taken to be a 50/50 mix) are as radially flat as the electrons. Electrons are a kinetic species in the simulations of this chapter.

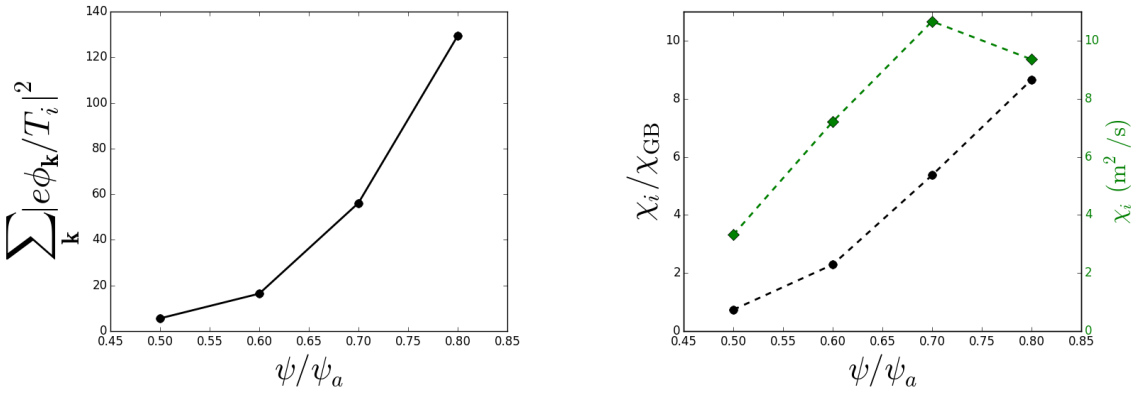

Figure 5.1: On the left is the normalized turbulent electrostatic amplitude from the four `GS2` simulations, and on the right is ion thermal diffusivity defined in equation (5.2). The latter is presented in both normalized (solid black circles) and SI units (dashed green diamonds). The markers represent the discrete values from simulation.

The `GS2` code was run locally at several flux surfaces throughout this profile to obtain energy-dependent fluxes for the two helium species in ITG turbulence, from which we can calculate the diffusion coefficients via equations (4.11) and (4.14). There are four total `GS2` simulations equally spaced between $\psi_{\min} = 0.5\psi_a$ and $\psi_{\max} = 0.8\psi_a$. Beyond this latter radius, direct loss of alpha particles and enhanced ripple transport become important. In this chapter, ψ is taken to be the physical radius of the flux surface: the half-width in meters at the height of the magnetic axis, and ψ_a is the half-width of the last closed flux surface. Unless otherwise stated, all fluctuating quantities including fluxes are steady-state time-averaged.

The general results from these simulations are plotted in figure 5.1. There, the ion thermal diffusivity is determined from:

$$q_i \approx -n_i \chi_i \nabla T_i, \tag{5.1}$$

and we make the usual local approximation that $\nabla T_i \approx -T_i/L_{Ti}$. The normalizing

gyro-Bohm diffusivity [15] is defined as:

$$\chi_{\mathrm{GB}} \equiv \rho_s^2 c_s / a, \tag{5.2}$$

where $c_s = \sqrt{T_e/m_i}$ is the sound speed, and ρ_s is gyroradius calculated at the sound speed. The values we obtain for these ion thermal diffusivities are roughly consistent with previous computational [2, 15] and experimental [72, 73] results. Throughout this chapter, we will use χ_i as a proxy for the amplitude of the turbulence. For example, when we show results having multiplied $\chi_i \times 5$, what is meant is that we have multiplied the square-amplitude of the turbulence (and thus the resulting diffusion coefficients) by the same factor of five.

From these simulations, and interpolating linearly between them and their velocity space grid points, we can obtain trace diffusion coefficients for a helium species in the domain defined by $0.5 < \psi/\psi_a < 0.8$ and $0 < v < v_\alpha$. These are shown in figure 5.2. The nominal case for turbulent transport will be in this domain, with alpha particles being produced in the region $0 < \psi < \psi_{\mathrm{min}}$ entering the domain as a Maxwellian flux at the local ion temperature, and alpha particles being produced within the domain according to equation (1.4). The edge condition of $F_0\left(\psi_{\mathrm{max}}, v\right)$ is the analytic slowing-down distribution (1.20), plus a population of Maxwellian helium at the local ion temperature to bring the total edge[1] density to a given value. Nominally, $10^{17}/\mathrm{m}^3$ (about 0.1% of the local electron density)

[1]This "edge" is not to be confused with the pedestal region or the LCFS. Instead, we are speaking of the outer edge of simulation domain. This is, in a sense, the edge for alpha particles, since beyond here, it is possible for direct orbit losses to become important.

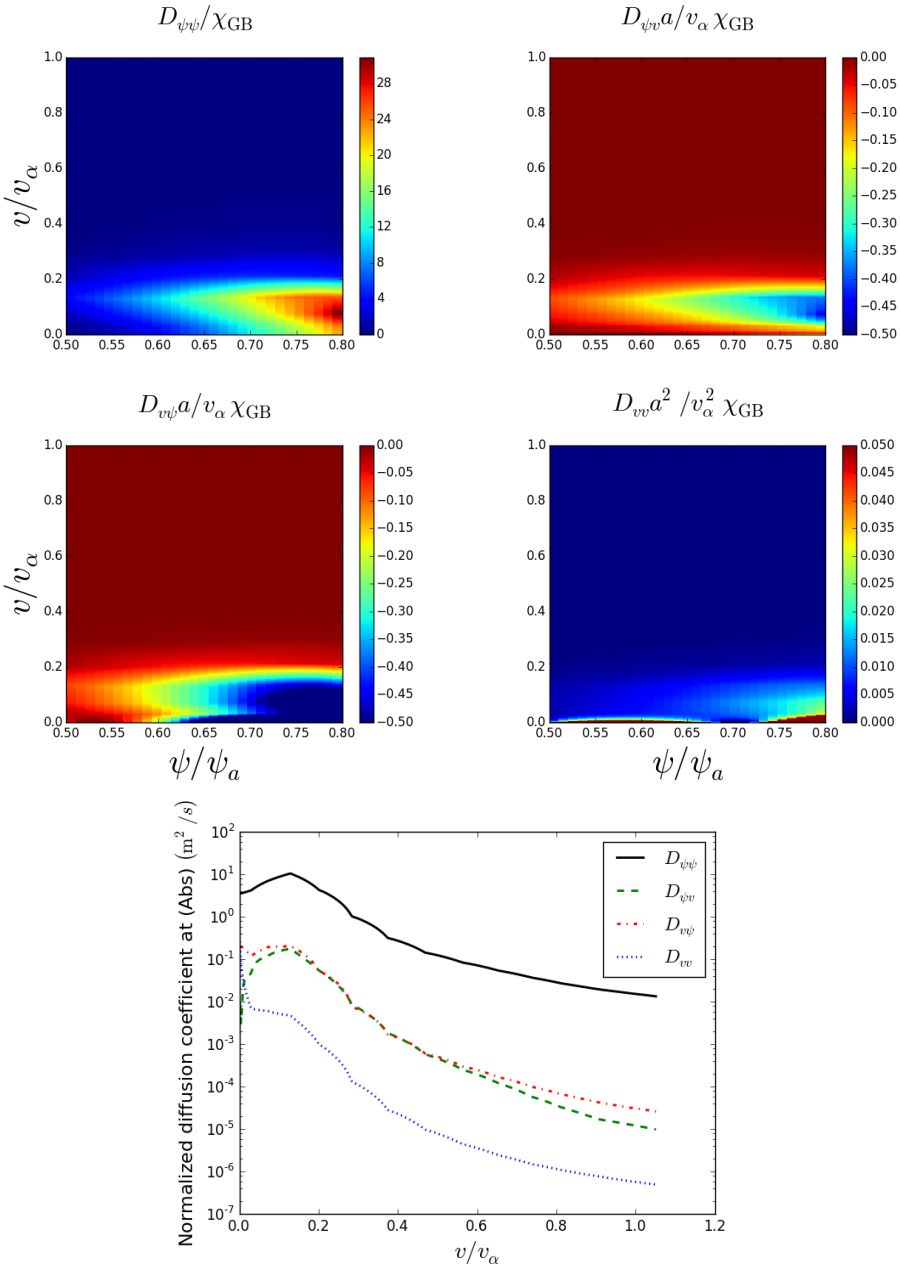

Figure 5.2: At top, the four turbulent diffusion coefficients for a trace helium species in the domain spanned by alpha particles. Numerical values are given with respect to the local (in radius) χ_{GB}. On the bottom is the velocity dependence of the coefficients, also normalized the same values as the top figure, at fixed $\psi = 0.6\psi_a$.

is chosen as the baseline boundary alpha particle density for reasons discussed in section 5.2.3. The baseline resolution is 30 radial grid points in ψ and 400 speed grid points.

Immediately we can make some observations about this case. The dominance of $D_{\psi\psi}$ is apparent in figure 5.2, implying the diffusive models[2] commonly used in the literature are sufficient. This is further confirmed in section 5.3. This need not be the case, but is a statement on the relative phase of h_α and ϕ versus $\partial\phi/\partial t$[3]. Other types of turbulence or species might require more than just radial diffusion. Note that, at high energy, the scaling of all the diffusion coefficients with v is similar. This is because both terms on the right hand side of the gyrokinetic equation (2.45) have the same basic scaling at high energy (from the gyroaverage $\langle\phi\rangle_{\mathbf{R}}$). Also, with these values of diffusion coefficients, combined with the collision frequency $\nu_\parallel$, we can calculate the discriminant from equation (4.27) and find, in this case, that the PDE is elliptic throughout the domain.

With the diffusion coefficients shown in this section, let us examine the behavior of alpha particles applying the low-collisionality transport equation (4.16).

5.2 General properties of the alpha particle distribution

In this section, we describe some of the interesting properties that are observed when solving for the transport of alpha particles. Particularly, we will be looking for departures from the slowing-down distribution.

[2]Note that this does *not* refer only to particle diffusion, but to the diffusion of F_0 as a whole.
[3]See equations 4.5 to 4.8

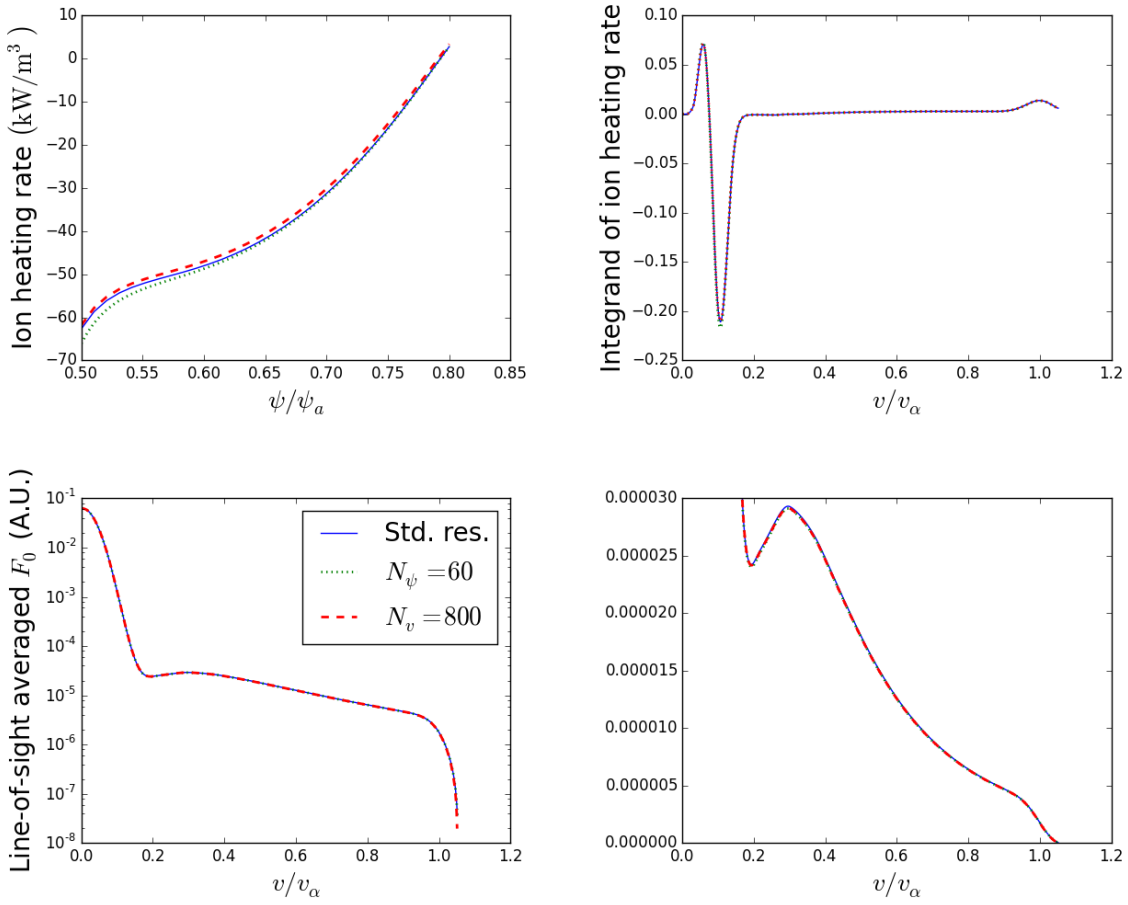

Figure 5.3: Convergence of the solution given by `T3CORE` by comparing sensitive diagnostics. In all cases, we compare the nominal resolution to doubling the energy and radial grid resolutions. On the top left is the alpha-ion heating as a function of radius, and on the top right as a function of energy: the integrand of equation (5.3). The two top plots are with a higher imposed edge density than the nominal case to increase the sensitivity (so that in those plots, $n_{\alpha,\mathrm{edge}} = 10^{18}/\mathrm{m}^3$). The bottom two are the distribution function itself as a function of energy, summed over all radii. The bottom left is a logarithmic scale and the bottom right is a linear scale, focused on the tail.

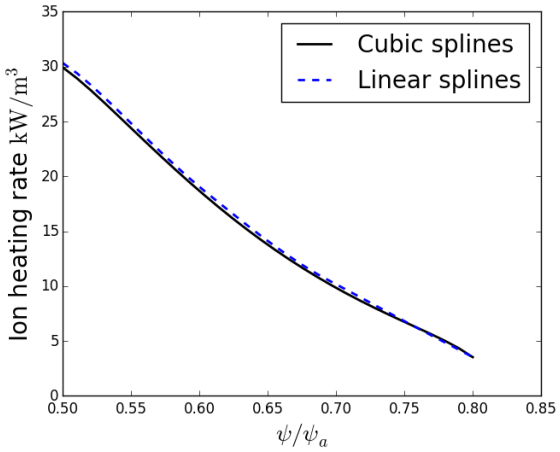

Figure 5.4: Comparing the obtained alpha-ion heating rate as a function of radius for when cubic splines are used between the four `GS2` simulations, versus linear interpolation.

Throughout this section, we will refer to the heating rate *by* alpha particles (either ash or hot alphas) *to* either ions or electrons. To find such a heating rate, we use conservation of energy to express this as the *cooling* rate of alphas against the same species, so that the rate at which alpha particles heat species s via collisions is given by:

$$H_{\alpha s} = -\int C_{\alpha s}\left[F_{0\alpha}\right]\frac{1}{2}m_\alpha v^2\,\mathrm{d}^3\mathbf{v}. \tag{5.3}$$

To gain the reader's confidence in the results presented here, the results of a convergence study are shown in figures 5.3 and 5.4. The latter is used as a proxy to justify that enough `GS2` runs were performed, and that further refinement is not expected to change the results significantly.

5.2.1 Energy distribution and departure from F_s

It is expected from the results of chapter 3 and references [25] and [31] that alpha particles at high energy would be relatively well-confined to a flux surface,

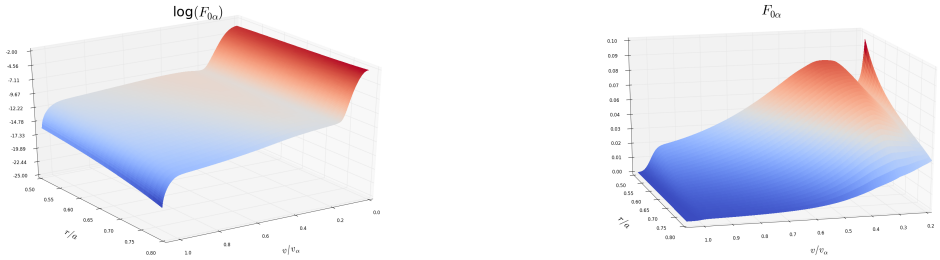

Figure 5.5: On the left: a perspective plot of the logarithm of $F_{0\alpha}$ plotted throughout the domain (excluding the last radial point which is imposed to be the analytic slowing-down distribution). On the right: a linear plot focusing on the tail and the inversion from microturbulence. Units are arbitrary. The beginning of the Maxwellian ash can be seen at the edge of the plotted domain on the right.

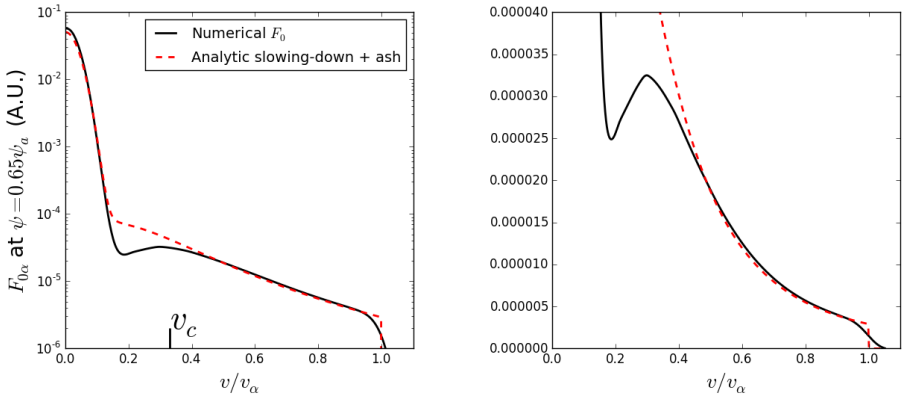

Figure 5.6: The alpha particle distribution compared to the slowing-down distribution at fixed radius $\psi = 0.65\psi_a$. The left plot is on a logarithmic scale, while the right is a linear plot focused on the high-energy tail.

obeying a slowing-down distribution. However, at moderate energies, we expect a significant change to $F_{0\alpha}$, which is reported throughout the domain in figure 5.5, and at particular radii in figures 5.6 and 5.7. There, we compare against the analytic slowing-down distribution for the local source and collisional properties. To match the total density of the calculated distribution, a population of Maxwellian ash was added to the analytic distribution.

At some radii, for the nominal level of turbulence, we observe an inversion in

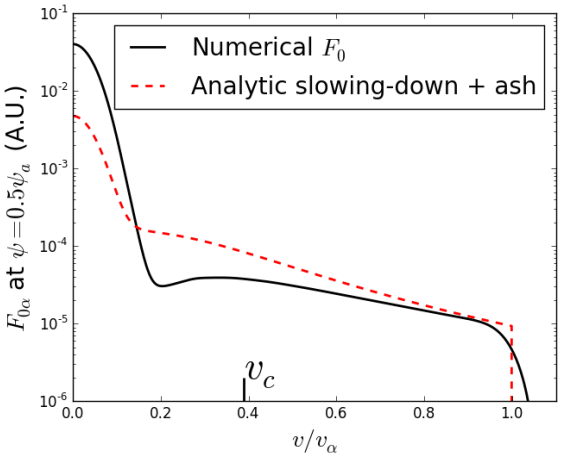

Figure 5.7: The alpha particle distribution compared to the slowing-down distribution at mid-radius $\psi = 0.5\psi_a$. A significant departure from F_s at high energy is observed, compared to the relatively good agreement figure 5.6 (which was taken at another radius). The lack of agreement in the low-energy part is due to our convention of adding only enough ash to keep the total density consistent.

the distribution for a relatively short range of velocity space, roughly between the Maxwellian ash and the critical speed v_c (see figure 5.5). Similar inversions have been observed in experiments and other simulations. For example, reference [3] found a critical diffusion coefficient that, if constant throughout the domain, could cause an inverted distribution. See figure 5.8 for the results of our simulations when the diffusion coefficient is held constant in radius and energy.

Unfortunately, the "realistic" equilibrium profile used in reference [3] is not available, but we can rescale our profile so that the local properties at mid-radius match theirs. Furthermore, other differences include the fact that those authors make the approximation of a Dirac-delta function source, and they approximate the collision operator according to equation (1.16). For these reasons, we do not expect perfect agreement, but we recover the same general trend: a flat or inverted alpha particle distribution when the diffusion coefficient is above a critical value around 6

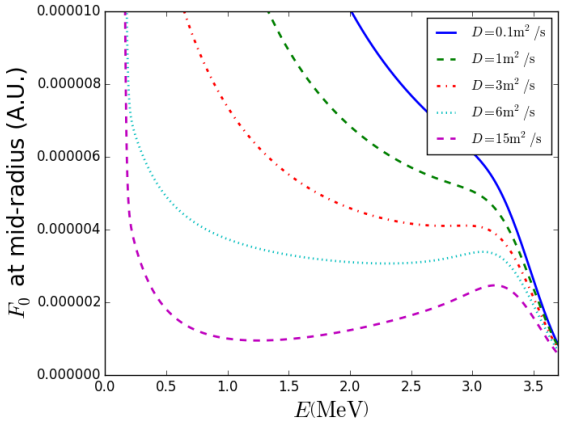

Figure 5.8: Alpha particle distribution at mid-radius for various constant diffusion coefficients. Our radial profile is rescaled so that $n_e = 2 \times 10^{20}/\mathrm{m}^3$ and $T_e = T_i = 10\mathrm{keV}$ at mid-radius. Can be compared to figure 2 of reference [3].

m^2/s.

From our turbulence simulations, we find diffusion coefficients which are strong functions of energy, so we do not expect to see the behavior of figure 5.8 for real simulations. But the diffusion coefficient is appreciable in the lower energy parts of the domain, and this is where we do see the inversion.

The JET experimental team also observed an inversion of the alpha particle distribution, reprinted here in figure 5.9. For our nominal case, we do not see the inversion go to such high energy. Our peak is around 300 to 400 keV, whereas the peak in the JET case is around 1.3 MeV. This difference can be attributed to either different equilibrium parameters (ours is an ITER case), or to Alfvénic activity which is not captured in these electrostatic simulations. Nor is our inversion as strong as seen in figure 5.9, which spans nearly an order of magnitude in $F_{0\alpha}$.

Therefore, we observe energy distributions which can differ significantly from the slowing-down distribution, with unexpected features that are nevertheless sup-

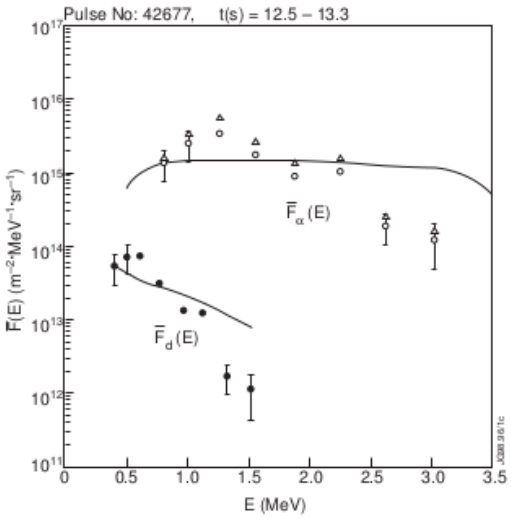

Figure 5.9: Figure 6 from reference [4], reprinted. The hollow and solid dots are measures of line-of-sight integrated distribution function for alpha particles and knock-on deuterons, respectively.

ported by the literature.

5.2.2 Radial profile

Here, we compare some radial properties of the calculated $F_{0\alpha}$ to the analytic slowing down distribution (1.20), which is calculated given only local parameters.

We see from figure 5.10 that the slowing-down distribution differs by at most about 50%. Note that this is purely the analytic slowing-down distribution (1.20) without any ash added. In other sections (*e.g.*, figure 5.6), when we add ash to the slowing-down distribution, we do so in order to keep the total alpha density $n_\alpha = n_{\text{hot}} + n_{\text{ash}}$ consistent. This allows the most generous possible comparison to the analytic slowing-down distribution, allowing for the possibility that somehow one knows the total density of helium.

The heating rate as a function of radius is plotted in figure 5.11. Here we

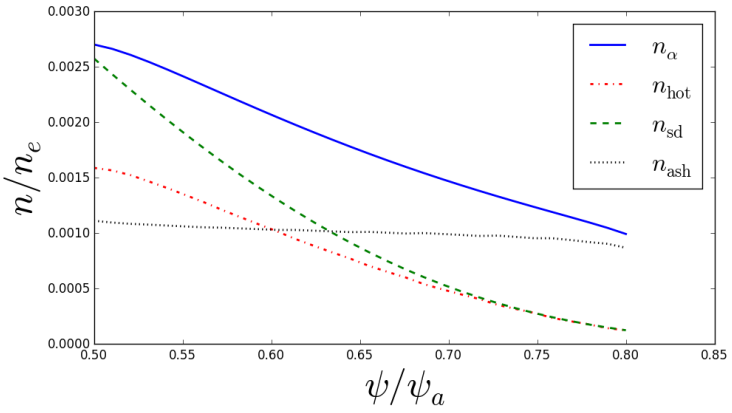

Figure 5.10: The density profile of hot alpha particles as compared to the analytic slowing-down distribution, with an approximately uniform ash for comparison. The solid blue line is the total density of helium from the simulation, and the ash is separated out as described in section 5.2.3.

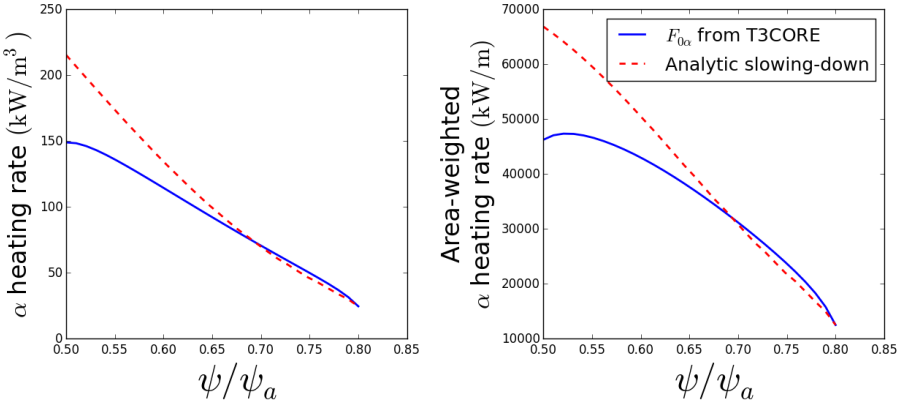

Figure 5.11: On the left is the alpha particle heating rate summed over ions and electrons based on the calculated and slowing-down distributions. On the right is weighted by the area of the flux surface $A_\psi \sum_s H_s$

see differences approximately in line with the density profiles in figure 5.10. At some radii, we see a decrease in the alpha heating compared to the slowing-down distribution, while at others, a small increase.

5.2.3 Effect of the ash

While this dissertation focuses on the non-Maxwellian tail of hot alphas, it is worthwhile to put this into context by examining the transport of the low-energy Maxwellians with energies around T_i. Note that `T3CORE` solves for the entire distribution self-consistently: any Maxwellianization that arises is due to the natural solution of the collision operator (1.15).

We run transport simulations of our base case for several edge densities. To get approximate Maxwellian quantities at low temperature, we perform a linear fit of $\log F_{0\alpha}$ to v^2 using all the grid points between $0 < v < v_{ti}/\sqrt{2}$. The goodness of this fit is illustrated in figure 5.12, and the results from these fits are shown as radial density and temperature profiles for the ash in figure 5.13.

We observe a relatively flat density profile for the ash, which is consistent with previous TFTR [74–76] and DIII-D [77] measurements. This latter study provides further experimental support for our observation that the total amount of helium present in the plasma is mostly a function of the density at the edge.

In some cases, we see a modest decrease in the ash temperature relative to the bulk ions. It is because of this decrease in temperature that the amount of ash present can have a significant effect on the collisional ion heating in the transport

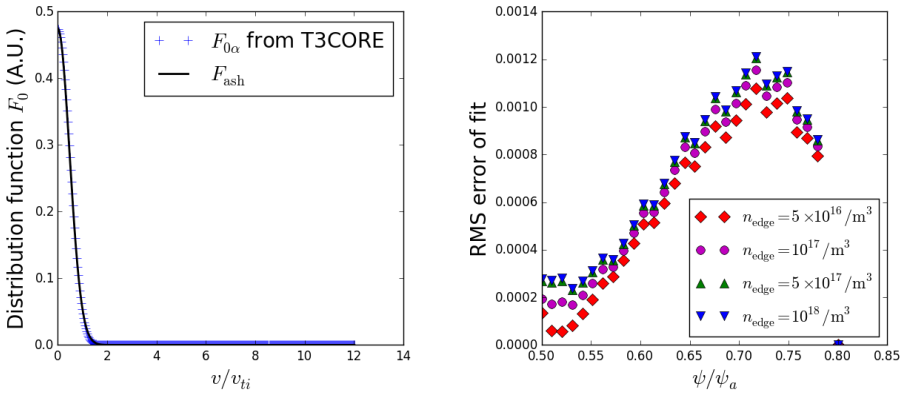

Figure 5.12: On the left, a typical fit of $F_{0\alpha}$ to a Maxwellian (here, $n_{\rm edge} = 10^{18}$ at $\psi = 0.5\psi_a$). On the right: the root-mean-square measure of how good this fit is for several radii and edge conditions.

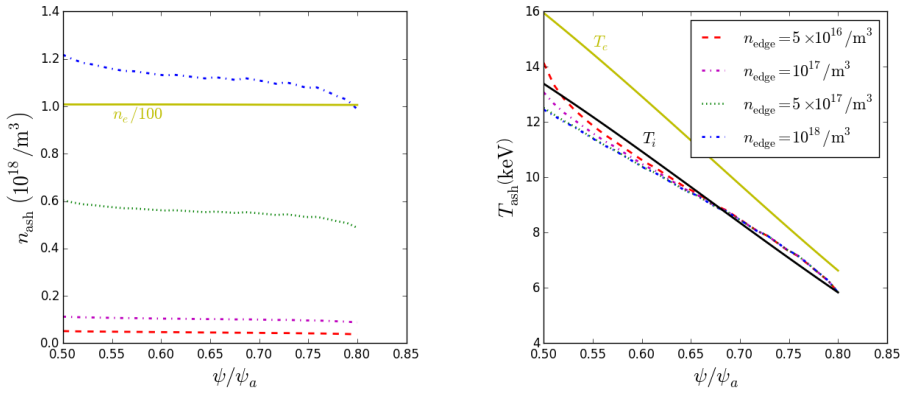

Figure 5.13: On the left and right are respectively the densities and temperatures of the ash compared to the equilibrium, as calculated by a fit to $F_{0\alpha}$. The solid yellow line on the left plot is the equilibrium electron density divided by 100, and the solid yellow and black lines on the right are the electron and ion temperature, respectively.

simulation.

To quantify the effect on heating, see figure 5.14, which is broken down into high- and low-energy alpha contributions, and the effect on ions and electrons. Note that only this latter distinction is physically meaningful: we don't know *a priori* where the ash ends and the hot alphas begin, and the statistical fit is not perfect. For these diagnostic purposes, we define the "hot" alpha particle distribution to be

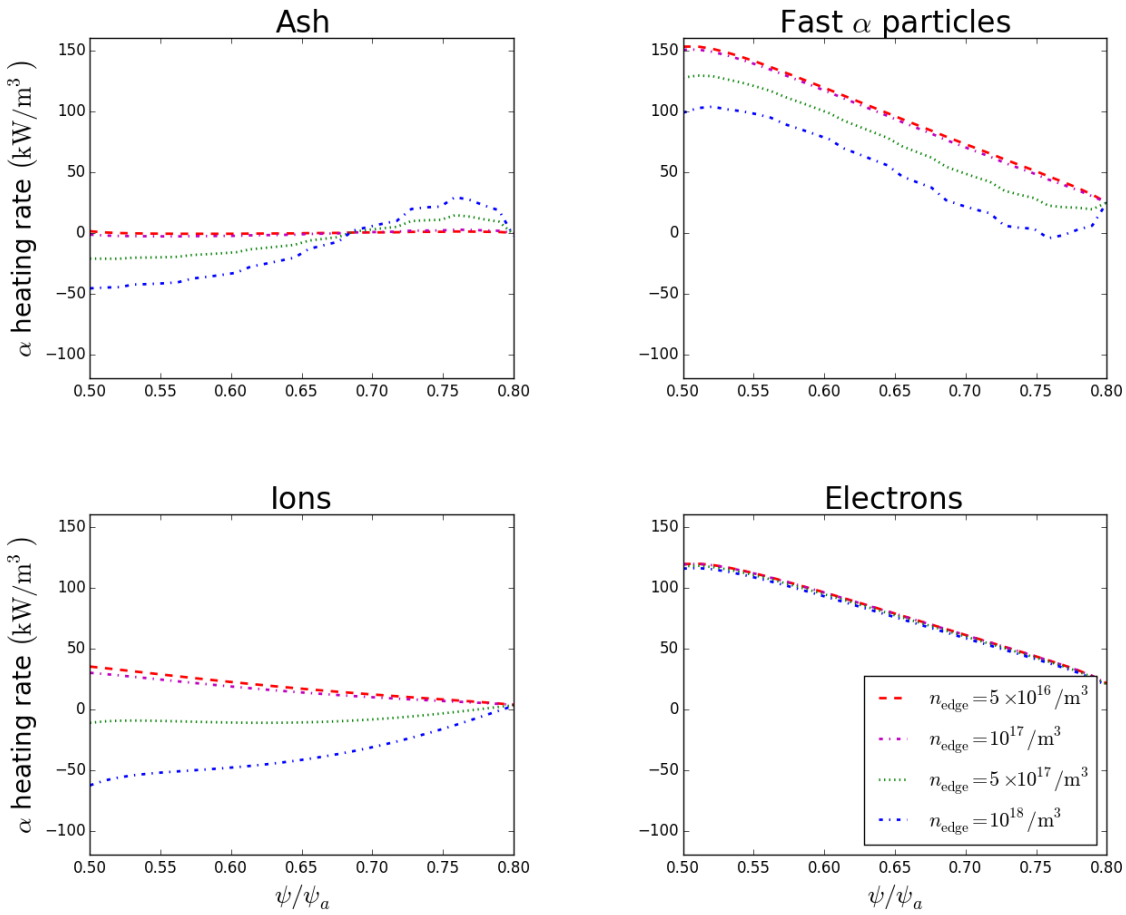

Figure 5.14: The effect of the edge density on collisional alpha heating rate. Top-left: heating rate from the ash to the plasma; top-right: heating rate from the hot distribution ($F_{0\alpha} - F_{\rm ash}$); bottom-left: heating rate to the ions; bottom-right: heating rate to the electrons.

the difference between the full distribution and the fitted ash:

$$F_{\text{hot}} \equiv F_{0\alpha} - F_{\text{ash}}. \tag{5.4}$$

The hot alpha density is then $n_{\text{hot}} = \int F_{\text{hot}}\, \mathrm{d}^3\mathbf{v}$.

We see that the heating of ions is significantly affected by the edge condition, while the electron heating is largely untouched. Both "hot" and "ash" parts of the distribution appear to contribute to the effect of reducing the heating of ions.

Recall that our our diffusion coefficients are interpolated linearly from a `GS2` velocity grid, which neither uses nor requires as fine of an energy grid as `T3CORE`. This could call these results into question (the relative cooling of ions by low-energy alphas). The results of this section are robust to increasing `GS2` velocity resolution. The reason is because the Legendre grid used in `GS2` puts a relatively large number of points at low energy, so the ash is already fairly well resolved, even when a relatively few number of grid points span the entire alpha energy range.

It is still likely that this anomalous cooling of ions is unphysical because the chosen profile is not self-consistent with respect to the turbulence simulations. Perhaps, due to the same turbulence, the ion temperature profile would also change if a `Trinity` simulation were run. In that case, the temperature difference between the ions and helium ash might be minimal. Indeed, experiments [77] show helium transport to scale closely with that of the ions, and this is confirmed by our nonlinear simulations. Therefore, the results of this section can be interpreted as highlighting the limits of the trace approximation, while demonstrating the importance of helium

transport. The *relative* transport of the helium ash compared to the main ions is particularly important.

The results in this section indicate that, if the ash transports unfavorably, it can undo heating benefits of fusion alpha particles, especially to the ions. To accurately calculate the temperature difference ($T_{\text{ash}} - T_i$), a self-consistent turbulent transport simulation of the bulk plasma is required. We proceed with the nominal case with $n_{\text{edge}} = 10^{17}/\text{m}^3$, chosen to minimize this effect of the ash, and examine the transport of the non-Maxwellian tail. This density also agrees roughly with the helium density predicted by Budny [1] at $\psi \approx 0.8\psi_a$.

5.2.4 Partition of heating among the species

An effect which depends strongly on the energy is the preferential heating of electrons versus ions. At high energy, elastic scattering off of the faster, lighter electrons is dominant, while at lower energies, the energy transfer to slower, heavier ions becomes important. The critical speed v_c marks this transition, so the differences in $F_{0\alpha}$ we observe at and below v_c are expected to have a stronger effect on the ions than the electrons. This expectation is confirmed in figure 5.15, where the modified alpha particle distribution has a relatively strong effect on the ion heating.

Figure 5.15 also shows the heating breakdown by energy by plotting the integrand of equation (5.3). The Maxwellian ash resides primarily below $v = 0.2v_\alpha$. Since we only add enough ash to the slowing-down distribution to make the total density consistent, one can observe a significant difference at these low energies due

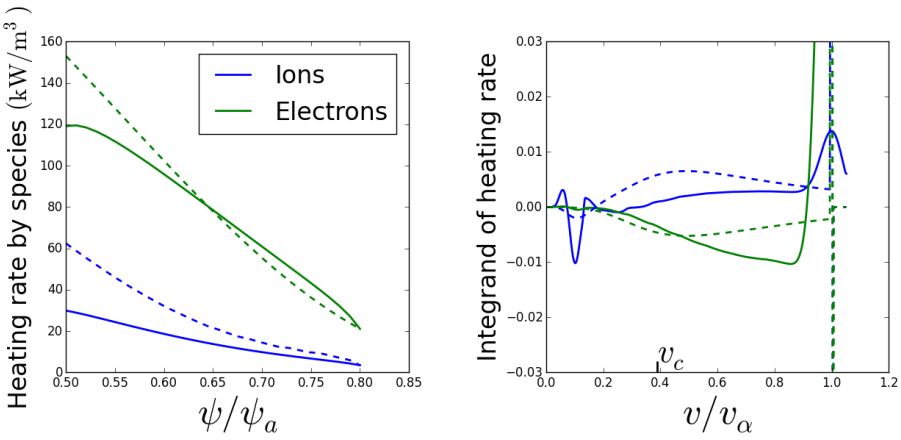

Figure 5.15: On the left: the radial profile of alpha particle heating on electrons and ions. On the right: the collisional heating by alpha particles at $\psi = 0.5\psi_a$, broken down by species and energy: $\left(m_\alpha v^2/2\right) C_{\alpha s}\left[F_{0\alpha}\right] 4\pi v^2$, the integrand of equation (5.3). The dotted lines represent the heating by the slowing-down distribution with ash included.

to these different ash densities. At high energy, the slowing-down distribution has a delta function derivative at $v = v_\alpha$, which integrates to approximately the correct value.

Throughout the intermediate energy range, we see a meaningful difference between the slowing down distribution and the numerically calculated one. As expected, there is a decrease in the ion heating around v_c. Interestingly, we also see an increase in the *cooling* of electrons at moderately high energy ($v \sim 0.8 v_\alpha$). However, this effect is typically dominated by the alpha-electron heating around 3.5 MeV (at a rate which is off the scale of figure 5.15), while the ions do not enjoy such large amounts of heating at that high energy. Therefore, the reduction in heating at moderate energies due to the transport-modified distribution affects the ions disproportionally.

5.3 Effects of turbulence on key alpha diagnostics

In this section, we chronicle the effect of microturbulence on three key alpha particle diagnostics that are related to the primary effects of alpha particles:

1. **Plasma heating**. As discussed in chapter 1 and elaborated upon in this chapter, this is key to achieving burning plasma. It not only depends on the density of alpha particles, but on the particular form of the distribution.

2. **Destabilization of Alfvén eigenmodes**. An important effect of alpha particles is their destabilizing of TAEs, EAEs, etc. These usually depend upon the alpha particle pressure gradient, which will be affected by microturbulence.

3. **Wall and divertor load**. The details of the fast alpha particle trajectories will be important in the edge region in diagnosing how much power will need to be absorbed by plasma-facing components. This region is outside of our simulation domain, but we can provide the alpha particle heat flux entering the pedestal region and beyond.

So the three *key diagnostics* we will refer to throughout this section are: total alpha heating rate; the alpha particle pressure gradient, normalized to the core electron pressure $p_{e0} = n_e\left(\psi = 0\right) \times T_e\left(\psi = 0\right)$; and the alpha particle heat flux. We will be taking into account different scenarios that alter the background microturbulence, or conditions upon the alpha particles themselves, and examining the sensitivity of these diagnostics.

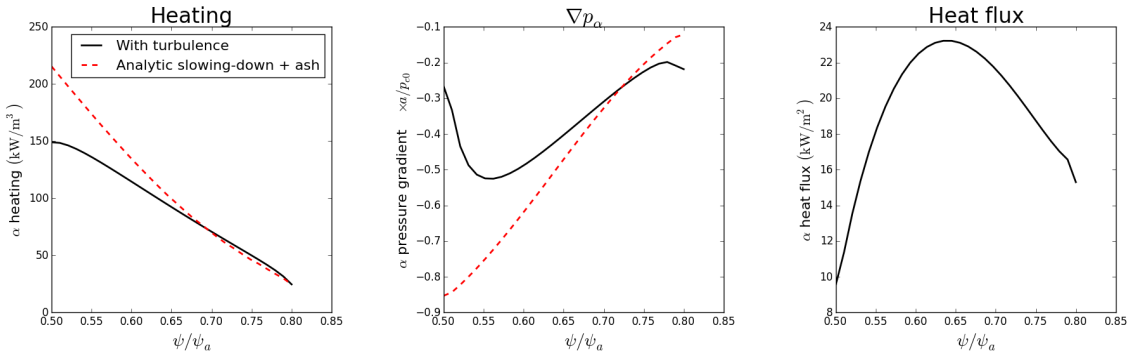

Figure 5.16: Comparing the calculated distribution with microturbulence to that of the local slowing down distribution with a population of ash.

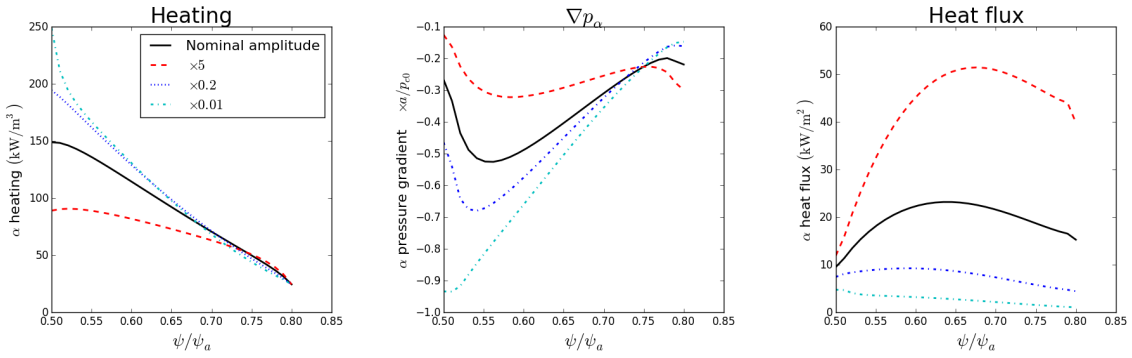

Figure 5.17: Comparing the effect of scaling turbulent amplitude (and hence all diffusion coefficients) by a factor.

First, we reiterate that the presence of microturbulence modifies the slowing-down distribution, which in turn has an effect on the radial profiles in figure 5.16. While we showed in the previous section that there is an effect on the collisional heating rate, particularly for the ions, we find more dramatic effects in the other diagnostics: the alpha pressure gradient nearly halves at $0.55\psi_a$, and there is no way for the slowing-down distribution to generate any heat flux, since it is by definition the stationary (in radius) tail.

Having demonstrated that microturbulence has an effect, we elaborate upon this by scaling the diffusion coefficients by several different factors, and the results of these simulations are in figure 5.17. For this case, increasing the turbulent amplitude

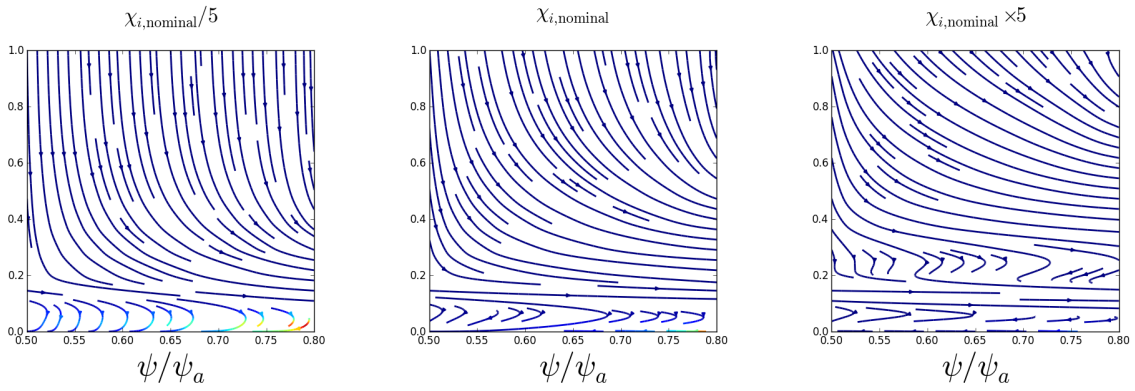

Figure 5.18: Comparing the streamlines of alpha particles under different turbulent conditions. Center is the nominal amplitude, with the left and right scaled up and down by a factor of five, respectively. The slope of the stream lines at every point is the normalized ratio between the energy flux and the radial flux: $\Gamma_{v,\mathrm{tot}}/\Gamma_\psi$.

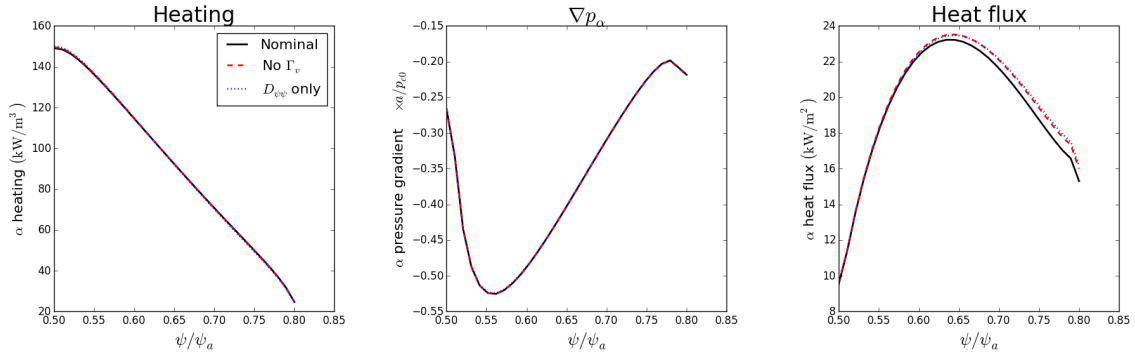

Figure 5.19: Comparing the radial profiles with all four turbulent diffusion coefficients, ignoring energy flux Γ_v, and only retaining the pure radial diffusion coefficient $D_{\psi\psi}$.

by a factor of five has a *decreasing* effect on TAE drive. Also, note the similarity between the very weak turbulence (the cyan curves, with scaling factors of 1/100) and the slowing-down results in figure 5.16, as should be expected. The amplitude of turbulence seems to have a nearly direct relationship with the heat flux into the pedestal. We can visualize the effect of increasing turbulence by comparing the stream-plots in figure 5.18.

While microturbulence plays a significant role in the alpha particle profile, the normalized diffusion coefficients in figure 5.2 imply that radial diffusion is the

dominant mechanism. This is clearly demonstrated in our simulations, examining when various combinations of these four coefficients are implemented. The solid black curves in figure 5.19 are the nominal case with all four diffusion coefficients, the red dashed curves show case where the energy flux is ignored, and for the blue dotted curve, $D_{\psi v}$ is further ignored. This suggests that, at least for ITG turbulence, applying all four diffusion coefficients used here and in reference [41] is unnecessary: only pure radial diffusion plays any significant role.

Note that we are speaking of the radial diffusion of $F_{0\alpha}$, not just density. The diffusion coefficient $D_{\psi\psi}$ contains both the particle and thermal diffusivities as well as the associated cross-terms. Recall that the particle and heat fluxes can be written as moments of the radial flux[4]. Then, what we mean by the diffusive limit is $\Gamma_\psi = -D_{\psi\psi}\partial F_{0\alpha}/\partial\psi$, in contrast to applying equations (4.3) and (4.4), which include all four diffusion coefficients. Any pinch[5] of helium due to microturbulence can come from either: thermodiffusion, which is the part of the particle flux due to a temperature gradient; or the flux-at-zero-gradient, which must come from the $D_{\psi v}$ term in equation (4.3). It is this latter effect that we are asserting is negligible, along with turbulent heating of the alphas, whereas thermodiffusion is contained in the energy dependence of $D_{\psi\psi}$.

One could argue that the other diffusion coefficients become more relevant (though perhaps not dominant) at lower energies by examining figure 5.2. After running with a higher imposed edge density, in figure 5.20, we can see that, even

[4]See equations (2.67) and (2.69)

[5]Defined here as a particle flux against the density gradient

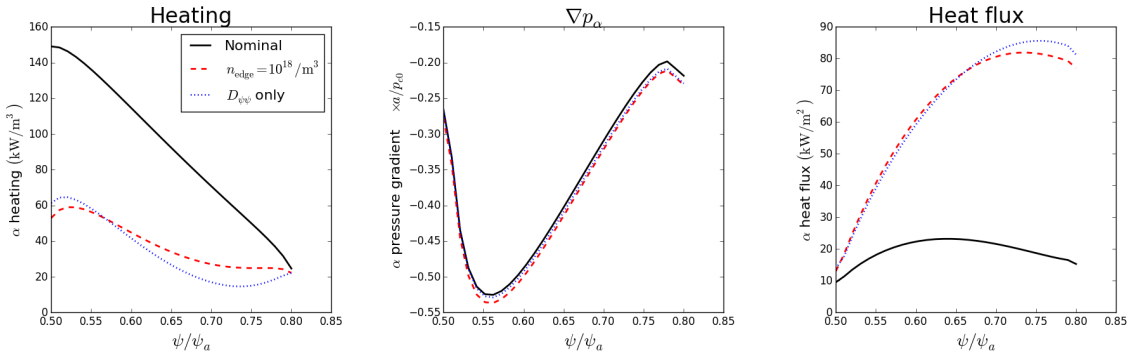

Figure 5.20: Similarly to figure 5.19, compares pure diffusion to all four coefficients, except with a larger ash population.

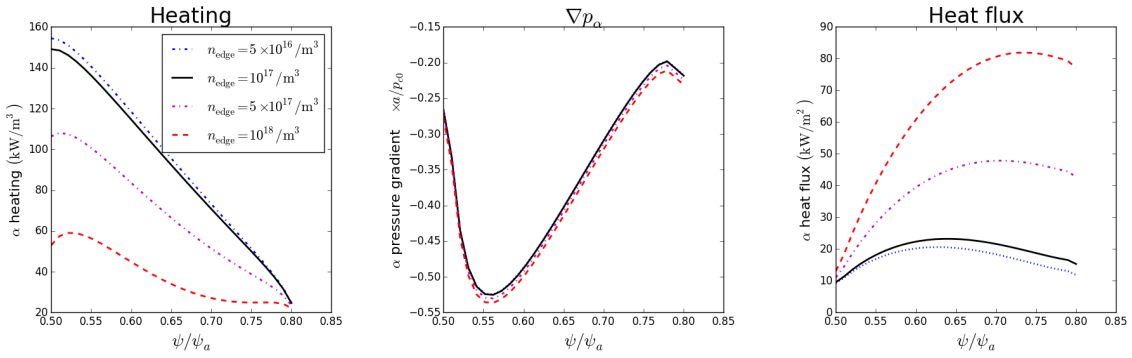

Figure 5.21: Effect of increasing or decreasing the edge density from the nominal case, thereby changing the ash population.

with an increased ash population, there is still little overall effect of $D_{\psi v}$, $D_{v\psi}$, and D_{vv}, except a modest effect in the heating profile.

It has been established in section 5.2.3 that the ash can play an important role in the overall heating, depending on their relative transport with respect to the main ions. In figure 5.21, we include those results alongside the other sensitivity studies in this section.

Finally, we examine the effect that geometry has on our simulation. This manifests itself in the transport algorithm in the difference between $\mathcal{V}'(\psi)$ and surface area A_ψ. In figure 5.22, we plot the alpha particle profile versus a situation where we naively assume a circular geometry. Both cases use the same local Miller [61]

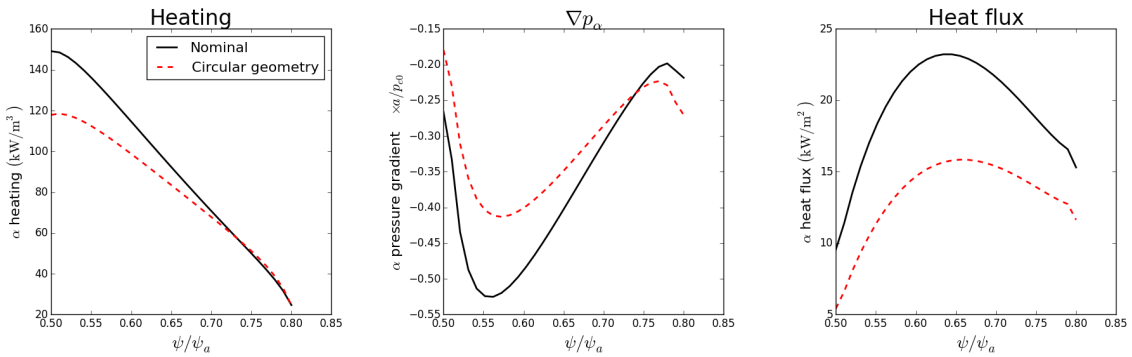

Figure 5.22: Effect of geometry on the alpha particle profile. Circular model has the same surface area as the nominal case. Both cases use the same Miller expansion in `GS2`.

parameters, and the area of each flux surface is held constant. The only difference between the black and the red curves in figure 5.22 is that the latter takes $A_\psi \propto \mathcal{V}'$ in equation (4.16).

5.4 Dilution model

As discussed in chapter 1, one reason why the transport of helium is important is that it dilutes the fusion fuel. With such a flexible tool as `T3CORE`, we can model this effect by iteratively adjusting the source according to the local helium density, assuming the only effect of the helium on the equilibrium is to displace the main ions (holding the electron density constant and keeping the bulk plasma quasi-neutral).

We can go a step further considering the results of section 3.1. There, we determined that, linearly and nonlinearly, even when alpha particles have a high-enough density to not be trace in electrostatic turbulence, their effect is primarily that of diluting the turbulent drive. Both our nonlinear simulations and those of

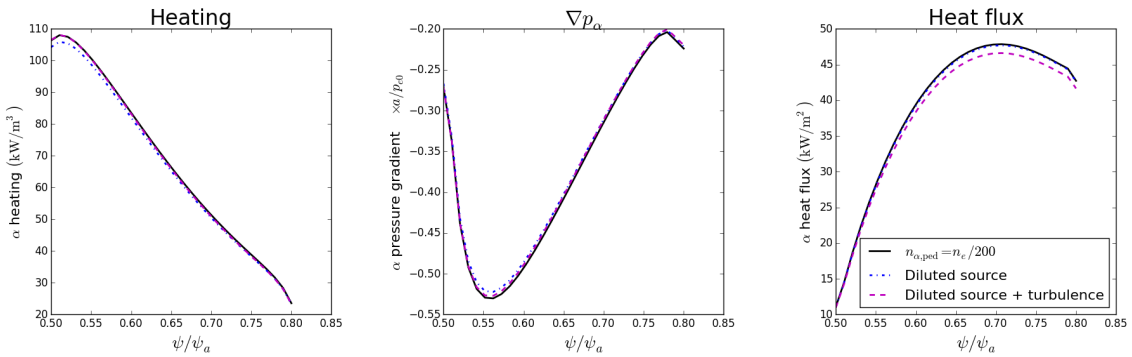

Figure 5.23: Plot of the key diagnostics for the case of $n_{\alpha,\text{edge}} = 0.5\% n_e$, compared to the case where fusion fuel is diluted by the presence of helium, and the case where the turbulence is also diluted.

Tardini [55] are consistent with the following scaling:

$$\frac{\chi_{i,\text{dil}}}{\chi_i} \approx \left(1 - 3\frac{Z_f n_f}{n_e}\right) \tag{5.5}$$

where χ_i is used as a measure of the amplitude of the turbulence and $\chi_{i,\text{dil}}$ is the value of χ_i we would expect if there were a significant population of fast ions of charge Z_f and density n_f. We can apply this to alpha particles in our transport solution to determine the coupled effect of dilution on the source *and* the turbulence. We stress that this is only an *ad hoc* model and make no claims to its general validity. In fact, it was derived for *fast ions*, and if the bulk of the helium is at low density, this dilution scaling may not be valid.

With this caveat in mind, let us proceed to examine the key diagnostics of the previous section taking into account the different forms of dilution and the relative importance of each. We consider helium edge density fractions (relative to electrons) of 0.5%, 1%, and 2% in figures 5.23 to 5.25. We hesitate to go beyond this due to the concerns about the ash concerns raised in section 5.2.3.

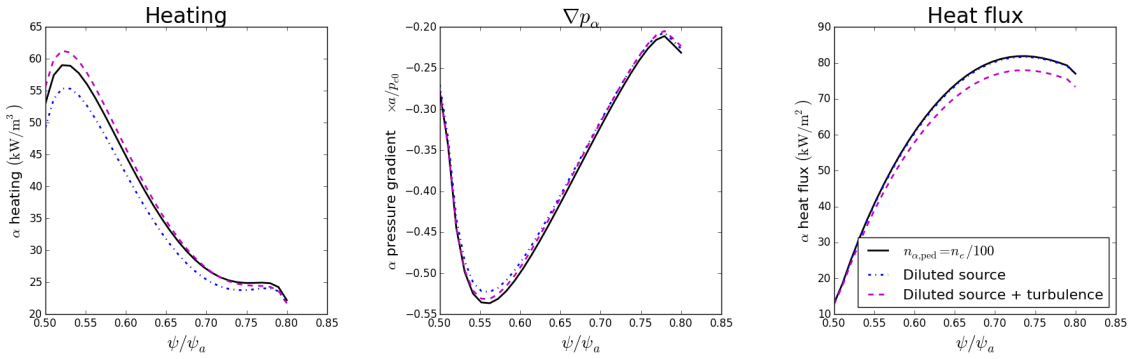

Figure 5.24: Same as figure 5.23, but with $n_{\alpha,\text{edge}} = 1\% n_e$

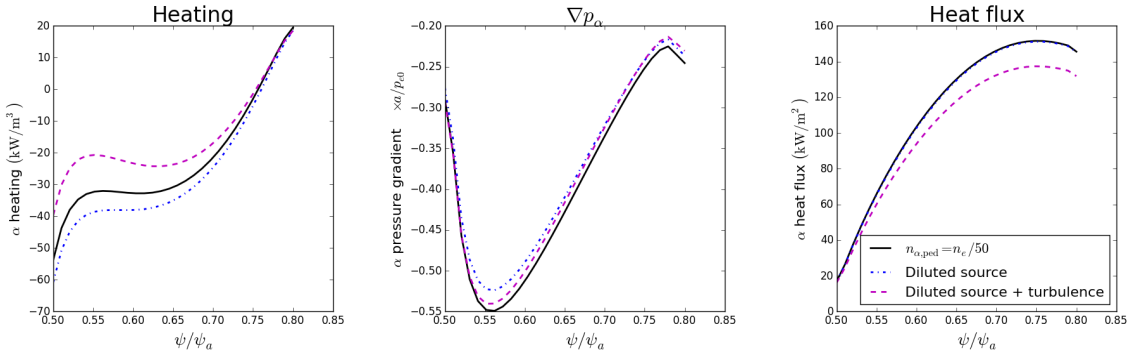

Figure 5.25: Same as figure 5.23, but with $n_{\alpha,\text{edge}} = 2\% n_e$

These results suggest at least the *possibility* that dilution might not be wholly undesirable for fusion. On one hand, the fusion source is reduced by displacing fusing ions with helium. On the other hand, the turbulence is weaker, recovering some alpha-ion heating. Of course, if the turbulence were weaker than in the nominal case here, or if our artificial scaling is not valid, this would change our result. The case where the edge alpha density is 2% in particular started with a *negative* heating rate of ions due to the cooling effect of low-energy alphas on ions (which might be unphysical, see the discussion of section 5.2.3). Neither form of dilution appears to have a significant effect on the pressure profile or heat flux of alphas, at least up to $n_\alpha/n_e \sim 2\%$.

5.5 Core ejection model

Sawteeth are periodic oscillations associated with the kink instability in the central region of a tokamak, named for their characteristic signal in experimental diagnostics [78, 79]. Their effect on fast ions, such as alpha particles, is to eject them from the core [80–82]. While we do not model this central region, nor does `T3CORE` account for MHD timescales, we can simulate the effect of this ejection to some extent by adjusting the inner boundary condition. Instead of a Maxwellian input flux from equation (4.20), let us integrate the source over all radii, keeping the velocity-dependence as-is:

$$\Gamma_{\text{in,ej}}(v) = \frac{|\nabla\psi|_{\psi_{\min}}}{A_{\psi_{\min}}} \int_0^{\psi_{\min}} S_p \mathcal{V}' d\psi. \tag{5.6}$$

This represents a worst-case scenario for sawteeth in two ways: a) this is a steady-state boundary condition, whereas sawteeth are transient phenomena, periodically ejecting fast ions over a period of about 100 ms, and b) here there is *no* collisional slowing-down anywhere between $0 < \psi < 0.5\psi_a$.

That said, let us proceed to analyze the effect of such a steady-state direct ejection of alpha particles. The general behavior of alpha particles is shown in the stream plot in figure 5.26. There is clearly a qualitative difference associated with this high-energy boundary condition at $\psi = 0.5\psi_a$, as compared to figure 1.4. The effect of this steady-state ejection on the key diagnostics is shown in figure 5.27.

As should be expected, this boundary condition results in dramatically differ-

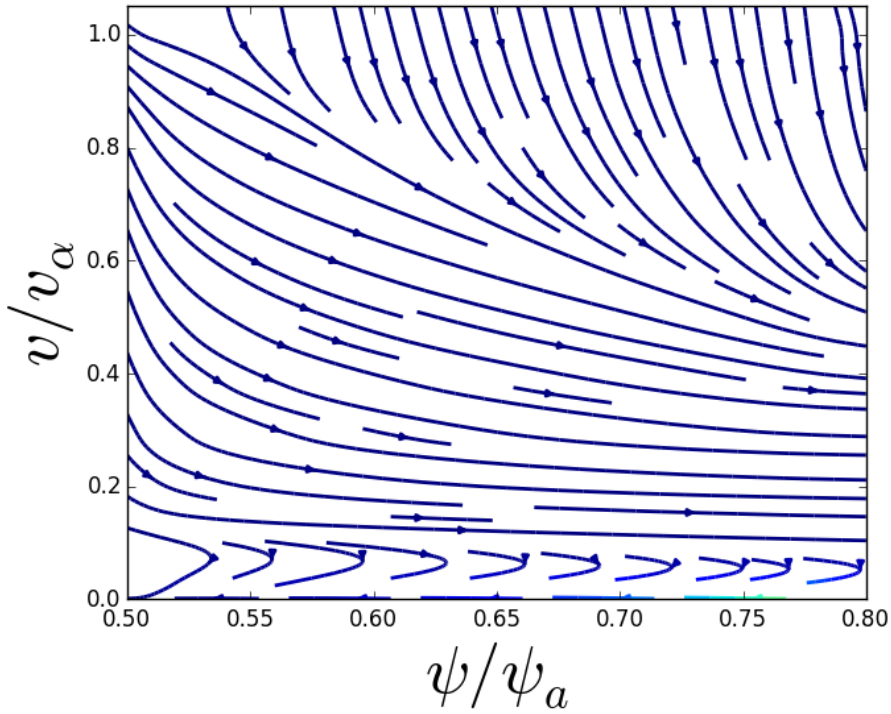

Figure 5.26: Stream plot for the adjusted direct-ejection high-energy boundary condition in equation (5.6). Compare to figure 1.4, where the incoming flux at $\psi = 0.5\psi_a$ is at low energy only.

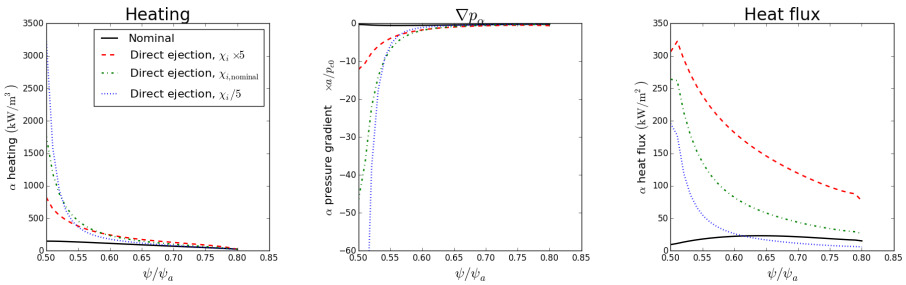

Figure 5.27: Showing key alpha diagnostics for the steady-state high-energy ejection model, with different scalings for the turbulent amplitude.

ent alpha particle profiles. Interestingly, collisions are strong enough to slow down alpha particles in this domain to the extent that the outgoing heat flux at the "edge" is only about twice that as the nominal incoming flux. Naturally, the presence of turbulence (and how strong it is) significantly modifies this edge heat flux, as in figure 5.17. Since alpha particles are entering the domain with much more energy than before, there is a very strong effect on the pressure profile, which is further affected by microturbulence.

Chapter 6: Conclusion and outlook

In this dissertation, we explored in depth the effect of drift wave electrostatic turbulence on fusion-produced alpha particles. Even though finite-beta physics is expected to play an important role in alpha particle transport, it was demonstrated that *even in* electrostatic turbulence, the alpha particle distribution departs from the well-known slowing-down distribution, resulting in many interesting effects which were chronicled. It is suspected that yet more interesting results have yet to be discovered.

Based on our results, if the profiles we have started from are to be trusted as generating a reasonable representation of the turbulence expected in ITER, we can make the following conclusions:

1. Turbulence, and the details thereof, has a significant effect on the alpha particle energy distribution.

2. Increasing the amplitude of turbulence has the effect of modifying the alpha pressure profile favorably with respect to TAE drive, while decreasing the collisional alpha heating power.

3. For electrostatic ITG turbulence, the effect of turbulence is almost entirely

radial diffusion of the distribution function, with a diffusion coefficient that is a strong function of energy.

In order to perform these studies, a code needed to be developed as proof-of-principle and to generate physics results. This tool was specifically developed to post-process `GS2` output files to solve the coupled radial-energy transport of trace alpha particles, with or without finite-beta effects modifying the turbulence. It is not a robust, general-purpose transport solver like `Trinity`, nor does it aim to be. That said, there is always room for improvement of the model, and possible future upgrades include: the inclusion of a collision operator in the fluctuations, which can have a far more complicated dependence on the equilibrium F_{0s} than the other terms in the gyrokinetic equation; and generalizing to include pitch-angle dependence of anisotropic equilibrium distributions.

The novel and efficient technique outlined in this thesis, however, is generally applicable. It is envisioned that `T3CORE` or something like it will mature into a more general-purpose module capable of interfacing between any transport simulator such as `Trinity`, `TRANSP`, `TGYRO`, and `CRONOS`, and to interpret the results of any turbulence simulation. This flexibility, it is hoped, could make way for fruitful collaborations to perform robust, efficient, and reasonably rigorous modelling of non-Maxwellian impurities for ITER and beyond.

Appendix A: Non-Maxwellian effects on TAEs

It sometimes comes as a surprise that a local flux-tube code such as `GS2` is capable of examining TAEs. Cheng, Gorelenkov, and Hsu [83] developed the analytic theory of TAEs in the high-mode-number limit, based on local gyrokinetics with a model for trapped electrons. In addition, Bass and Waltz [6] have used similar a similar code `GYRO` to study TAEs. In this appendix, we chronicle some results from linear `GS2` simulations with non-Maxwellian fast ions.

A.1 Identification of TAEs

Toroidicity-induced Alfvén eigenmodes are stable MHD waves present in toroidal plasmas [5]. It was later discovered that fast particles can destabilize these waves [9], and they have been heavily studied ever since. There are several other Alfvén eigenmodes which are driven unstable under various conditions and take different physics under consideration, such as EAEs, KTAEs, EPMs, etc. In this appendix, we use the term TAE as a shorthand umbrella term for all such Alfvénic modes that are driven unstable by fast ions.

TAEs are characterized by a toroidal mode number n, and those which are unstable in present day devices are typically of order unity. But in larger devices

like ITER, the unstable mode numbers are expected to be around 20-30 [84], making the large-n expansion of reference [83] more appropriate. This also makes TAEs approachable with local flux tube codes. To see why, consider the formal definition of k_y in `GS2` coordinates [85]:

$$k_y \equiv \frac{n}{a} B_a a^2 \frac{d\psi}{d\psi_p}, \tag{A.1}$$

where ψ is a generalized dimensional radial coordinate, ψ_p is the poloidal magnetic flux, and B_a is the magnitude of the magnetic flux at the center point of the LCFS. If we happen to choose the toroidal magnetic flux as our coordinate, then $\psi = a\psi_t / B_a a^2$. Also, normalize k_y by the ion Larmor radius ρ_i so equation (A.2) can be rewritten as:

$$k_y \rho_i = nq\rho^*, \tag{A.2}$$

where we also used the definition of the safety factor $q \equiv d\psi_t / d\psi_p$. We can see that, in order for this to be of order unity with ρ^* small, n must be comparably large. Suppose we have a mode locally unstable at $k_y \rho_i = 0.05$ and $q = 2$. In an ITER-sized device where $\rho^* \approx 10^{-3}$, this would correspond to a toroidal mode number of $n \approx 25$. So while the flux tube does not know what the toroidal mode number is, it does know its wavelength in terms of ρ_i.

Since `GS2` is run as a initial-value code, only the most unstable mode can be studied. Therefore, in recreating the TAEs of reference [5], we must add in a fast-particle species to destabilize it and make it "visible". This changes the properties

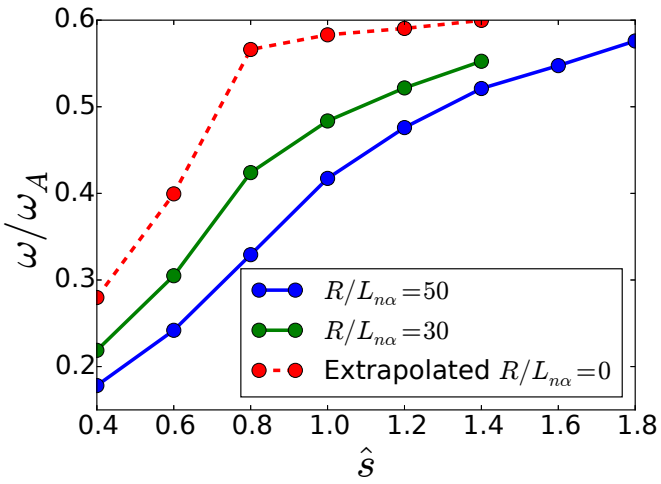

Figure A.1: TAE frequency as a function of shear from `GS2` for inverse aspect ratio $2r/R = 0.2$, to be compared with figure 2 of reference [5]. The normalizing frequency is defined to be $\omega_A = v_A/qR$, where v_A is the Alfvén speed.

of the waves somewhat, but we can extrapolate to the case of stable TAEs in figure A.1. The eigenfunctions produced by such a mode are shown in figure A.2 and compare favorably to reference [5].

A.2 Effect of non-Maxwellian fast ions

We switch to the parameters of Bass and Waltz [6], in which TAEs and EPMs are driven unstable by a population of alpha-particle-like Maxwellian fast ions with $T_f = 100T_e$ and $n_f = 0.025n_e$. Here, we follow their case as closely as possible, including taking $\beta'(\psi) = 0$ for the geometry (so that flux surfaces are concentric and circular).

In figure A.3, we plot the frequency and growth rates for TAEs obtained from our `GS2` simulations. When renormalizing into their units, we see very good agreement with reference [6], except that we do not capture their decrease in growth

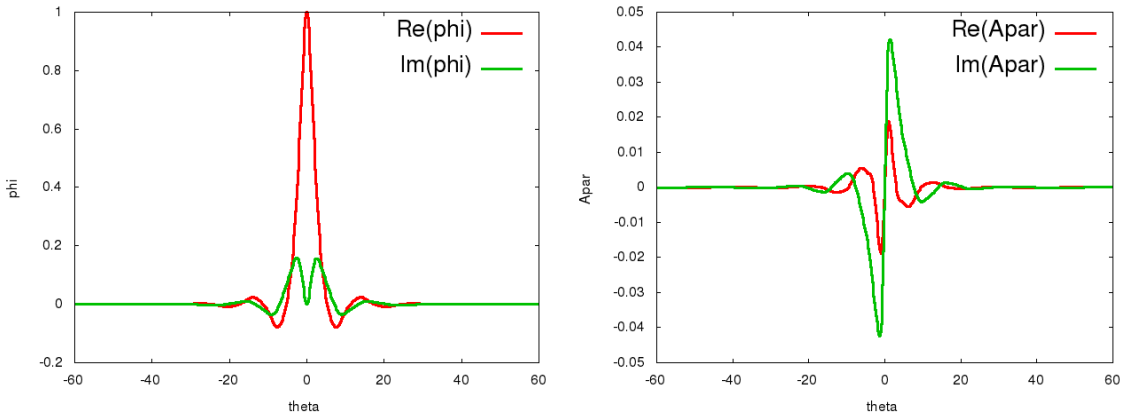

Figure A.2: The TAE eigenfunction generated by `GS2` for a driven version of the case from reference [5]. On the left is the real and imaginary parts of ϕ as a function of θ, to be compared with figure 11 of reference [5]. On the right is $A_{\parallel}$.

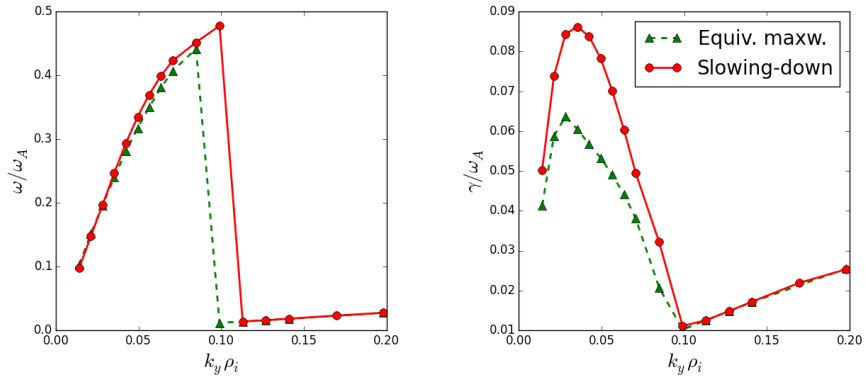

Figure A.3: Frequency (left) and growth rate (right) spectra of the case from reference [6], comparing the equivalent Maxwellian with the slowing-down distribution at $a/L_{nf} = 4$.

rate at $k_\theta\rho_s = 0.03$ in the transition from EPM to TAE. The right side of the plots in figure A.3 is the long-wavelength part of the ITG spectrum.

Also plotted in figure A.3 is the spectrum obtained when the Maxwellian fast ions are replaced with an analytic slowing-down distribution with the same temperature and $v_c \approx 0.4v_\alpha$. We find that this occurs when $E_\alpha \approx 380T_e$, corresponding to a $T_e = 9.2\,\mathrm{keV}$ plasma. In figure A.4, we compare the frequencies and growth rates at different fast ion density gradients for a fixed mode $k_y\rho_i \approx 0.35$.

We conclude that the equivalent Maxwellian fails to reproduce the spectrum

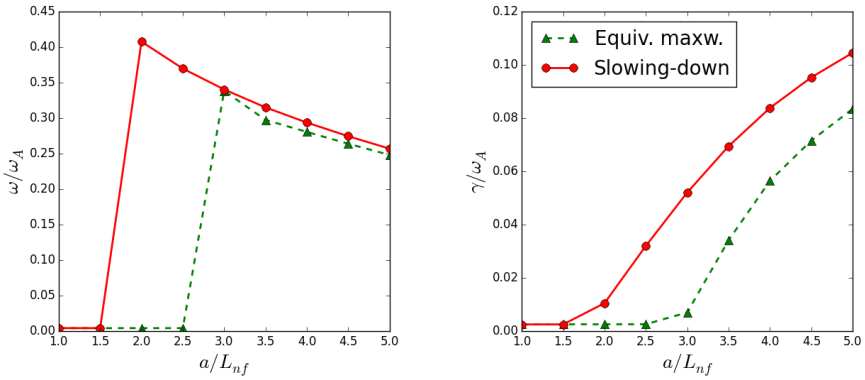

Figure A.4: Frequency (left) and growth rates (right) as a function of fast ion density gradient, comparing the equivalent Maxwellian with the slowing-down distribution.

and critical gradient for TAEs[1] that a slowing-down distribution would predict. This is unsurprising: if a wave is driven unstable by resonant particles, the shape of the distribution function F_0 would certainly matter.

[1]Note that the authors of reference [6] later refer to the critical gradient for TAEs in their stiff transport model [14]. In this context, it is believed that they are referring to the alpha particle gradient *at which TAEs fail to saturate* in nonlinear simulations. We make no claims as to whether or not Maxwellian and slowing-down alphas behave similarly in this regard.

Appendix B: Numerical instability in the δf-PIC algorithm

In this appendix, we examine the δf particle-in-cell algorithm from an analytic, applied-mathematics perspective. In doing so, we find an unconditional numerical instability that has been observed in codes based on this algorithm. We outline several efforts to seek a fundamental cause of the instability, with limited success.

Particle-in-cell (PIC) methods have been a widely used tool in plasma physics for decades. In classic "full-f" Vlasov PIC, charged particles are simulated and the fields are approximated on a grid based on an appropriate interpolant. All particles of the same species are identical: the concentration of simulation particles represents the value of the distribution function at a particular location in phase space, just as it is physically. The full distribution function is solved from the Vlasov equation:

$$\frac{\mathrm{d}f_s}{\mathrm{d}t} = \frac{\partial f_s}{\partial t} + \mathbf{v} \cdot \frac{\partial f_s}{\partial \mathbf{r}} + \frac{Z_s e}{m_s}\left(\mathbf{E} + \frac{1}{c}\mathbf{v} \times \mathbf{B}\right) \cdot \frac{\partial f_s}{\partial \mathbf{v}} = 0, \tag{B.1}$$

where the distribution function for species s is $f_s = f_s(\mathbf{r}, \mathbf{v}, t)$, with mass m_s, and charge number Z_s (-1 for electrons). The electric and magnetic fields are $\mathbf{E}$ and $\mathbf{B}$ respectively, and are found by solving Maxwell's equation, using moments of f_s to find the charge and current density. The total time derivative along particle trajectories is represented by $\mathrm{d}/\mathrm{d}t$. The PIC method is Lagrangian in the sense that

a solution is obtained by the method of characteristics. Full-f PIC is unweighted precisely because the right hand side of (B.1) is zero. This method has been well-studied and applied; its limitations are well-known because numerical dispersion relations are able to be calculated [86–88].

It is typical in plasma theory to expand the distribution function into a relatively constant equilibrium distribution F_{0s} and a small perturbation δf_s such that $f_s = F_{0s} + \delta f$. Aydemir [89] took advantage of the properties of Monte Carlo integration to present a solution method which solves only for the perturbation. This method was later expanded by Parker, Lee [90], Denton, Kotschenreuther [91], and is now known as the δf-PIC method. It greatly reduces the impact of statistical noise compared to resolving the full distribution function f. The scheme *is* weighted in the sense that the right hand side of the kinetic equation for δf does not vanish, so each marker caries a *weight*, which changes with time along characteristics (see section B.1).

Because much of the dynamics has been replaced by a time-dependent weight in the δf scheme, a numerical dispersion relation based solely on the marker trajectories is not useful. In fact, for a linear problem, the particle trajectories are entirely deterministic. Therefore, to analyze the algorithm, the changing weights play the central role; the particle trajectories only serve to complicate this analysis. This appendix represents a full analytic treatment of the algorithm to seek an explanation for a numerical instability that occurs in the simplest of cases, and is converged on resolution.

For numerical simulations, a variation of the `GSP` code [92]) was used.

B.1 The Ω_H mode

It will be convenient to express the gyrokinetic equation in terms of

$$g_s \equiv h_s - \frac{Z_s}{T_s} F_{0s} \langle \phi \rangle_{\mathbf{R}} = \langle \delta f_s \rangle_{\mathbf{R}}, \tag{B.2}$$

so that one avoids a numerical instability resulting from multiple time derivatives in the gyrokinetic equation [93, 94]. In terms of g_s, the gyrokinetic equation (2.45) in the electrostatic limit reads:

$$\begin{aligned} &\frac{\partial g_s}{\partial t} + \left(v_\parallel \mathbf{b} + \mathbf{v}_{ds} + \frac{c}{B} \mathbf{b} \times \nabla \langle \phi \rangle_{\mathbf{R}} \right) \cdot \nabla g_s - \langle C_{\mathrm{GK}} [g_s] \rangle_{\mathbf{R}} \\ &\quad = -\frac{Z_s e}{T_s} F_{0s} \mathbf{b} \cdot \nabla \langle \phi \rangle_{\mathbf{R}} - \frac{c}{B} \left(\mathbf{b} \times \nabla \langle \phi \rangle_{\mathbf{R}} \right) \cdot \nabla F_{0s}, \end{aligned} \tag{B.3}$$

where F_{0s} is Maxwellian in this appendix. Equation (B.3) is is closed by solving for the leading contribution to Poisson's equation (quasineutrality):

$$\sum_s Z_s e \int \langle g_s \rangle_{\mathbf{r}} \, \mathrm{d}^3 \mathbf{v} + \frac{Z_s^2 e^2}{T_s} \int F_{0s} \left[\langle \langle \phi \rangle_{\mathbf{R}} \rangle_{\mathbf{r}} - \phi \right] \mathrm{d}^3 \mathbf{v} = 0, \tag{B.4}$$

which in Fourier-space can be written as:

$$\tilde{\phi}_{\mathbf{k}} = \frac{\sum_s Z_s e \int J_0 \tilde{g}_s \, \mathrm{d}^3 \mathbf{v}}{\sum_s \left(Z_s^2 e^2 / T_s \right) \left[1 - e^{-k_\perp^2 \rho_s^2 / 2} I_0 \left(k_\perp^2 \rho_s^2 / 2 \right) \right]}. \tag{B.5}$$

The modified Bessel function I_0 enters the analysis through the identity:

$$\Gamma_{0s} \equiv 2 \int_0^\infty \left[J_0\left(a v_\perp\right)\right]^2 v_\perp dv_\perp = e^{-a^2/2} I_0\left(\frac{a^2}{2}\right) \approx 1 - \frac{1}{2} k_\perp^2 \rho_s^2, \tag{B.6}$$

where the latter approximation, useful later, is valid for $k_\perp \rho_s \ll 1$.

We shall concern ourselves with a simplified system: that of the Ω_H mode [95]. It is the simplest possible gyrokinetic system with multiple kinetic species, yet it exhibits the converged numerical instability presented here. In this regime, we make the following assumptions, in addition to those made in chapter 2:

- Electrostatic perturbations ($\beta \to 0$)
- Linear dynamics only (small perturbations)
- Uniform, triply-periodic, shearless slab geometry ($\nabla \mathbf{B} = 0$)
- Uniform Maxwellian equilibrium ($\nabla F_0 = 0$)
- Singly-charged ions and kinetic electrons with $T_e = T_i$
- Long-wavelength approximation ($k_\perp \rho_i \ll 1$)

Note that, as we shall discuss later, it is possible to stabilize the numerical instability by relaxing the first of these assumptions. However, the instability is robust to the latter five assumptions, which are made here solely for simplicity.

Since the $v_\perp$ coordinate only enters the problem through the gyro-averages, it will be convenient to eliminate it from the problem. To this end, we define the

μ-averaged distribution $\bar{g}_s$ as:

$$\bar{\tilde{g}}_s \equiv 2\pi \int_0^\infty J_0 \left(\frac{k_\perp v_\perp}{\Omega_s} \right) \tilde{g}_s v_\perp dv_\perp, \tag{B.7}$$

where $\tilde{g}_s(\mathbf{k})$ is the Fourier transform of $g_s(\mathbf{R})$. In taking the long-wavelength limit, let $J_0 \approx 1$, $\Gamma_{0e} \approx 1$, and $\Gamma_{0i} \approx 1 - k_\perp^2 \rho_i^2/2$. So the simplified set of equations becomes:

$$\frac{\partial \bar{g}_s}{\partial t} + v_\parallel \frac{\partial \bar{g}_s}{\partial z} = -\frac{Z_s e}{T} v_\parallel F_{0s\parallel} \frac{\partial \phi}{\partial z} \tag{B.8}$$

$$\tilde{\phi} = \frac{2T}{n_i e k_\perp^2 \rho_i^2} \sum_s Z_s \int_\infty^\infty \bar{\tilde{g}}_s dv_\parallel \tag{B.9}$$

with $F_{0s\parallel} \equiv (n_{0s}/v_{ts}\sqrt{\pi})\, e^{-v_\parallel^2/v_{ts}^2}$. Note that equations (B.8) and (B.9) are directly analogous to the Langmuir plasma wave in the limit $k_\perp \gg k_\parallel$ and $T_\parallel \gg T_\perp$, with an effective Debye length of $\lambda_D = n_i e^2 \rho_i / T_i$. Therefore, this instability should also be present in a Vlasov δf-PIC code in the appropriate limit. Note that although the form of the equations are identical, the physical interpretation of (B.9) is distinct from Poisson's equation: it is instead the leading-order finite Larmor radius correction to the polarization density [96].

We can find the corresponding dispersion relation by Laplace-transforming equation (B.8) and inserting into (B.9) to obtain:

$$k_\perp^2 \rho_i^2 = Z' \left(\frac{\omega}{k_\parallel v_{ti}} \right) + Z' \left(\frac{\omega}{k_\parallel v_{te}} \right). \tag{B.10}$$

The Ω_H mode is found by expanding the plasma dispersion function $Z(\zeta)$ for large

argument in (B.10). Including complex corrections, the frequency is approximated by:

$$\omega = \omega_0 - i\sqrt{\frac{\pi v_{ti}}{2v_{te}}}\frac{\omega_0^3}{k_\parallel^2 v_{ti}^2}e^{-\omega_0^2/k_\parallel^2 v_{ti}^2}, \tag{B.11}$$

where:

$$\omega_0 \equiv \frac{k_\parallel v_{te}}{k_\perp \rho_i}. \tag{B.12}$$

The wave is therefore Landau-damped. Due to its high frequency, one requires very small time-steps to resolve it, so it is easy to mistake this instability for a simple violation of the CFL condition [97]. However, the numerical instability under consideration here is converged on time-step if the Ω_H mode is resolved accordingly.

B.2 The δf-PIC algorithm

This section details the δf-PIC method of solving equations (B.8) and (B.9), taking advantage of two powerful multi-dimensional techniques: the method of characteristics, and Monte-Carlo integration.

With the method of characteristics, we can reduce an n-dimensional partial differential equation to a set of ordinary differential equations along characteristic curves that define the proper time derivative. This will give us the solution along any appropriate characteristic curve, headed by a *marker* (or "particle"), labelled in this thesis by Greek indices. The species index will be taken to be implicit in the marker index, so where convenient we will write, for example, Z_α instead of $Z_{s(\alpha)}$. Define a marker weight, which is just the normalized solution of the gyrokinetic

equation along its characteristic trajectory:

$$w_\alpha \equiv \frac{\bar{g}_{s(\alpha)}\left(\mathbf{R}_\alpha, v_{\parallel\alpha}\right)}{F_{0s(\alpha)}} = \frac{\bar{g}_\alpha}{F_{0\alpha}}. \tag{B.13}$$

As such, (B.8) becomes:

$$\frac{dw_\alpha}{dt} = -\frac{Z_\alpha e}{T_\alpha} v_\parallel \left(\frac{\partial \phi}{\partial z}\right)_{\mathbf{r}=\mathbf{R}_\alpha}, \tag{B.14}$$

which is the solution of the gyrokinetic equation along characteristic curves defined by:

$$\frac{dx_\alpha}{dt} = 0, \; \frac{dy_\alpha}{dt} = 0, \; \frac{dz_\alpha}{dt} = v_{\parallel\alpha}. \tag{B.15}$$

A marker's position at any time is:

$$\mathbf{R}_\alpha(t) = \left(x_{\alpha 0}, \, y_{\alpha 0}, \, z_{\alpha 0} + v_{\parallel\alpha} t\right). \tag{B.16}$$

Some authors choose to normalize the weight by the full distribution f (such that $w = \delta f / f$). This would introduce a factor of $1/(1 - w_\alpha)$ to the right-hand side of (B.14). Even so, the numerical instability remains, and when linearized for small perturbations, (B.14) is recovered.

In order to solve (B.13), it remains to find $\partial\phi/\partial z$ at the marker location z_α. We will use a spatial grid to aid in this, with a 3D interpolant function $S_3(\mathbf{r}) = S(x/\Delta x)S(y/\Delta y)S(z/\Delta z)$, where S can be one of many possible shape functions (see reference [86]), and Δx, Δy, and Δz are the grid spacings in the x, y, and z

directions respectively. Without a loss of generality, we will take S here to be the linear interpolant function:

$$S(x) \equiv \begin{cases} 1 - |x|, & \text{if } |x| < 1 \\ 0, & \text{otherwise.} \end{cases} \tag{B.17}$$

Therefore, if we know $\partial\phi/\partial z$ on grid points labelled by $\mathbf{r}_i$, we can find the corresponding value at location of marker α by:

$$\frac{\partial\phi}{\partial z_\alpha} = \left(\frac{\partial\phi}{\partial z}\right)_{\mathbf{r}=\mathbf{R}_\alpha} = \sum_i S_3\left(\mathbf{R}_\alpha - \mathbf{r}_i\right) \frac{\partial\phi}{\partial z_i}. \tag{B.18}$$

Define the discrete Fourier transforms:

$$Q_{\mathbf{k}} = \mathcal{F}_D\left[Q(\mathbf{r}_i)\right] = \sum_i e^{-i\mathbf{k}\cdot\mathbf{r}_i} Q(\mathbf{r}_i), \tag{B.19}$$

$$Q_i = \mathcal{F}_D^{-1}\left[Q_{\mathbf{k}}\right] = \frac{1}{N_g} \sum_{\mathbf{k}} e^{i\mathbf{k}\cdot\mathbf{r}_i} \tilde{Q}(\mathbf{k}), \tag{B.20}$$

where $N_g = N_x N_y N_z$ is the total number of grid points and $\mathbf{k}$ is discretely-valued. Now, find $\partial\phi/\partial z$ on the grid point $\mathbf{r}_i$ in terms of the Fourier modes of ϕ:

$$\frac{\partial\phi}{\partial z_i} = \frac{1}{N_g} \sum_{\mathbf{k}} e^{i\mathbf{k}\cdot\mathbf{r}_i} i k_\parallel \phi_{\mathbf{k}}. \tag{B.21}$$

To proceed, we need a way of estimating the integral in (B.9) on the grid. We do this by means of Monte-Carlo integration [89], using the same interpolant as in

(B.18). Monte-Carlo is a method by which one expresses an arbitrary integral (in this case a one-dimensional integral in $v_\parallel$) as an expectation value over some probability distribution p, then estimates this expectation value as a discretely-sampled average. Formally,

$$\int_{-\infty}^{\infty} \bar{g}_s(v_\parallel) dv_\parallel = \int_{-\infty}^{\infty} \frac{\bar{g}_s(v_\parallel)}{p(v_\parallel)} p(v_\parallel) dv_\parallel = \left\langle \frac{g}{p} \right\rangle_p , \tag{B.22}$$

where $\langle \rangle_p$ is the expectation value over the probability distribution p, which obeys the following properties:

$$p > 0 \quad \forall v_\parallel \tag{B.23}$$

$$\int_{-\infty}^{\infty} p(v_\parallel) dv_\parallel = 1. \tag{B.24}$$

If we take $p = F_{0\parallel s}/n_{0s}$ by distributing markers according to a Maxwellian in $v_\parallel$, and have N discrete samples of $\bar{g}_s$, then we can write:

$$\int_{-\infty}^{\infty} \bar{g}_s(v_\parallel) dv_\parallel = \left\langle \frac{g}{p} \right\rangle_p = \frac{n_{0s}}{N} \sum_{\alpha=1}^{N} w_\alpha + \mathcal{O}\left(\frac{n_{0s} \mathrm{var}\,(w)}{\sqrt{N}} \right). \tag{B.25}$$

The extension to multiple dimensions can be found in reference [89].

To account for the spatial-dependence of (B.25), we use the interpolant function S_3 since the location at which we want the integral (on a grid point $\mathbf{r}_i$) is in general not the same as the marker positions $\mathbf{R}_\alpha$. This is perhaps the only non-rigorous part of the algorithm and may be what is responsible for unphysical behavior at large particle number.

Moving forward with this caveat in mind, we can estimate the charge density

at the spatial grid location $\mathbf{r}_j$:

$$q(\mathbf{r}_j) \equiv \sum_s Z_s e \int_{-\infty}^{\infty} \bar{g}(\mathbf{r}_j, v_\parallel) dv_\parallel \approx \frac{1}{N_c} e \sum_\beta n_{0\beta} Z_\beta S_3 \left(\mathbf{R}_\beta - \mathbf{r}_j\right) w_\beta. \tag{B.26}$$

The average number of particles of each species per grid cell is N_c, so that the total number of particles per species is $N_p = N_g N_c$. Finally, we can calculate $\phi_{\mathbf{k}}$ from the discrete Fourier transform of this quantity using (B.9):

$$\phi_{\mathbf{k}} = \frac{2T_i}{n_{0i} e^2 k_\perp^2 \rho_i^2} \sum_j e^{-i\mathbf{k}\cdot\mathbf{r}_j} q(\mathbf{r}_j) \tag{B.27}$$

B.3 Matrix form of the algorithm and existence of converged numerical instability

Now, once a suitable time-advancement algorithm is implemented to solve the ODEs, the entire algorithm is given by equations (B.14, (B.15), (B.18), (B.21), (B.27), and (B.26). Such a system has been implemented in the simplified `dk2d` code in 2D with a 2nd-order Runge-Kutta scheme.

By combining these equations, we find that the ODE for the marker weights is coupled linearly to the weights of all other markers. That is:

$$\dot{w}_\alpha = \sum_\beta M_{\alpha\beta}(t) w_\beta, \tag{B.28}$$

where:

$$M_{\alpha\beta}(t) = \frac{-2Z_\alpha Z_\beta v_\alpha}{N_p} \sum_{\mathbf{k},\mathbf{i},\mathbf{j}} S_3\left(\mathbf{R}_\alpha - \mathbf{r}_i\right) S_3\left(\mathbf{R}_\beta - \mathbf{r}_j\right) e^{i\mathbf{k}\cdot\left(\mathbf{r}_j - \mathbf{r}_i\right)} \frac{ik_\parallel}{k_\perp^2 \rho_i^2} \tag{B.29}$$

$$\approx \frac{-2Z_\alpha Z_\beta v_\alpha}{N_p} \sum_{\mathbf{k}} |S_\mathbf{k}|^2 e^{i\mathbf{k}\cdot\left(\mathbf{R}_\beta - \mathbf{R}_\alpha\right)} \frac{ik_\parallel}{k_\perp^2 \rho_i^2} \tag{B.30}$$

The last line is only an approximation because one cannot rigorously shift a discrete Fourier transform continuously. It is our experience, however, that using this approximation makes little qualitative difference to the behavior of the algorithm, and this is the analytic form taken in reference [98]. We will, however, be using the exact form unless stated otherwise. The time-dependence of the matrix elements (B.29) comes from that of the marker positions, through (B.15). Therefore, the δf-PIC algorithm is fundamentally a large coupled system of first-order ODEs with variable coefficients.

One can solve (B.28) semi-analytically only in the case where there is a single-mode (with a given $\mathbf{k}_\perp$ and $k_\parallel$) present, and the approximation made in (B.29) is valid. In this case, the solution is:

$$\mathbf{w}(t) = \mathbf{w}(t=0) \exp\left[\mathbb{A}(t)\right], \tag{B.31}$$

where here exp is the matrix-exponential and the elements of $\mathbb{A}$ are given by:

$$A_{\alpha\beta}(t) = \int_0^t M_{\alpha\beta}(t')dt' = \frac{-i}{k_\parallel\left(v_{\parallel\beta} - v_{\parallel\alpha}\right)} e^{ik_\parallel\left(z_{\beta 0} - z_{\alpha 0}\right)} \left(e^{ik_\parallel\left(v_{\parallel\beta} - v_{\parallel\alpha}\right)t} - 1\right) M_{\alpha\beta}. \tag{B.32}$$

When multiple Fourier-modes are allowed, this solution is not valid because then the matrix $\mathbb{M}$ fails to commute at different times ($\mathbb{M}(t_1)\mathbb{M}(t_2) \neq \mathbb{M}(t_2)\mathbb{M}(t_1)$).

In general, for multiple modes, (B.28) offers no immediate analytic solution. However, at any given moment during a simulation, we can take the matrix to be approximately constant, and use that to calculate the instantaneous eigenvalue spectrum. The time-evolution of the most unstable eigenvalue is given in figure B.2.

The system (B.28) can even be solved implicitly:

$$\mathbf{w}(t + \Delta t) = (\mathbb{M}(t + \Delta t)\Delta t - \mathbb{I})^{-1}\, \mathbf{w}(t), \tag{B.33}$$

where $\mathbf{w}$ is a column-vector of all the particle weights. Figure B.1 compares the relative difference in the solution obtained by the code `dk2d`, and solving the linear system B.28 explicitly and implicitly. Note that the explicit matrix solution is identical to within machine precision to the δf-PIC algorithm. In fact, it should *be* the algorithm, with no approximations made.

Another property of the matrix $\mathbb{M}$ is that it is poorly conditioned (see the evolution of the condition number in figure B.3). This implies that the dynamics are not reversible without a roundoff-error catastrophe, but it is unclear if this provides insight to the numerical instability discussed below.

Note that solving this matrix system is much more inefficient than the particle algorithm itself. In a δf particle-in-cell code, this matrix never needs to be stored, calculated, or inverted in its entirety. Nevertheless, equation (B.28) is the exact analytic form of the linear algorithm. We find that the numerical instability presented

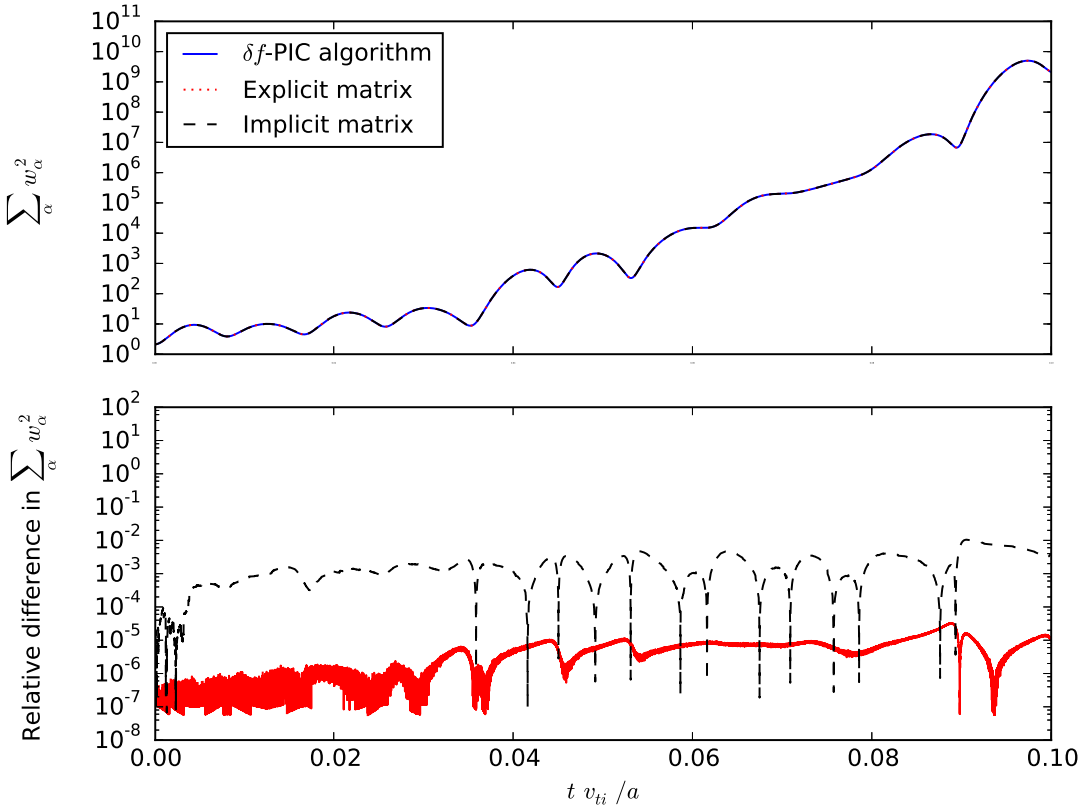

Figure B.1: Comparing the δf-PIC algorithm to a direct solve of the matrix system (B.28). The sum of the squared particle weights is displayed in the upper chart. The relative difference compared to the results of an actual δf-PIC code: $|\left[\sum_\alpha w_\alpha^2\right]_{\text{PIC}} - \left[\sum_\alpha w_\alpha^2\right]_{\text{matrix}}| / \left[\sum_\alpha w_\alpha^2\right]_{\text{PIC}}$ is shown below. The explicit matrix is accurate to machine precision, while the implicit scheme suffers from a small amount of numerical dissipation due to the finite-time-step. The explicit and implicit schemes used here are forward and backward Euler respectively, with $\delta t = 10^{-6} a/v_{ti}$. The resolution is $N_y = 4$, $N_z = 4$, and 20 particles per species per grid cell. A low resolution is necessary due to the need to invert a dense matrix of size $N_p \times N_p$ every time-step.

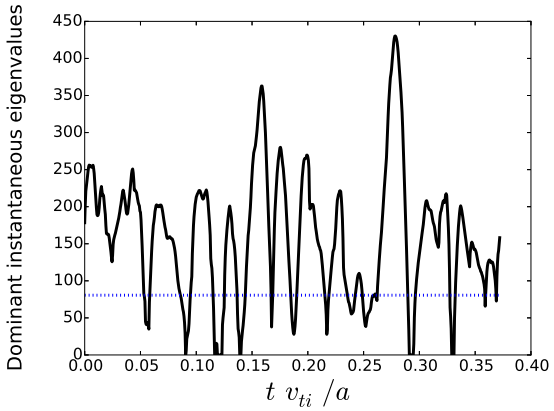

Figure B.2: Time-evolution of the largest real eigenvalues of matrix B.29. The horizontal dotted line marks the approximate average growth rate of the code ($\gamma \approx 80.6$) for the parameters: $N_y \times N_z = 4 \times 4$, $L_z = 2\pi a$, $L_y = 40\pi\rho_i$, $N_p = 320$.

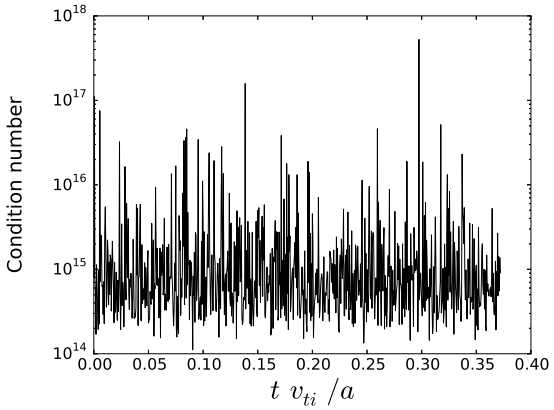

Figure B.3: Time-evolution of the condition number of matrix B.29. Same case as figure B.2

in the following section is a property of this matrix system itself.

B.4 Characterization of the numerical instability

Here, we detail the properties of the discovered numerical instability. In what follows, it will be useful to distinguish between the two separate instabilities observed: a *finite-particle* instability, which is difficult to characterize, and whose average growth rate generally decreases with increasing particle number. Indeed, there is not a clean exponential behavior associated with this numerical instability (see, *e.g.*, figure B.5). As the number of particles increases, one ultimately finds a *converged* numerical instability at some mode numbers, which does, in contrast, exhibit clear exponential/oscillatory behavior. It is this *unconditional* instability that we will chiefly concerns ourselves with in this section.

The standard, minimally-resolved case in which one can observe the converged numerical instability is: $L_y = 20\pi\rho_i$, $L_z = \pi a$, $N_y = 4$, $N_z = 4$, $m_i/m_e = 1849$, $N_c = 8000$.

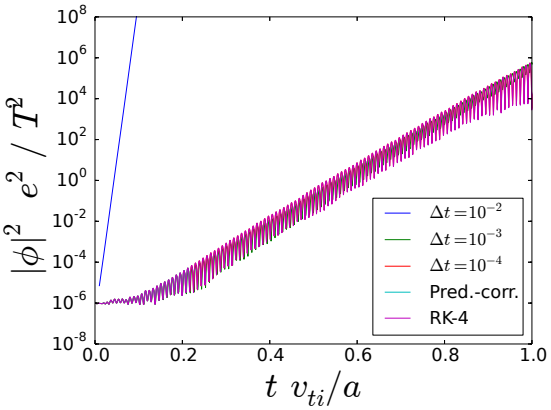

Figure B.4: Demonstrating the convergence of instability growth rate on time-step size and method. Second-order Runge-Kutta is the default, with a simple predictor-corrector scheme and fourth-order Runge-Kutta also shown (the latter two have $\Delta t = 10^{-4}$). At high step-size, the simulation is wildly unstable, which is to be expected from a violation of the CFL condition.

B.4.1 Convergence in time-step

As a basic check, we verify that we are not violating a CFL condition. By decreasing the growth rate and changing time-integration methods, we converge upon the same unstable solution. We are confident that we are converging upon the exact solution of the time-continuous equations (see figure B.4).

B.4.2 Convergence in particle number

In figure B.5, we illustrate the convergence of the unphysical growth rate on particle number. When initializing with random noise, it is expected that the initial size of the perturbation decreases with increasing particle number. However, there is a fixed growth rate one reaches at which we consider the solution converged.

Note also the non-exponential behavior when N_c is below the threshold. This is the finite-particle instability, which proves troublesome in some circumstances, requiring a large number of particles per cell to stabilize. While it is expected that

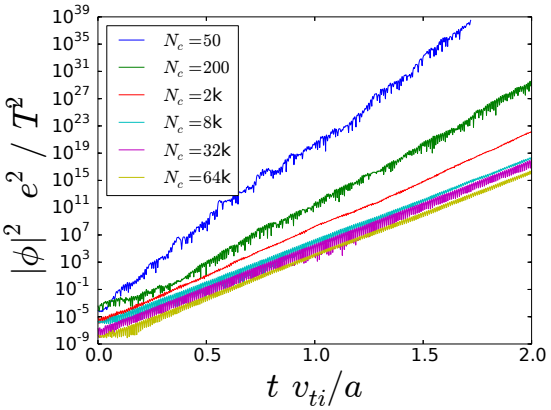

Figure B.5: Demonstrating the convergence of instability growth rate on particle number. Under-resolved cases ($N_c < 8000$) suffer from the poorly-behaved finite-particle instability.

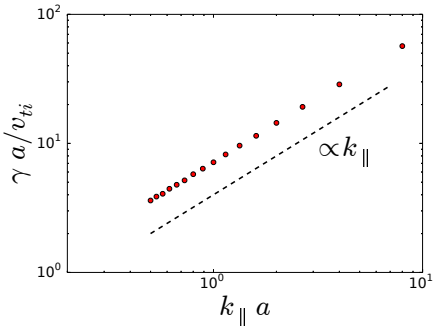

Figure B.6: Dependence of the unphysical growth rate on parallel wave number. The actual power law fit is $k_\parallel^{0.9976}$.

under-resolving the number of particles would cause a loss of accuracy, it is not clear why a numerical instability would result. It is this instability that is observed in figure B.5 and confirmed with the δf-PIC matrix (B.29) to be a fundamental feature of the algorithm. It is not clear if the converged numerical instability is another aspect of this finite-particle effect, or if they are in fact two separate instabilities arising in independent circumstances.

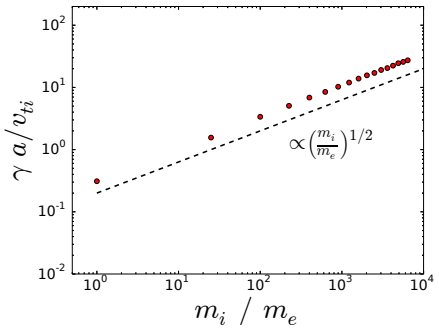

Figure B.7: Dependence of the unphysical growth rate on electron-ion mass ratio. Note the existence of instability at $m_e = m_i$. Actual power law fit is $(m_i/m_e)^{0.5131}$

B.4.3 Scaling with parallel wave number

When multiple modes are present (particularly a parallel mode and its counter-propagating partner) there is a clear direct linear relationship between the parallel wavenumber and the growth rate: see figure B.6. This is not particularly surprising: the arbitrary parallel length scale a only enters in defining $k_\parallel$ and the characteristic time a/v_{ti}.

Unlike in the perpendicular direction, when only one parallel mode exists in the system, the instability vanishes. This indicates that, even in the linear case, there is coupling between the parallel modes of ϕ that gives rise to this numerical instability. This question is studied further in the next section.

B.4.4 Scaling with mass ratio

Two kinetic species are required to observe the numerical instability. Typically, these are taken to be light electrons and heavy ions. In fact, this was used in the simplification that $\Gamma_{0e} = 1$, and $\Gamma_{0i} = 1 - k_\perp^2 \rho_i^2/2$. As the mass ratio is adjusted

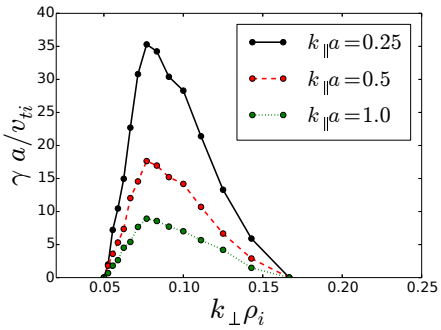

Figure B.8: Illustrating the dependence of the unphysical growth rate on perpendicular wave number at several values of $k_\parallel$.

using the same simplified field equation (B.9), we find that the growth rate scales linearly with $v_{te}/v_{ti} = \sqrt{m_i/m_e}$ (see figure B.7).

Note that a positive unphysical growth rate remains even when the mass ratio is taken to be unity (as in a positronic plasma). In this limit, the approximation used in (B.9) breaks down and electron Larmor radius effects play as much of a role as the "ions". So while the instability still exists with full Larmor radius effects, the important point here is that the separation of scales between the characteristic velocities of ions and electrons is *not* responsible for the instability, although it does have a scaling effect on the growth rate.

B.4.5 Scaling with perpendicular wave number

It is found that the numerical instability is only converged for a range of wavenumbers $k_\perp$. In figure B.8 is the relationship of the growth rate with $k_\perp$. A peak growth rate is clearly visible around $k_\perp \rho_i \approx 0.08$. The threshold for stability does not change with $k_\parallel$, which is to be expected from the linear scaling. The finite-particle instability has an even more complicated dependence on $k_\perp$, which is not

detailed here.

B.5 Unphysical mode coupling

A key property of the converged numerical instability is that it only occurs with more than one parallel Fourier mode present. In this section, we examine the coupling between parallel modes that occurs in the algorithm even when the equation we are trying to solve is linear. Any such mode coupling is thus unphysical.

To start, consider again the Ω_H system with the same assumptions as before and write the equation for the weight evolution as:

$$\dot{w}_\alpha = -\frac{Z_\alpha e}{N_g T} v_\alpha \sum_{k'_\parallel} e^{ik'_\parallel z_\alpha} S^*_{k'_\parallel} i k'_\parallel \phi_{k'_\parallel}, \tag{B.34}$$

where we used the approximation of equation (B.29). In this section, we will allow multiple $k_\parallel$ modes, but still only one $k_\perp$ mode. As such, $k_\perp$ is just a parameter that determines the strength of the potential, which from equation (B.26) and equation (B.27) is:

$$\phi_{k_\parallel} = \frac{2TeS_{k_\parallel}}{e^2 k_\perp^2 \rho_i^2 N_c} \sum_\alpha e^{-ik_\parallel z_\alpha} Z_\alpha w_\alpha. \tag{B.35}$$

Now, take the time derivative of equation (B.35), hitting both the position z_α and the weight w_α :

$$\dot{\phi}_{k_\parallel} = \frac{2S_k T}{e k_\perp^2 \rho_i^2 N_c} \sum_\alpha e^{-ik_\parallel z_\alpha} Z_\alpha \left(\dot{w}_\alpha - i k_\parallel v_\alpha w_\alpha \right). \tag{B.36}$$

We have $\dot{w}_\alpha$ from equation (B.34), but to proceed, we need a way of expressing w_α in terms of $\phi_{k_\parallel}$. To this end, make the ansatz (borne by observation) that all weights oscillate and grow at the same frequency and growth rate as the potential. Then

$$\phi \propto w_\alpha \propto e^{-i\omega t}. \tag{B.37}$$

Now using $w_\alpha = i\dot{w}_\alpha/\omega$, we can write equation (B.36) as:

$$\dot{\phi}_{k_\parallel} = \frac{2S_k T}{e k_\perp^2 \rho_i^2 N_c} \sum_\alpha e^{-ik_\parallel z_\alpha} Z_\alpha \dot{w}_\alpha \left(1 + \frac{k_\parallel v_\alpha}{\omega}\right) \tag{B.38}$$

$$-i\omega\phi_{k_\parallel} = -\frac{2S_k}{k_\perp^2 \rho_i^2 N_p} \sum_{k'_\parallel} \sum_\alpha S^*_{k'_\parallel} i k'_\parallel e^{i\left(k'_\parallel - k_\parallel\right) z_\alpha} v_\alpha \left(1 + \frac{k_\parallel v_\alpha}{\omega}\right) \phi_{k'_\parallel}, \tag{B.39}$$

where we substituted equation (B.34) and noted that $Z_\alpha^2 = 1$ for both singly-charged ions and electrons. Equation equation (B.38) has the form

$$\left(\omega^2 \mathbb{I} - \mathbb{C}\right) \boldsymbol{\phi} = 0 \tag{B.40}$$

where $\boldsymbol{\phi}$ is a column vector of all parallel modes $\phi_{k_\parallel}$, and $\mathbb{C}$ is a matrix, indexed by the parallel modes $k_\parallel$ and $k'_\parallel$:

$$C_{k_\parallel k'_\parallel} = \frac{2S_{k_\parallel} S^*_{k'_\parallel} k'_\parallel}{k_\perp^2 \rho_i^2 N_p} \sum_\alpha e^{i\left(k'_\parallel - k_\parallel\right) z_\alpha} v_\alpha \left(\omega + k_\parallel v_\alpha\right). \tag{B.41}$$

Equations equation (B.40) and equation (B.41) constitute a numerical dispersion relation of the δf-PIC algorithm, in which mode-coupling, while unphysical, is a

defining feature. We will find, however, that this mode-coupling does *not* explain the converged numerical instability. Therefore, there are features missing from equation (B.41), possibly due to the continuous shift in the discrete Fourier transform.

Consider the case of only one parallel mode. Then, equation (B.40) is:

$$\begin{aligned}\omega^2 &= \frac{2\left|S_{k_\parallel}\right|^2 k_\parallel}{k_\perp^2 \rho_i^2 N_p} \sum_\alpha v_\alpha \left(\omega + k_\parallel v_\alpha\right) \\ &\approx \frac{2\left|S_{k_\parallel}\right|^2 k_\parallel^2}{k_\perp^2 \rho_i^2} \frac{\sum_\alpha v_\alpha^2}{N_p} \approx \Omega^2,\end{aligned} \tag{B.42}$$

which, in the limit of infinite particles (in which $\sum_\alpha v_\alpha / N_p \to 0$) is just the Ω_H frequency, with finite-particle and finite-grid effects!

Now, in the case of two parallel modes: $\pm k_\parallel$, equation (B.40) becomes a 2×2 system, whose solution is given by $\det\left(\omega^2 \mathbb{I} \mp \mathbb{C}\right) = 0$. The elements of $\mathbb{C}$ are:

$$\begin{aligned}C_{11} &= \frac{2\left|S_{k_\parallel}\right|^2 k_\parallel}{k_\perp^2 \rho_i^2 N_p} \sum_\alpha v_\alpha \left(\omega + k_\parallel v_\alpha\right) \approx \Omega^2 \\ C_{22} &= -\frac{2\left|S_{k_\parallel}\right|^2 k_\parallel}{k_\perp^2 \rho_i^2 N_p} \sum_\alpha v_\alpha \left(\omega - k_\parallel v_\alpha\right) \approx \Omega^2 = C_{11} \\ C_{12} &= -\frac{2\left|S_{k_\parallel}\right|^2 k_\parallel}{k_\perp^2 \rho_i^2 N_p} \sum_\alpha e^{-2ik_\parallel z_\alpha} v_\alpha \left(\omega + k_\parallel v_\alpha\right) \\ C_{21} &= \frac{2\left|S_{k_\parallel}\right|^2 k_\parallel}{k_\perp^2 \rho_i^2 N_p} \sum_\alpha e^{2ik_\parallel z_\alpha} v_\alpha \left(\omega - k_\parallel v_\alpha\right),\end{aligned} \tag{B.43}$$

where the approximations are valid in the limit of infinite particle number. So the

solution of the matrix equation is given by:

$$\begin{aligned} 0 &= \left(\omega^2 - C_{11}\right)^2 + C_{12}C_{21} \\ &= \omega^4 + C_{11}^2 - 2\omega^2 C_{11} + C_{12}C_{21} \\ &= \omega^4 + \Omega^4 - 2\omega^2\Omega^2 + b\omega\Omega^3 + c\Omega^4 - 2\omega^2\Omega^2 d, \end{aligned} \tag{B.44}$$

and we have defined the following dimensionless quantities:

$$b \equiv 2i\frac{\Omega}{k_\parallel}\frac{\mathrm{Im}\left[\left(\sum_\alpha e^{2ik_\parallel z_\alpha} v_\alpha^2\right)\left(\sum_\alpha e^{-2ik_\parallel z_\alpha} v_\alpha\right)\right]}{\left(\sum_\alpha v_\alpha^2\right)^2} \tag{B.45}$$

$$c \equiv \frac{\left|\sum_\alpha e^{2ik_\parallel z_\alpha} v_\alpha^2\right|^2}{\left(\sum_\alpha v_\alpha^2\right)^2} \tag{B.46}$$

$$d \equiv \frac{1}{4}\frac{\Omega^2}{k_\parallel^2}\frac{\left|\sum_\alpha e^{2ik_\parallel z_\alpha} v_\alpha\right|^2}{\left(\sum_\alpha v_\alpha^2\right)^2}. \tag{B.47}$$

The behavior of these quantities are such that $0 < c < 1$, $d > 0$. In the course of simulation, b oscillates and is not positive-definite, so we will assume it time-averages to zero. Furthermore, in the limit of infinite particles, $d \to 0$ because of the single power in v_α (which is another reason to neglect b). Therefore, equation (B.44) can be reduced to:

$$\omega^4 - 2\omega^2\Omega^2 + \Omega^4\left(1 + c\right), \tag{B.48}$$

in which $\mathrm{Im}\omega > 0$ for any $c > 0$:

$$\gamma \equiv \mathrm{Im}\omega = \frac{\Omega}{2}\sqrt{\sqrt{1+c^2}-1}. \tag{B.49}$$

In the limit of $c \ll 1$, we have $\gamma \approx c\Omega/2$. However the quantity c does indeed vanish in the limit of increasing particle number, albeit slowly. This might be responsible for the finite-particle instability.

B.6 Mitigation schemes

That such a catastrophic instability is fundamental to the δf-PIC algorithm is surprising since there are many examples of it reproducing good physics [58, 99]. To get good results, other groups must have either avoided this particular range in parameter space, or employed one of several mitigation methods that have been found to stabilize the resolved instability. From most- to least-physically satisfying, this section presents possible methods of mitigating the numerical instability.

B.6.1 Small, finite-β

Ignoring compressive ($\delta B_\parallel$) fluctuations, the more general form of the gyrokinetic equation reads:

$$\begin{aligned}\frac{\partial g_s}{\partial t} + \left(v_\parallel \mathbf{b} + \mathbf{v}_{ds} + \frac{c}{B}\mathbf{b}\times\langle\chi\rangle_{\mathbf{R}}\right)\cdot\nabla g_s - \langle C_{\mathrm{GK}}\left[g_s\right]\rangle_{\mathbf{R}} \\ = -\frac{Z_s e}{T_s}F_{0s}\mathbf{b}\cdot\nabla\langle\chi\rangle_{\mathbf{R}} - \left(\mathbf{v}_{ds} + \frac{c}{B}\mathbf{b}\times\langle\chi\rangle_{\mathbf{R}}\right)\cdot\nabla F_{0s}.\end{aligned} \tag{B.50}$$

where $\chi = \phi - A_\parallel v_\parallel / c$, and $\mathbf{A}$ is the perturbed vector potential such that $\delta\mathbf{B} = \nabla \times \mathbf{A}$. Here, the definition of g_s is altered to be $g_s = h_s - Z_s e F_{0s} \langle \chi \rangle_{\mathbf{R}} / T_s$. The parallel component of Ampere's law is:

$$k_\perp^2 A_\parallel = \frac{\sum_s Z_s e \int J_0 g_s v_\parallel \, \mathrm{d}^3\mathbf{v}}{k_\perp^2 - \sum_s Z_s^2 e^2 e^{-k_\perp^2 \rho_s^2/2} I_0 \left(k_\perp^2 \rho_s^2/2\right)/2}. \tag{B.51}$$

With these generalized equations, one can solve for the kinetic Alfvén wave, which becomes the Ω_H mode in the limit $\beta \ll m_e/m_i$. As long as one avoids this regime by running at a small, but finite β, the Alfvén wave is stable, unlike the Ω_H mode.

In physics, one rarely encounters plasmas of interest with $\beta < m_e/m_i$, so this is a somewhat physically-satisfying solution. Some authors have discovered modifications to the algorithm, such as a split-weight scheme [93] or by using canonical momentum coordinates [58], that may make the electromagnetic algorithm more efficient or accurate.

B.6.2 Piecewise-constant fields

Another way to stabilize the converged instability is to alter the way the gradient of the potential is calculated at the location of the particle. In (B.18), we calculated the gradient on the grid, then interpolated that to the particles. Instead, one can use the *local* gradient at the particle location given ϕ on the nearby grid points. Then, all particles within a grid cell would experience the same electric field.

For example, if instead of (B.18), we had:

$$\frac{\partial \phi}{\partial z_\alpha} = \frac{1}{\Delta z}\left(\phi_{z_{i'+1}} - \phi_{z_{i'}}\right) \tag{B.52}$$

$$i' \equiv \mathrm{mod}\left[\mathrm{floor}\left(\frac{z_\alpha}{\Delta z}\right), N_z\right], \tag{B.53}$$

then the algorithm appears to be only unstable to the finite-particle instability. The reason this occurs is unclear.

This method is not without its costs, however. Besides a general loss of accuracy by taking the electric field as piece-wise constant, one introduces a self-force from a particle experiencing a field from its own charge. This occurs because the interpolation from the particle to the grid is no longer symmetric with the corresponding interpolation from the grid to the particle [86]. This can be seen by noting that the elements $A_{\alpha\alpha}$ in (B.29) vanish. By altering the algorithm with (B.52), this feature is lost. Though no detailed investigation on the consequences of this scheme has been performed here, this would surely introduce undesirable effects.

B.6.3 Collision operator / coarse-graining

Until now, we have considered only the collisionless problem. Implementing a physically-rigorous collision operator into δf-PIC is a challenge, and one to which the community has not yet reached consensus on an acceptable solution. The implementation of collisions used in `ROMA` is based on the pitch-angle operator of Broemstrup [92], which itself is an extension of the Chen-Parker coarse-graining

method [100].

Based on our simulations, an effective pitch-angle collision frequency of about $\nu \sim 30 v_{ti}/a$ is required the stabilize the instability. For this case, the growth rate is comparable, so our interpretation here is that this strong of a collision frequency simply introduces strong enough damping to counteract the instability.

B.6.4 Mode filtering

Perhaps the least satisfying way to stabilize the algorithm is to simply ignore the ones that are unphysically unstable. Doing so involves employing a mask in Fourier space such that after $\phi_{\mathbf{k}}$ is calculated, one negates a set of modes that suffer from numerical instability. This works because, as evident from figure B.8, only a range of $k_\perp$ are unstable. Although it has not been analyzed here, it is possible that in toroidal geometry with magnetic shear, a smaller range of modes might be unstable and could make this technique more palpable. Furthermore, if there is a way to *a priori* predict when such modes will be unstable, as we have attempted to find, filtering could be a satisfying solution if it were a function of grid resolution.

B.7 Conclusion

In this work, we presented the analytic form of the δf-PIC algorithm. In doing so, a fundamental numerical instability is exposed: one that is due to under-resolution in particle number. While having too few particles certainly leads to inaccuracy [98], there is no clear reason why a strong numerical instability should

result. Furthermore, there is an even more troubling instability that is converged on particle number. There is therefore no way to use the algorithm to distinguish the instability as unphysical, and it presents itself clearly in the simplest multi-species gyrokinetic situation: the Ω_H mode in a periodic slab.

Responsible computational physics requires a fundamental understanding of the discrete equations of a proposed algorithm and a clear expression of its limitations. There is much work to be done in this regard with the δf-PIC algorithm. A statistical analysis of the set of ODEs (B.28) is warranted, though it is not clear how such an analysis would proceed. Once a fundamental cause for the unphysical instability is found, work can proceed in mitigating the undesired behavior at a fundamental level.

Appendix C: Generalized Gaussian quadrature

A module called `genquad` has been developed for `GS2` and implemented in the `alphas` branch[1] that generalizes the Gaussian quadrature scheme for isotropic F_0 in the domain $0 < v < \infty$ or $0 < v < v_{\max}$. It is a generalization of the technique that Landreman and Ernst [101] applied to the Maxwellian distribution.

C.1 Motivation

Throughout the simulation, we wish to perform integrals of the form:

$$I = \int_0^\infty \omega(v) g(v) dv, \tag{C.1}$$

where $\omega(v)$ is a suitable weight[2] function associated with the quadrature scheme. In general, it is identical to the orthogonality-weight-function associated with some set of orthogonal polynomials. For example, the Legendre polynomials (which are currently used in `GS2` in the domain $0 < v < v_{\text{cut}}$) obey $\int_{-1}^{1} P_m(x) P_n(x)\, dx \propto \delta_{m,n}$.

[1] as of revision 3602

[2] Not to be confused with the integration node weights w_i.

So for this case $\omega(v) = 1$ and

$$\int_0^{vcut} g(v)dv \approx \sum_{i=1}^{N} w_i g(v_i) \tag{C.2}$$

Here, v_i are the roots of the Nth Legendre polynomial shifted to the domain $(0, v_{cut})$, and w_i are the associated integration weights.

The above choice of weight function (and thus quadrature scheme) is somewhat arbitrary, except for the following important observation. In equation (C.2), we are making the statement that g is well-approximated by a polynomial for $0 < v < v_{cut}$. In fact, if g *is* a polynomial of degree $2N - 1$ or less, then Gaussian quadrature provides the *exact* value of the integral. Otherwise, it exhibits *spectral accuracy*, which means that the error decreases exponentially with N.

When g is approximately Maxwellian and $v_{cut} \approx 2v_{ts}$, this is a reasonable approximation. However, for fast particles, there is a long tail that is necessary to resolve, which is very difficult to do so directly with polynomials. Figure C.1 compares the fit of a 10th-order polynomials to the Maxwellian and figure C.2 compares a slowing-down type distribution (1.20) to its own 10th-order polynomial fit. The inaccuracy of the latter is clear. This same inaccuracy could, in principle, be replicated for a Maxwellian if v_{cut} is increased, along with a linear increase in resolution.

Therefore, we desire a more judicious choice of weight function ω. We choose to use F_0 itself, whether Maxwellian or any other form. Then, we are simply making the assertion that g/F_0 is approximately polynomial, which is hopefully a more

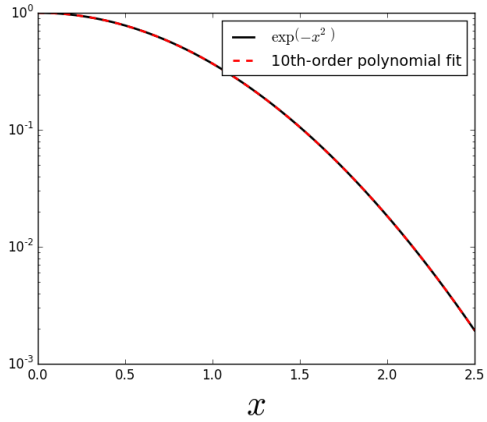

Figure C.1: Showing the fit of a Maxwellian between $0 < x < 2.5$ to its 10th-order polynomial fit.

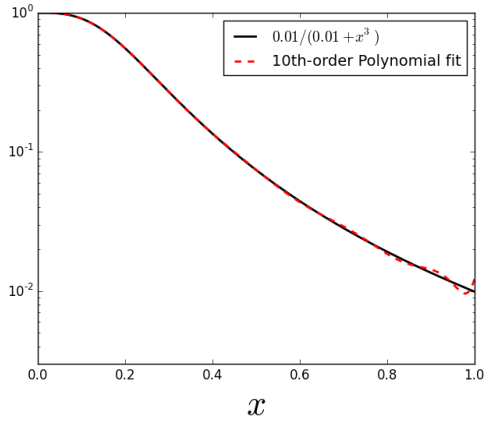

Figure C.2: Fitting a slowing-down-type distribution to its 10th-order polynomial fit.

correct statement. With this module implemented, GS2 should in principle be able to calculate integrals with an arbitrary $F_0(v)$ while retaining spectral accuracy.

C.2 Algorithm

The algorithm we use to calculate these weights and associated abscissae (*i.e.*, integration nodes) is a Stieltjes procedure [102], which generates a set of polynomials that are orthogonal with respect to any positive-definite weight function. The zeroes and weights for integration can then be found via an eigenvalue decomposition of the

Jacobi matrix [102]. More naive methods, such as Gram-Schmidt orthogonalization, or Newton-Raphson root-finding, fail to produce a well-conditioned algorithm.

In this section, we will describe the procedure for an integration domain $0 < v < \infty$, but is trivially generalized to finite or doubly-infinite domains. Let our target polynomials π_n be orthogonal in the sense that

$$\int_0^\infty \omega(v)\pi_n(v)\pi_m(v)dv \propto \delta_{nm}, \tag{C.3}$$

where δ_{mn} is the Kronecker delta. Also, let these polynomials be defined by a set of recursion coefficients a_n and b_n such that:

$$\pi_{n+1}(v) = (v - a_n)\,\pi_n(v) - b_n\pi_{n-1}(v), \tag{C.4}$$

and let $p_0 = 1$. Our task is to find the coefficients for which C.3 holds for arbitrary $\omega(v)$. We do this inductively: suppose we know the coefficients $a_0, \ldots, a_{n-1}$ and $b_0, \ldots, b_{n-1}$ (and hence can calculate the values of the polynomials up to π_n), then it is possible to find the next coefficients a_n and b_n. To see how, first multiply equation (C.4) by π_n and integrate, obeying the orthogonality relation equation (C.3). We find:

$$a_n = \frac{\int_0^\infty \omega(v)v\pi_n^2(v)dv}{\int_0^\infty \omega(v)\pi_n^2(v)dv}. \tag{C.5}$$

Similarly multiplying the same equation by π_{n-1}:

$$b_n = \frac{\int_0^\infty \omega(v)\pi_n^2(v)dv}{\int_0^\infty \omega(v)\pi_{n-1}^2(v)dv}, \tag{C.6}$$

where we used $\int \omega(v)\pi_n\pi_n dv = \int v\pi_{n-1}\pi_n dv$, which can also be obtained from equation (C.4) by shifting n by one. At this point, the success of the algorithm rests on accurately computing the integrals in equation (C.5) and equation (C.6). This is done with the `QUADPACK` library [103], a robust and widely used adaptive numerical integration toolset.

Once these coefficients are obtained up through $N-1$, construct a diagonal symmetric matrix whose diagonal elements are a_n, and the off-diagonal elements are $\sqrt{b_n}$. This is the *Jacobi matrix*, and its eigenvalues define the zeros of the polynomials π_n (which are also the integration abscissae), and the square of first element of each eigenvector are the corresponding integration weights [104]. This completes the algorithm.

C.3 Using the routine

To use the module in Fortran, compile and include the `genquad` module, and call the routine accordingly:

```
call get_quadrature_rule(func,Npts,a,b,abscissae,weights,inf_flag1,inf_flag_2)
```

The arguments are defined as follows:

- `func` is a pointer to a function that defines ω from C.1, defined in the code as

`external`, and takes only one argument. Function must be declared as "external" in the calling routine.

- `Npts` is the desired number of integration points
- `a`: lower bound of integration
- `b`: upper bound of integration
- `abscissae` (output): the points used to evaluate an integral (the points x_i below)
- `weights` (output): the integration weights so that $\int_a^b f(x)\omega(x)dx \approx \sum_i w_i f(x_i)$ is spectrally accurate
- `inf_flag1` (optional input): If `true`, lower bound is $-\infty$ instead of `a`. Default is `false`.
- `inf_flag2` (optional input): If `true`, upper bound is ∞ instead of `b`. Default is `false`.

C.4 Validation

To verify the accuracy of the integrals performed by this method, several test cases were set up. Four integration weights, each of which were used to estimate four integrands, were tested over a range of resolutions. The weight functions are:

- Gaussian: $\omega_1(v) = e^{-v^2}$, for $-\infty < v < \infty$
- Exponential: $\omega_2(v) = e^{-v}$, for $0 < v < \infty$
- "Slowing-down", shifted domain: $\omega_3 = \frac{1}{0.1+10v^3}$, for $-1 < v < 4$

- Lorentzian: $\omega_4 = \frac{1}{1+v^2}$, for $0 < v < 4$

These were combined to integrate the functions:

- Polynomial: $g_1(v) = 5v^5 + v^4 - 3v^3 + 7v^2 - 10v + 9$
- Trigonometric: $g_2(v) = \cos(4v)$
- Hyperbolic: $g_3(v) = \tanh(2v + 1)$
- Exponential: $g_4(v) = 10\exp(-v^4 + 2v^2)$

Giving a total of 16 integrals that were estimated. For example, one such integral is

$$I_{4,3} = \int_0^4 \omega_4(v) g_3(v) dv = \int_0^4 \frac{\cos(4v)\, dv}{1 + v^2} \tag{C.7}$$

Estimates of the above integrals are compared against high-resolution results from `Mathematica` to give an error. The results are shown in Figure C.3. The polynomial converges to machine precision quickly, as expected, since Gaussian integration is exact for polynomials of order $2N - 1$. The other, more complicated functions, exhibit error which decays exponentially, indicative of spectral accuracy.

The reader might be concerned that the numerical estimates for integrals such as I_{13} are slow to converge. This is to be expected for the same reason as before: functions like the hyperbolic tangent are not easily approximated by polynomials from 0 to ∞. To ease this concern, table C.1 compares the abscissae and weights for the ω_1 integrals to Gauss-Hermite quadrature, to which they ought to be identical, and are to within three significant figures of double precision. We conclude that

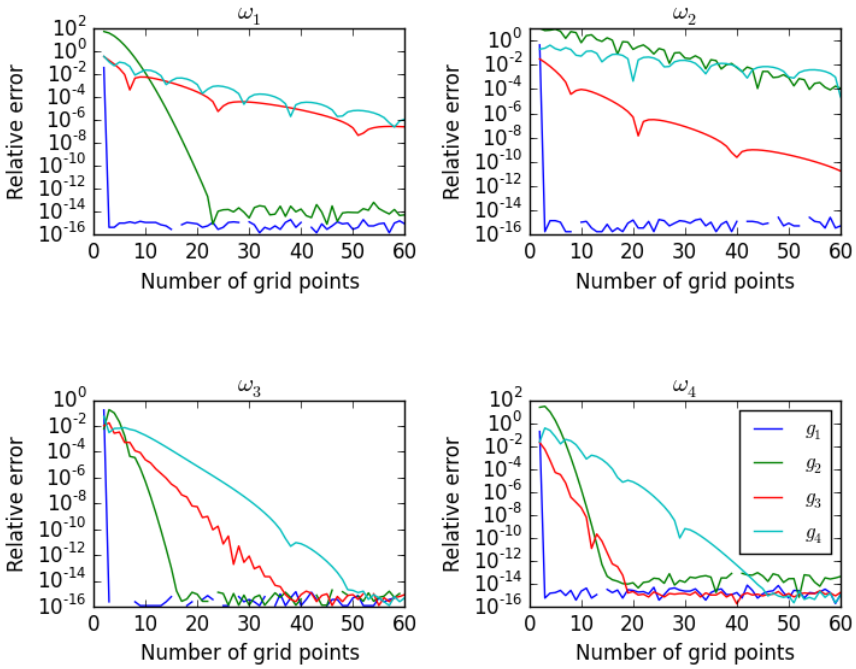

Figure C.3: Plotting the relative error $|(I_{\text{estimate}} - I_{\text{exact}})/I_{\text{exact}}|$ for all sixteen combinations of weights ω_i and test functions g_j at increasing resolution.

Gaussian quadrature is at a basic level ill-equipped to calculate these particular integrals, and that our scheme successfully reproduces established quadrature rules.

Table C.1: The Gauss-Hermite quadrature rule as predicted by this algorithm, compared to the actual Gauss-Hermite algorithm, for $N = 20$. The maximum relative error in the abscissae is 1.89×10^{-14}, and that of the weights is 2.61×10^{-13}.

i	$(v_i)_{\text{est}}$	$(v_i)_{\text{actual}}$	$(w_i)_{\text{est}}$	$(w_i)_{\text{actual}}$
1	-5.3874808900112328	-5.3874808900111999	2.2293936455341707E-013	2.2293936455340001E-013
2	-4.6036824495507460	-4.6036824495506998	4.3993409922731292E-010	4.3993409922730000E-010
3	-3.9447640401156243	-3.9447640401155999	1.0860693707692838E-007	1.0860693707690000E-007
4	-3.3478545673832154	-3.3478545673831999	7.8025564785320700E-006	7.8025564785320006E-006
5	-2.7888060584281291	-2.7888060584280998	2.2833863601635451E-004	2.2833863601630001E-004
6	-2.2549740020892766	-2.2549740020893001	3.2437733422378706E-003	3.2437733422379998E-003
7	-1.7385377121165868	-1.7385377121165999	2.4810520887463609E-002	2.4810520887460000E-002
8	-1.2340762153953226	-1.2340762153953000	0.10901720602002375	0.11090172060200000
9	-0.73747372854539395	-0.73747372854540005	0.28667550536283415	0.28667550536280001
10	-0.24534070830090093	-0.24534070830089999	0.46224366960061003	0.46224366960059998
11	0.24534070830090127	0.24534070830089999	0.46224366960061003	0.46224366960059998
12	0.73747372854539406	0.73747372854540005	0.28667550536283398	0.28667550536280001
13	1.2340762153953233	1.2340762153953000	0.10901720602002343	0.11090172060200000
14	1.7385377121165868	1.7385377121165999	2.4810520887463612E-002	2.4810520887460000E-002
15	2.2549740020892752	2.2549740020893001	3.2437733422378571E-003	3.2437733422379998E-003
16	2.7888060584281309	2.7888060584280998	2.2833863601635237E-004	2.2833863601630001E-004
17	3.3478545673832163	3.3478545673831999	7.8025564785320650E-006	7.8025564785320006E-006
18	3.9447640401156252	3.9447640401155999	1.0860693707692728E-007	1.0860693707690000E-007
19	4.6036824495507442	4.6036824495506998	4.3993409922731096E-010	4.3993409922730000E-010
20	5.3874808900112345	5.3874808900111999	2.2293936455341619E-013	2.2293936455340001E-013

Bibliography

[1] R. Budny. Fusion alpha parameters in tokamaks with high DT fusion rates. *Nucl. Fusion*, 42:1383, 2002.

[2] Andris M. Dimits, G. Bateman, M. Beer, B. I. Cohen, W. Dorland, G. W. Hammett, C. Kim, J. E. Kinsey, M. Kotschenreuther, A. H. Kritz, L. L. Lao, J. Mandrekas, W. M. Nevins, S. E. Parker, A. J. Redd, D. E. Shumaker, R. Sydora, and J. Weiland. Comparisons and physics basis of tokamak transport models and turbulence simulations. *Phys. Plasmas*, 7:969, 2000.

[3] D. J. Sigmar, R. Gormley, and G. Kamelander. Effects of anomalous alpha particle diffusion on fusion power coupling into tokamak plasma. *Nuclar Fusion*, 33(5):677, 1993.

[4] JET Team. Alpha particle studies during JET DT experiments. *Nuclear Fusion*, 39:1619, 1999.

[5] C. Z. Cheng, L. Chen, and M. S. Chance. High-n ideal and resistive shear Alfven waves in tokamaks. *Ann. Phys. (N. Y).*, 161:21, 1985.

[6] E. M. Bass and R. E. Waltz. Gyrokinetic simulations of mesoscale energetic particle-driven Alfvenic turbulent transport embedded in microturbulence. *Phys. Plasmas*, 17:112319, 2010.

[7] Mark Herrmann and Nathaniel Fisch. Cooling Energetic α Particles in a Tokamak with Waves. *Phys. Rev. Lett.*, 79:1495, August 1997.

[8] N. J. Fisch. Alpha channelling in mirrors and tokamaks. *Transactions of fusion science and technology*, 51:1, 2007.

[9] GY Fu and JW Van Dam. Excitation of the toroidicity-induced shear alfvén eigenmode by fusion alpha particles in an ignited tokamak. *Physics of Fluids B Plasma Physics*, 1(10):1949, 1989.

[10] H. Biglari, F. Zonca, and L. Chen. On resonant destabilization of toroidal Alfven eigenmodes by circulating and trapped energetic ions/alpha particles in tokamaks. *Phys. Fluids B Plasma Phys.*, 4:2385, 1992.

[11] SE Sharapov, B Alper, HL Berk, DN Borba, BN Breizman, CD Challis, IGJ Classen, EM Edlund, Jacob Eriksson, A Fasoli, et al. Energetic particle instabilities in fusion plasmas. *Nuclear Fusion*, 53(10):104022, 2013.

[12] H. Berk, B. Breizman, and H. Ye. Map model for nonlinear alpha particle interaction with toroidal Alfvén waves. *Phys. Fluids B*, 5:1506, 1993.

[13] B. N. Breizman and S. E. Sharapov. Energetic particle drive for toroidicity-induced Alfven eigenmodes and kinetic toroidicity-induced Alfven eigenmodes in a low-shear tokamak. *Plasma Phys. Control. Fusion*, 37:1057, 1995.

[14] R. E. Waltz and E. M. Bass. Prediction of the fusion alpha density profile in ITER from local marginal stability to Alfvén eigenmodes. *Nucl. Fusion*, 54:104006, 2014.

[15] C. Estrada-Mila, J. Candy, and R. E. Waltz. Turbulent transport of alpha particles in reactor plasmas. *Phys. Plasmas*, 13:112303, 2006.

[16] J. Candy and R. E. Waltz. An Eulerian gyrokinetic-Maxwell solver. *J. Comput. Phys.*, 186:545, April 2003.

[17] M. Albergante, J. P. Graves, a. Fasoli, F. Jenko, and T. Dannert. Anomalous transport of energetic particles in ITER relevant scenarios. *Phys. Plasmas*, 16:112301, 2009.

[18] F. Jenko, W. Dorland, M. Kotschenreuther, and B. N. Rogers. Electron temperature gradient driven turbulence. *Phys. Plasmas*, 7:1904, 2000.

[19] C. Angioni, A. G. Peeters, G. V. Pereverzev, A. Bottino, J. Candy, R. Dux, E. Fable, T. Hein, and R. E. Waltz. Gyrokinetic simulations of impurity , He ash and α particle transport and consequences on ITER transport. *Nucl. Fusion*, 49:055013, 2009.

[20] M. Kotschenreuther, G. Rewoldt, and W.M. Tang. Comparison of initial value and eigenvalue codes for kinetic toroidal plasma instabilities. *Comput. Phys. Commun.*, 88:128, August 1995.

[21] W. Dorland, F. Jenko, M. Kotschenreuther, and B. N. Rogers. Electron temperature gradient turbulence. *Phys. Rev. Lett.*, 85:5579, December 2000.

[22] T. Dannert, S. Gunter, T. Hauff, F. Jenko, X. Lapillonne, and P. Lauber. Turbulent transport of beam ions. *Phys. Plasmas*, 15:062508, 2008.

[23] M. N. Rosenbluth and P. H. Rutherford. Excitation of alfven waves by high-energy ions in a tokamak. *Phys. Rev. Lett.*, 34:1428, 1975.

[24] J. D. Gaffey. Energetic ion distribution resulting from neutral beam injection in tokamaks. *J. Plasma Phys.*, 16:149, 1976.

[25] C. Angioni and A. G. Peeters. Gyrokinetic calculations of diffusive and convective transport of α particles with a slowing-down distribution function. *Phys. Plasmas*, 15:052307, 2008.

[26] T. Hauff and F. Jenko. EB advection of trace ions in tokamak microturbulence. *Phys. Plasmas*, 14:092301, 2007.

[27] T. Hauff. *Transport of Energetic Particles in Turbulent Plasmas 2009*. PhD thesis, Universitat Ulm, 2009.

[28] M. J. Pueschel, F. Jenko, M. Schneller, T. Hauff, S. Gunter, and G. Tardini. Anomalous diffusion of energetic particles: connecting experiment and simulations. *Nucl. Fusion*, 52:103018, October 2012.

[29] T. Hauff, M. J. Pueschel, T. Dannert, and F. Jenko. Electrostatic and magnetic transport of energetic ions in turbulent plasmas. *Phys. Rev. Lett.*, 102:075004, February 2009.

[30] W. Zhang, V. Decyk, I. Holod, Y. Xiao, Z. Lin, and L. Chen. Scalings of energetic particle transport by ion temperature gradient microturbulence. *Phys. Plasmas*, 17:055902, 2010.

[31] G. Wilkie, I. Abel, E. Highcock, and Dorland W. Validating modeling assumptions of alpha particles in electrostatic turbulence. *Journal of Plasma Physics*, 81:905810306, 2015.

[32] P. Helander and D. Sigmar. *Collisional Transport in Magnetized Plasmas*. Cambridge University Press, 2002.

[33] R. Hazeltine and J. Meiss. *Plasma Confinement*. Dover, 2013.

[34] J. Huba. *NRL Plasma Formulary*. Naval Research Laboratory, Washington, 2011.

[35] I. Abel, G. G. Plunk, E Wang, M. Barnes, S. C. Cowley, W. Dorland, and A. Schekochihin. Multiscale Gyrokinetics for Rotating Tokamak Plasmas : Fluctuations , Transport and Energy Flows. *Reports Prog. Phys.*, 76:116201, November 2013.

[36] H Brysk. Fusion neutron energies and spectra. *Plasma Physics*, 15(7):611, 1973.

[37] B Appelbe and J Chittenden. The production spectrum in fusion plasmas. *Plasma Physics and Controlled Fusion*, 53(4):045002, 2011.

[38] T. H. Stix. Heating of toroidal plasma by neutral injection. *Plasma Phys.*, 14:367, 1973.

[39] T. Antonsen and B. Lane. Kinetic equations for low frequency instabilities in inhomogeneous plasmas. *Phys. Fluids*, 23:1205, 1980.

[40] E. A. Frieman and L. Chen. Nonlinear gyrokinetic equations for low-frequency electromagnetic waves in general plasma equilibria. *Phys. Fluids*, 25:502, 1982.

[41] R. E. Waltz, E. M. Bass, and G. M. Staebler. Quasilinear model for energetic particle diffusion in radial and velocity space. *Phys. Plasmas*, 20:042510, 2013.

[42] I. Abel and A. Schekochihin, 2015. In preparation.

[43] F. Parra. *Extension of gyrokinetics to transport time scales.* PhD thesis, Massachussetts Institute of Technology, 2009.

[44] P. J. Catto. Linearized gyro-kinetics. *Plasma Phys.*, 719:2, 1978.

[45] R. Kulsrud. In M. Rosenbluth and R. Sagdeev, editors, *Handbook of Plasma Physics*. North Holland Publishing, 1983.

[46] J. Freidberg. Ideal magnetohydrodynamic theory of magnetic fusion systems. *Rev. Mod. Phys.*, 54:801, 1982.

[47] M. Barnes. *Trinity: A unified treatment of turbulence, transport, and heating in magnetized plasmas.* PhD thesis, University of Maryland, 2009.

[48] J. A. Krommes and Genze Hu. The role of dissipation in the theory and simulations of homogeneous plasma turbulence, and resolution of the entropy paradox. *Phys. Plasmas*, 1:3211, 1994.

[49] I. Abel, M. Barnes, S. C. Cowley, W. Dorland, and A. Schekochihin. Linearized model FokkerPlanck collision operators for gyrokinetic simulations. I. Theory. *Phys. Plasmas*, 15:122509, 2008.

[50] M. Barnes, I. Abel, W. Dorland, D. R. Ernst, G. W. Hammett, Paolo Ricci, B. N. Rogers, A. Schekochihin, and T. Tatsuno. Linearized model Fokker-Planck collision operators for gyrokinetic simulations. II. Numerical implementation and tests. *Phys. Plasmas*, 16:072107, 2009.

[51] B. Li and D. R. Ernst. Gyrokinetic Fokker-Planck collision operator. *Phys. Rev. Lett.*, 106:195002, May 2011.

[52] J. Candy, R. E. Waltz, S. E. Parker, and Y. Chen. Relevance of the parallel nonlinearity in gyrokinetic simulations of tokamak plasmas. *Phys. Plasmas*, 13:074501, 2006.

[53] J. Candy, D. Borba, H. L. Berk, G. T. Huysmans, and W. Kerner. Nonlinear interaction of fast particles with Alfven waves in toroidal plasmas. *Phys. Plasmas*, 4:2597, 1997.

[54] J. Citrin, F. Jenko, P. Mantica, D. Told, C. Bourdelle, J. Garcia, J. W. Haverkort, G. M. D. Hogeweij, T. Johnson, and M. J. Pueschel. Nonlinear stabilization of tokamak microturbulence by fast ions. *Phys. Rev. Lett.*, 111:155001, October 2013.

[55] G. Tardini, J. Hobirk, V. G. Igochine, C. F. Maggi, P. Martin, D. C. McCune, A. G. Peeters, A. C. C. Sips, A. Stäbler, J. Stober, and ASDEX Upgrade Team. Thermal ions dilution and ITG suppression in ASDEX Upgrade ion ITBs. *Nucl. Fusion*, 47:280, April 2007.

[56] C. Holland, C. C. Petty, L. Schmitz, K. H. Burrell, G. R. McKee, T.L. Rhodes, and J. Candy. Progress in GYRO validation studies of DIII-D H-mode plasmas. *Nucl. Fusion*, 52:114007, November 2012.

[57] Y. Nishimura. Excitation of low-n toroidicity induced Alfven eigenmodes by energetic particles in global gyrokinetic tokamak plasmas. *Phys. Plasmas*, 16:030702, 2009.

[58] A. Mishchenko, A. Könies, and R. Hatzky. Gyrokinetic particle-in-cell simulations of Alfvén eigenmodes in presence of continuum effects. *Phys. Plasmas*, 21:052114, May 2014.

[59] C. Roach, M. Walters, R. Budny, F. Imbeaux, T. Fredian, M. Greenwald, J. Stillerman, D. Alexander, J. Carlsson, J. Cary, F. Ryter, J. Stober, P. Gohil, C. Greenfield, M. Murakami, G. Bracco, B. Esposito, M. Romanelli, V. Parail, P. Stubberfield, I. Voitsekhovitch, C. Brickley, A. R. Field, Y. Sakamoto, T. Fujita, T. Fukuda, Hayashi N., G. M. D. Hogeweij, A. Chudnovskiy, N. A. Kinerva, C. E. Kessel, T. Aniel, G. T. Hoang, J. Ongena, E. J. Doyle, W. A. Houlberg, A. R. Polvoi, ITPA Confinement Database, Modelling Topical Group, and ITPA Transport Physics Topical Group. The 2008 Public Release of the International Multi-tokamak Confinement Profile Database. *Nucl. Fusion*, 48:125001, 2008.

[60] D. J. Campbell. The physics of the International Thermonuclear Experimental Reactor FEAT. *Phys. Plasmas*, 8:2041, 2001.

[61] R. L. Miller, M. S. Chu, J. M. Greene, Y. R. Lin-Liu, and R. E. Waltz. Noncircular, finite aspect ratio, local equilibrium model. *Phys. Plasmas*, 5:973, 1998.

[62] V. Grandgirard, Y. Sarazin, P. Angelino, A. Bottino, N. Crouseilles, G. Darmet, G. Dif-Pradalier, X. Garbet, Ph. Ghendrih, and S. Jolliet. Global full-f gyrokinetic simulations of plasma turbulence. *Plasma Physics and Controlled Fusion*, 49:B173, 2007.

[63] Y. Idomura, M. Ida, T. Kano, N. Aiba, and S. Tokuda. Conservative global gyrokinetic toroidal full-f five-dimensional vlasov simulation. *Computer Physics Communications*, 179:391, 2008.

[64] M. A. Beer. *Gyrofluid models of turbulent transport in tokamaks*. PhD thesis, Princeton University, 1995.

[65] Y. Idomura. Full-f gyrokinetic simulation over a confinement time. *Physics of Plasmas*, 21:022517, 2014.

[66] M. Barnes, I. Abel, W. Dorland, T. Gorler, G. W. Hammett, and F. Jenko. Direct multiscale coupling of a transport code to gyrokinetic turbulence codes. *Phys. Plasmas*, 17:056109, 2010.

[67] J. Candy, C. Holland, R. E. Waltz, M. R. Fahey, and E. Belli. Tokamak profile prediction using direct gyrokinetic and neoclassical simulation. *Phys. Plasmas*, 16:060704, 2009.

[68] F. Parra and M. Barnes. Equivalence of two different approaches to global delta-f gyrokinetic simulations. *Plasma physics and controlled fusion*, 57:054003, 2015.

[69] N. Mandell and W. Dorland. Hybrid Gyrokinetic/Gyrofluid Simulation of ITG Turbulence. 2014.

[70] http://www.julialang.org.

[71] R. Balescu. Is Onsager symmetry relevant in the transport equations for magnetically-confined plasmas? *Phys. Bluids B*, 3:564, 1991.

[72] R. J. Groebner, W. Pfeiffer, F. P. Blau, K. H. Burrell, E. S. Fairbanks, Seraydarian R. P., H. St. John, and R. E. Stockdale. Experimentally inferred ion thermal diffusivity profiles in the Doublet III Tokamak: Comparison with neoclassical theory. *Nuclear Fusion*, 26:543, 1986.

[73] S. D. Scott, P. H. Diamond, R. J. Fonck, R. J. Goldston, R. B. Howell, K. P. Jaehnig, G. Schilling, E. J. Synakowski, M. C. Zarnstorff, C. E. Bush, Fredrickson E., Hill K. W., Janos A. C., D. K. Mansfield, D. K. Owens, H. Park, G. Pautasso, A. T. Ramsey, J. Schivell, Tait G. D., W. M. Tang, and G Taylor. Local measurements of correlated momentum and heat transport in the TFTR tokamak . *Phys. Rev. Lett.*, 64(5):531, 1990.

[74] EJ Synakowski, PC Efthimion, G Rewoldt, BC Stratton, WM Tang, B Grek, KW Hill, RA Hulse, DW Johnson, MW Kissick, et al. Helium, iron, and electron particle transport and energy transport studies on the tokamak fusion test reactor. *Physics of Fluids B: Plasma Physics (1989-1993)*, 5(7):2215–2228, 1993.

[75] E. J. Synakowski, R. E. Bell, R. V. Budny, C. E. Bush, P. C. Efthimion, B. ... Grek, and G. Taylor. Measurements of the Production and Transport of Helium Ash in the TFTR Tokamak. *Physical Review Letters*, 75(20):3689, 1995.

[76] P. C. Efthimion, S. Von Goeler, W. A. Houlberg, E. J. Synakowski, M. C. Zarnstorff, S. H. ... Batha, and G. Taylor. Observation of particle transport barriers in reverse shear plasmas on the Tokamak Fusion Test Reactor. *Physics of Plasmas*, 5(5):1832, 1998.

[77] MR Wade, TC Luce, and CC Petty. Gyroradius scaling of helium transport. *Physical review letters*, 79(3):419, 1997.

[78] JA Wesson. Sawtooth oscillations. *Plasma physics and controlled fusion*, 28(1A):243, 1986.

[79] AW Edwards, DJ Campbell, WW Engelhardt, H-U Fahrbach, RD Gill, RS Granetz, S Tsuji, BJD Tubbing, A Weller, J Wesson, et al. Rapid collapse of a plasma sawtooth oscillation in the jet tokamak. *Physical review letters*, 57(2):210, 1986.

[80] Ya I Kolesnichenko and Yu V Yakovenko. Sawtooth oscillations and fast-ion ejection in tokamaks. *Nuclear fusion*, 32(3):449, 1992.

[81] M. F. F. Nave, J. Rapp, T. Bolzonella, R. Dux, M. J. Mantsinen, R. Budny, P. Dumortier, M. von Hellermann, S. Jachmich, H. R. Koslowski, G. Maddison, A. Messiaen, P. Monier-Garbet, J. Ongena, M. E. Puiatti, J. Strachan, G. Telesca, B. Unterberg, M Valisa, P. de Vries, and Contributors to the JET-EFDA Workprogramme. Role of sawtooth in avoiding impurity accumulation and maintaining good confinement in JET radiative mantle discharges. *Nucl. Fusion*, 43:1204, October 2003.

[82] Stefan Kragh Nielsen, Mirko Salewski, Henrik Bindslev, A Bürger, Vedran Furtula, M Kantor, Søren Bang Korsholm, HR Koslowski, A Krämer-Flecken, Frank Leipold, et al. Dynamics of fast ions during sawtooth oscillations in the textor tokamak measured by collective thomson scattering. *Nuclear fusion*, 51(6):063014, 2011.

[83] C. Z. Cheng, N. N. Gorelenkov, and C. T. Hsu. Fast particle destabilization of toroidal alfven eigenmodes. *Nuclear fusion*, 35(12):1639, 1995.

[84] P Rodrigues, A Figueiredo, J Ferreira, R Coelho, F Nabais, D Borba, NF Loureiro, HJC Oliver, and SE Sharapov. Systematic linear-stability assessment of alfvén eigenmodes in the presence of fusion α-particles for iter-like equilibria. *Nuclear Fusion*, 55(8):083003, 2015.

[85] E Highcock. *The Zero-Turbulence Manifold in Fusion Plasmas*. PhD thesis, Oxford University, 2012.

[86] A. B. Langdon and Charles K Birdsall. Theory of plasma simulation using finite-size particles. *Phys. Fluids*, 13:2115, 1970.

[87] M. D. Meyers, C.-K. Huang, Y. Zeng, S. A. Yi, and B. J. Albright. On the numerical dispersion of electromagnetic particle-in-cell code: Finite grid instability. Technical report, 2014.

[88] C.-K. Huang, Y. Zeng, Y. Wang, M. D. Meyers, S. A. Yi, and B. J. Albright. Finite grid instability and spectral fidelity of the electrostatic particle-in-cell algorithm. Technical report, 2015.

[89] A. Y. Aydemir. A unified Monte Carlo interpretation of particle simulations and applications to non-neutral plasmas. *Phys. Plasmas*, 1:822, 1994.

[90] S. E. Parker and W. W. Lee. A fully nonlinear characteristic method for gyrokinetic simulation. *Phys. Fluids B Plasma Phys.*, 5:77, 1993.

[91] Richard E. Denton and M. Kotschenreuther. df algorithm. *J. Comput. Phys.*, 119:283, 1995.

[92] I. Broemstrup. *Advanced Lagrangian Simulation Algorithms for Magnetized Plasmas Turbulence*. PhD thesis, University of Maryland, 2008.

[93] Igor Manuilskiy and W. W. Lee. The split-weight particle simulation scheme for plasmas. *Phys. Plasmas*, 7:1381, 2000.

[94] C. W. Nielson and H. R. Lewis. *Methods of Computational Physics*, volume 16. Academic Press, 1976.

[95] W. W. Lee. Gyrokinetic approach in particle simulation. *Phys. Fluids*, 26:556, 1983.

[96] W. Dorland. *Gyrofluid Models of Plasma Turbulence*. PhD thesis, Princeton University, 1993.

[97] R. Courant, K. Friedrichs, and H. Lewy. On the partial difference equations of mathematical physics. *IBM J. Res. ...*, 1967.

[98] W. M. Nevins, G. W. Hammett, Andris M. Dimits, W. Dorland, and D. E. Shumaker. Discrete particle noise in particle-in-cell simulations of plasma microturbulence. *Phys. Plasmas*, 12:122305, 2005.

[99] Y. Chen and S. E. Parker. A δf particle method for gyrokinetic simulations with kinetic electrons and electromagnetic perturbations. *J. Comput. Phys.*, 189:463, August 2003.

[100] Y. Chen and S. E. Parker. Coarse-graining phase space in δf particle-in-cell simulations. *Phys. Plasmas*, 14:082301, 2007.

[101] M. Landreman and D. Ernst. New velocity-space descretization for continuum kinetic calculations and Fokker-Planck collisions. *J. Comput. Phys.*, 243:130, 2013.

[102] W. Press, S. Teukolsky, W. Vetterling, and B. Flannery. *Numerical Recipes, third edition*. Cambridge University Press, 2007.

[103] http://www.netlib.org/quadpack.

[104] W. Gautschi. In P. Nevai, editor, *Orthogonal polynomials and functional analysis*. Kluwer Academic Publishers, 1990.